q-SPACE, RESTRICTED DIFFUSION AND PULSED GRADIENT SPIN ECHO NUCLEAR MAGNETIC RESONANCE

A thesis presented in partial fulfilment of the requirements
for the degree of Doctor of Philosophy in Physics
at Massey University

Andrew Coy

1995

p. ii, line 5	'pervides' should read 'provides'
p. ii, line 7	'give' should read 'given'
p. 25, bottom of page	't' should read 'τ'
p. 28, eqn (3.28)	full stop is in the wrong place
p. 29, lines 5 and 9, section 3.3.2	$\underline{\mathbf{r'}}$ should read $\mathbf{r}'$
p. 36, eqn (4.6)	$\overline{P_s}(Z,\infty)$ should read $Z^2\overline{P_s}(Z,\infty)$
p. 40, line 4	'logrwe' should read 'logarithmic'
p. 40, line 7	'ration' should read 'ratio'
p. 42, line 10, section 4.2.3	'planer' should read 'planar'
p. 42, line 3, section 4.3	'criteria' should read 'criterion'
p. 48, line 8	'on the order of' should read 'of the order of'
p. 78, line 13, section 6.6	'move' should read 'more'
p. 81, line 9, section 7.1	'hoping' should read 'hopping'
p. 93, bottom line	'However' should read 'however'
p. 94, line 10, section 7.4.3	'm^1' should read 'm^{-1}'
p. 118, line 17, section 8.3.3	'losses' should read 'loses'
p. 126, line 23	'repatative' should read 'reptative'

Abstract

The theory and technique of Pulsed Gradient Spin Echo (PGSE) Nuclear Magnetic Resonance (NMR) are presented. Particular attention is paid to the Fourier relationship between the average propagator of motion and the echo attenuation function. Using the q-space formalism, existing PGSE theory for diffusing molecules trapped between parallel barriers is extended to include the effects of relaxation at the walls. Computer simulations have been performed to test this extension to the theory and also to investigate the effect of finite gradient pulses in such an experiment.

PGSE experiments were performed on pentane inside rectangular microslides of $100~\mu$m width. Diffraction-like effects predicted by theory for such experiments were observed where the PGSE data has a minimum when the gradient wavevector $\mathbf{q}$ is equal to the reciprocal width of the microslides. Through the use of non-linear least squares fitting techniques the PGSE data is fitted to theories for perfectly reflecting walls, partially reflecting walls and wall with variable spacings.

NMR microimaging experiments were performed on the microslide capillaries. The images revealed edge enhancement effects which can be explained through the signal attenuation expressions used in PGSE experiments. A brief theoretical discussion shows that the effect is due to the restricted diffusion of the molecules at the boundaries compared with the center of the sample.

A pore hopping technique is presented which allows analytic expressions to be found for diffusion in porous media. PGSE experiments are performed on water diffusing in the interconnecting voids formed by close packed, monodisperse, micron sized polystyrene spheres. Diffraction-like interference effects predicted by theory are obseeved where the PGSE data has a maximum when q is equal to the reciprocal lattice spacing of the porous network. Using non-linear least squares fitting techniques the PGSE data is fitted to the pore hopping theory for a pore glass with some variation in pore spacing. The use of an appropriate structure function for the pore shape is analysed by modelling the true pore shape and comparing it to the structure function for a sphere. The parameters revealed by fitting theory to data are consistent with the known dimensions and show that important structural information can be revealed by this technique.

Electron Spin Resonance (ESR) experiments are performed on the quasi-one-dimensional organic conductor $(FA)_2PF_6$. PGSE experiments on the conduction electrons show restricted diffusion effects. The PGSE data is analysed using both an impermeable relaxing wall model and a permeable pore hopping model. Fitting the data to these models show that a hopping model is more consistent with the data.

PGSE experiments are performed on semi-dilute solutions of high molecular weight polystyrene dissolved in CCl_4. The reptation model of diffusion is reviewed and features of this model relevant to PGSE experiments are detailed. PGSE exper-

iments are performed and the mean square displacement of the entangled polymers is obtained as a function of diffusion time. Transitions from t to $t^{1/2}$ scaling of the mean square displacement are found, and a region exhibiting $t^{1/4}$ scaling is also observed, this region often being considered the signature for reptation.

The PGSE-MASSEY technique, which pervides a method to correct for gradient pulse mismatch, is described. The details of the hardware and software implementation of this technique are also give. PGSE-MASSEY experiments are performed on the semi-dilute polymer solutions and enable structure functions to be acquired. These structure functions are compared to the primitive chain structure function enabling an estimate of the Doi-Edwards tube diameter to be made.

Acknowledgements

Contents

List of Figures

List of Tables

LIST OF TABLES

Chapter 1

INTRODUCTION

1.1 Introduction

The Pulsed Gradient Spin Echo (PGSE) experiment has been used to measure molecular self-diffusion since the 1950's, long before the advent of NMR imaging techniques in 1973. In recent years, however, there has been a resurgence of interest in the PGSE experiment, the main reason for which was the suggestion that one could measure 'structure' inside a sample by observing the effect the 'structures' have on the self-diffusion of an interpenetrating liquid.

Traditionally the PGSE experiment was used almost exclusively to measure the self-diffusion coefficient of some liquid (or gaseous) sample. It was realised recently though that this type of experiment actually contains far more information than just the self-diffusion coefficient. In fact PGSE closely resembles a dynamic incoherent scattering experiment when the gradient pulses are sufficiently narrow. Such a scattering experiment contains information about the self-propagator that describes a molecule's displacement as a function of time. In free diffusion, the propagator would be a simple Gaussian function of time and distance. For a sample containing restrictions (walls, pores or otherwise) to a molecule's motion, the propagator will be altered as a result of interactions between the molecules and the restrictions.

In this thesis a q-space, or scattering, approach is used to analyse PGSE experiments. In this approach, the PGSE data acquired from diffusing molecules trapped between parallel barriers is identical in form to the single slit diffraction pattern. A minimum is observed in the echo attenuation data when q is equal to the reciprocal of the barrier spacing. This reciprocal space formalism is made apparent through a Fourier relationship between the echo attenuation function and the average propagator mentioned above.

The intention throughout this thesis has been to extend the ideas of a q-space approach to PGSE and to apply these ideas to real experiments performed on model systems. At the initiation of this thesis no PGSE experiment had been performed where the diffraction-like effects described above had been seen. In particular, no PGSE data had ever shown an increase in the echo signal with an *increase* in gradient strength. In analysing the data from experiments we have also fitted theory to data in an attempt to reveal quantitative parameters of interest to the system, demonstrating that such an approach may prove useful in samples where the structure dimensions were unknown.

As well as completely restricted diffusion, where the molecules are confined to an enclosed region, porous systems have also been a strong focus of PGSE work. A

q-space approach to model porous systems showed that the echo attenuation data would be similar to the pattern formed from multiple slit interference where a local maximum is observed at the reciprocal lattice distance. Again we have taken the approach of fitting the analytic theory derived to the PGSE data to reveal several important structural parameters pertaining to the model system under investigation.

Restricted diffusion ideas apply in a completely different way to the motion of entangled polymers in solution. The theory of de Gennes and Doi and Edwards predicts a reptative mechanism for diffusion similar to the motion observed in a "can of worms". As part of our effort to probe smaller distances with stronger gradients, we have implemented the PGSE-MASSEY technique. This technique enables any mismatch in the gradient pulses applied to be corrected. As this is the fundamental barrier to increased resolution in the PGSE experiment, and not signal-to-noise as is the case for NMR microimaging, any advances in this area are extremely useful.

The use of computers and software in this thesis has been extensive. A significant problem concerns non-linear least squares fitting necessary in order to fit theory to data in PGSE experiments. Computers have also been used to perform Monte Carlo simulations of molecules in PGSE experiments to test the extensions to PGSE theory shown here. The effects of finite gradient pulses were also of key interest as they are difficult to analyse theoretically and the effect on the echo attenuation function in restricted diffusion work was unknown.

The majority of this thesis deals with experiments on several different model systems. The similarity is that all restrict the motion of the molecules and in the process alter the dynamic propagator in such a way that the structural features that restricted the molecular motion can be measured. As the characterisation of this technique on model systems is completed the possibility for use in real samples of interest increases. An exciting possibility is that the gradient strengths becoming available to PGSE NMR, combined with a q-space approach, will allow samples with features as small as 100 Å to be studied.

1.2 Organisation of thesis

The theory for the work in this thesis is discussed initially.

- Chapter 2 introduces the NMR phenomenon and discusses the basic theory needed to understand the concepts of free induction decay, spin and stimulated echoes, relaxation and signal-to-noise ratios.

- Chapter 3 introduces the concept of magnetic field gradients and reviews the theory associated with imaging and diffusion measurements. The concept of q is introduced to describe a scattering wave vector in the PGSE experiment. An overview of the hardware used to perform the experiments in this thesis is also detailed.

- Chapter 4 details the q-space theories for several different sample geometries. The effect of finite gradient pulses is also investigated using computer simulations.

- Chapter 5 reviews the PGSE-MASSEY variation used to measure very small displacements with large field gradients. This technique was used in the work on polymer diffusion.

The experimental work carried out is then presented.

- Chapter 6 presents the work carried out on the fully enclosing rectangular microslide system. The review of the extension to the theory presented in Chapter 4 to include the effects of relaxation at the walls is presented. Both PSGE experiments, and an imaging experiment, were performed on the microslide sample. Several computer simulations were also performed. Fitting of theory to the PGSE data enables structural parameters to be deduced. The microimaging experiments revealed an edge enhancement effect explained by restricted diffusion at the sample boundaries.

- Chapter 7 reviews the theory for diffusion in a porous system. Experiments were carried out on a porous sample of close packed monodisperse polystyrene spheres. The fitting of theory to data again revealed important structural details. ESR experiments were performed on a one-dimensional conducting crystal in which the PGSE data showed restricted diffusion effects.

- Chapter 8 reviews the theory for polymer reptation. The experiments performed on semi-dilute, high molecular weight, monodisperse polymer solutions are presented. The enclosing network in an entangled polystyrene system presents a quite different type of restriction to the molecular diffusion. The PGSE-MASSEY technique is also used as part of these experiments.

Chapter 9 concludes the thesis and discusses potential future work in this area.

Chapter 2

NMR Theory

2.1 Quantum mechanical description

The field of nuclear magnetic resonance (NMR) reveals an interesting relationship between classical and quantum mechanics. While the nature of the NMR phenomenon is entirely quantum mechanical, it lends itself to a classical description with such ease that one can proceed far into the discipline without reference to the former. However there are occasions where the full quantum mechanical treatment is needed to explain effects observed in an NMR experiment[1, 2, 3]. Bearing these points in mind a brief quantum description of the nature of nuclear magnetization will be given before proceeding with the more widely used classical macroscopic magnetization description which will be used liberally throughout this dissertation.

2.1.1 Nuclear magnetic moment

The magnetic properties of atomic nuclei are related, like electrons, to their angular momentum[4]. A nucleus will possess a total magnetic moment $\boldsymbol{\mu}$ and a total angular momentum $\mathbf{L}$. In fact these two vectors are parallel such that

$$\boldsymbol{\mu} = \gamma \mathbf{L} \tag{2.1}$$

where γ is called the gyromagnetic ratio and is specific to the nucleus in question. Whilst in the case of atomic electrons it is the orbital angular momentum of the electronic charge that is the foundation for any magnetic properties, in the case of the nucleus it is the intrinsic angular momentum or spin of the nuclei that generates nuclear magnetism. Although it is convenient to imagine a rotating lump of charge generating a magnetic moment in a classical way, this belies the true quantum nature of the angular momentum of a nucleus.

In quantum mechanics $\boldsymbol{\mu}$ and $\mathbf{L}$ are treated as operators. A dimensionless angular momentum operator $\mathbf{I}$ is often defined so that

$$\mathbf{L} = \hbar \mathbf{I} \tag{2.2}$$

where $\hbar$ is Plancks constant divided by 2π. The magnitude of the angular momentum can be found by applying the operator $\mathbf{I}^2$ to a wave function and the resulting eigenvalue is found to have the value $I(I + 1)$, where I is a positive integer or half-integer for the case of intrinsic angular momentum. For the case of orbital angular momentum, such as an electron rotating around the nucleus, I can only

be an integer due to the boundary condition that the particle wave function must be a well- behaved function of particle position. The number I is known as the spin quantum number or spin of a nucleus in the case of NMR. For example, a ^{1}H hydrogen (proton) or ^{13}C nucleus has $I = 1/2$, whereas a ^{2}H deuterium nucleus has $I = 1$.

Operators to find each cartesian component of angular momentum can be defined as I_x, I_y and I_z respectively, but these operators do not commute with each other. However each component operator does commute with $\mathbf{I}^2$ allowing one to measure both the magnitude of the angular momentum and the component in one direction simultaneously. The eigenvalue of the component (normally taken as I_z) has $2I + 1$ possible values, being $m = I, I - 1 \ldots, -I$. For the example of a hydrogen nucleus where $I = 1/2$ the z component of angular momentum can have the values $m = 1/2$ or $m = -1/2$. One can therefore use these well known angular momentum operators in eqn (2.1) and eqn (2.2) to determine the magnetic moment through relationships such as

$$\mu_z = \gamma \hbar I_z. \tag{2.3}$$

The quantum state of a nucleus, $|\Psi\rangle$, can be described as a combination of basis states $|Im\rangle$. Because we often deal with similar nuclei for which I would be identical it is normal to label the basis states only by m. In other words

$$|\Psi\rangle = \sum_m a_m |m\rangle \tag{2.4}$$

where a_m represents the complex amplitude of each basis state $|m\rangle$ present in $|\Psi\rangle$.

2.1.2 The Zeeman interaction

If the nucleus is placed in a magnetic field then the magnetic moment will interact with the field. The basis states $|Im\rangle$ will no longer be degenerate and each will have a different energy level. This splitting is known as a Zeeman interaction. A magnetic dipole μ in a magnetic field B has an interaction energy of $-\boldsymbol{\mu} \cdot \mathbf{B}$. From eqn (2.3) the Hamiltonian for the case of a field $\mathbf{B}_0 = \mathbf{k}B_0$ oriented along the z-axis is

$$\mathcal{H} = -\gamma \hbar B_0 I_z. \tag{2.5}$$

The eigenvalues of this Zeeman Hamiltonian are simply

$$E_m = -\gamma \hbar B_0 m \tag{2.6}$$

where $m = I, I - 1, \ldots, -I$. A schematic representation of these energy levels are shown in Figure 2.1.

Nuclear precession

Time evolution of the nuclear wavefunction $\Psi(t)$ in the magnetic field is described by the Schrödinger equation using the Hamiltonian from eqn (2.5)

$$i\hbar \frac{\partial}{\partial t} |\Psi(t)\rangle = \mathcal{H} |\Psi(0)\rangle \tag{2.7}$$

Figure 2.1: Schematic representation of the energy levels for an $I = 1/2$ spin in a magnetic field B_0. The energy levels can be calculated from eqn (2.6) and the populations from eqn (2.20)

which can be written in terms of an evolution operator $U(t)$ as

$$|\Psi(t)\rangle = U(t)|\Psi(0)\rangle \tag{2.8}$$

where

$$U(t) = \exp(\frac{-i\mathcal{H}t}{\hbar}). \tag{2.9}$$

Using the Hamiltonian of eqn (2.5), one can express this as

$$U(t) = \exp(i\gamma B_0 I_z t). \tag{2.10}$$

This "exponential operator" formalism is well known in quantum mechanics and is utilised through the rule

$$R_z(\phi) = \exp(i\phi I_z) \tag{2.11}$$

where $R_z(\phi)$ is a rotation of ϕ degrees about the z-axis. Eqn (2.10) therefore suggests that in a magnetic field all states precess at a frequency ω_0 around the z axis, given by

$$\omega_0 = \gamma B_0. \tag{2.12}$$

This precession frequency is known as the Larmor frequency and is the fundamental equation used in NMR. It is interesting to note that the rotation operators about different axes do not commute with each other, just as I_x, I_y and I_z do not.

To detect this "precession" of the wavefunction the nuclei have to be disturbed. In the simple picture described at this stage, this would involve the absorption of some energy equivalent to the transition between two levels. The most common way this energy is applied is through a transverse alternating magnetic field of frequency $\omega = \Delta E/\hbar$. If the perturbing field B_1 is oscillating in the x direction then one would have a Hamiltonian of the form

$$\mathcal{H}_{\text{pert}} = \gamma\hbar B_1 \cos\omega t I_x. \tag{2.13}$$

The operator I_x has only finite matrix elements between states m and m' when $m' = m \pm 1$. Consequently transitions are allowable only between adjacent energy levels and would require the absorption or emission of energy

$$\Delta E = \hbar\omega = \gamma\hbar B_0 \tag{2.14}$$

or in terms of the frequency of the applied transverse field

$$\omega = \omega_0 = \gamma B_0. \tag{2.15}$$

Eqn (2.15) says that by applying an alternating field in the x (or y) axis, whose frequency is equal to the Larmor frequency, one can induce a transition between two adjacent energy levels. To discover the effect of this transition, a measurement would have to be made on the system.

2.1.3   The ensemble average

The result of a measurement on a nucleus in an admixture state described by
eqn (2.4) would be given by

$$\langle I_z \rangle = \langle \Psi | I_z | \Psi \rangle = \sum_m |a_m|^2 \, m. \tag{2.16}$$

This result is called the 'expectation value' of a measurement of I_z. For a single
nucleus this gives the probability $|a_m|^2$ of returning a value m. For a large number of
nuclei in the same state $|\Psi\rangle$ this expectation value is the mean of eigenvalue results
weighted by the probability of each occurring.

In a real sample, one would no longer be dealing with one nucleus but with many
identical nuclei, but where each can occupy a different state $|\Psi\rangle$. To calculate the
expectation value of I_z, one has to modify eqn (2.16) to allow for the case where
spins can be in different states $|\Psi\rangle$. The "average" ensemble expectation value for
I_z would now be

$$\overline{\langle \Psi | I_z | \Psi \rangle} = \sum_\Psi p_\Psi \langle \Psi | I_z | \Psi \rangle \tag{2.17}$$

where p_Ψ is the proportion of spins in a state $|\Psi\rangle$. For the simple case of $I = 1/2$ at
thermal equilibrium, some spins will be in the higher energy state $m = +1/2$ while
the rest will be in the lower energy state $m = -1/2$. The expectation of the angular
momentum will be

$$\overline{\langle I_z \rangle} = \overline{\langle \Psi | I_z | \Psi \rangle} = \frac{1}{2} \left(\overline{|a_{\frac{1}{2}}|^2} - \overline{|a_{-\frac{1}{2}}|^2} \right). \tag{2.18}$$

This tells us simply that the expectation value of the z component of angular mo-
mentum is the population difference between the two levels. The populations at
thermal equilibrium will be given by the Boltzmann factor, and the two levels will
have the populations

$$\overline{|a_{\pm\frac{1}{2}}|^2} = \frac{\exp\left(\pm\gamma\hbar B_0/2k_B T\right)}{\exp\left(\gamma\hbar B_0/2k_B T\right) + \exp\left(-\gamma\hbar B_0/2k_B T\right)}. \tag{2.19}$$

At room temperature the factor $k_B T$ will be many orders of magnitude larger than
the energy difference $\gamma\hbar B_0$ and hence the populations can be rewritten as

$$\overline{|a_{\pm\frac{1}{2}}|^2} = \frac{1}{2} \left(1 \pm \frac{\gamma\hbar B_0}{2k_B T} \right). \tag{2.20}$$

The population difference will then be

$$\overline{|a_{\frac{1}{2}}|^2} - \overline{|a_{-\frac{1}{2}}|^2} = \frac{\gamma\hbar B_0}{2k_B T}. \tag{2.21}$$

For protons at room temperature this factor is around 5×10^{-6} for a field of 1.4 T
(60 MHz). This population difference is what allows the NMR phenomenon to be
detected. Using eqn (2.18) one gets

$$\overline{\langle I_z \rangle} = \frac{\gamma\hbar}{4k_B T} B_0. \tag{2.22}$$

In fact, the state for an ensemble of spin $I = 1/2$ nuclei is completely defined by the quantities $\overline{\langle I_x \rangle}$, $\overline{\langle I_y \rangle}$ and $\overline{\langle I_z \rangle}$. A macroscopic classical magnetization vector $\mathbf{M}$ can be defined such that

$$\mathbf{M} = N\gamma\hbar \left[\overline{\langle I_x \rangle}\mathbf{i} + \overline{\langle I_y \rangle}\mathbf{j} + \overline{\langle I_z \rangle}\mathbf{k} \right] \tag{2.23}$$

where N is the number of spins per unit volume. When the spins are at thermal equilibrium in a magnetic field this magnetization vector will be aligned along the z-axis with magnitude

$$\overline{\langle M_z \rangle} = \frac{N\gamma^2\hbar^2}{4k_{\mathrm{B}}T}B_0 \tag{2.24}$$

which can be recognised as Curie's law for magnetization. This can be generalised for all values of I by recalculating eqn (2.18) and leads to

$$\overline{\langle M_z \rangle} = \frac{N\gamma^2\hbar^2 I(I+1)}{3k_{\mathrm{B}}T}B_0. \tag{2.25}$$

The magnetization vector $\mathbf{M}$ is a most useful description of the NMR phenomenon as it allows a classical picture of what is happening to be used. However the "vector" approach breaks down for cases when $I > 1/2$ where a tensor of higher rank would be needed to provide a full description of the spin system.

2.2 The semi-classical description

2.2.1 The rotating frame

It is now possible to use our macroscopic magnetization vector $\mathbf{M}$ to describe the effect of disturbing the spins using an alternating magnetic field as described by eqn (2.13). Classically a magnetic field $\mathbf{B}$ exerts a torque $\mathbf{M} \times \mathbf{B}$ on the magnetization vector $\mathbf{M}$. The equation of motion for $\mathbf{M}$ can easily be written down. From rotational mechanics, the torque is equal to the rate of change of angular momentum, so

$$\frac{\partial \mathbf{L}}{\partial t} = \mathbf{M} \times \mathbf{B} \tag{2.26}$$

and from eqn (2.1)

$$\frac{\partial \mathbf{M}}{\partial t} = \mathbf{M} \times (\gamma \mathbf{B}). \tag{2.27}$$

This equation holds regardless of the time dependence of $\mathbf{B}$. The motion of the magnetization vector $\mathbf{M}$ is solved by finding solutions to this equation. For constant $\mathbf{B}$ the equation is identical to the precession equation of a spinning top implying as stated before that the nuclear magnetization rotates around the magnetic field. In fact eqn (2.27) can also be derived quantum mechanically for $\boldsymbol{\mu}$ giving the same result[2].

A useful trick is to use a rotating coordinate system. If a coordinate system is defined that rotates with fixed angular velocity $\boldsymbol{\Omega}$ then eqn (2.27) transforms to

$$\frac{\delta \mathbf{M}}{\delta t} = \mathbf{M} \times (\gamma \mathbf{B} + \boldsymbol{\Omega}) \tag{2.28}$$
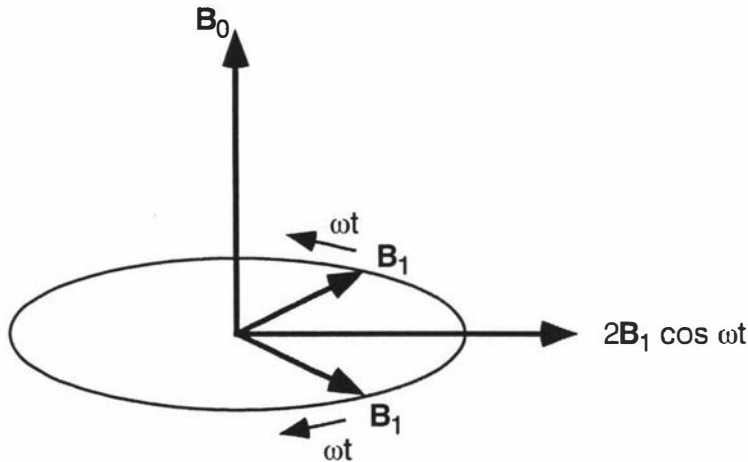
Figure 2.2: An alternating field $2\mathbf{B}_1 \cos \omega t$ represented by two counter rotating field components with magnitude B_1.

where $\delta \mathbf{M}/\delta t$ is the rate of change of $\mathbf{M}$ with respect to the new rotating coordinate system. The equation of motion for $\mathbf{M}$ is the same as in the laboratory (non-rotating) frame, if $\mathbf{B}$ is replaced by an effective field $\mathbf{B}_{\text{eff}}$, such that

$$\mathbf{B}_{\text{eff}} = \mathbf{B} + \frac{\Omega}{\gamma}. \tag{2.29}$$

This implies that for a fixed field $\mathbf{B} = B_0 \, \mathbf{k}$ and a rotating coordinate system $\Omega = -\gamma B_0 \, \mathbf{k}$ that the magnetization vector $\mathbf{M}$ will appear to remain fixed in time. In other words, rotating our reference frame at the Larmor frequency makes it appear that B_0 has disappeared and $\delta \mathbf{M}/\delta t = 0$. Of course the bulk magnetization of the spins remains fixed.

2.2.2   Resonant excitation

The effect of an alternating field $\mathbf{B}_1$ along the x direction with magnitude $2B_1$ is now considered. A coil around the sample has an r.f. current applied to it and therefore generates an oscillating r.f. field on the sample. This field can be represented by the sum of two counter rotating components each of magnitude B_1 as shown in Figure 2.2. In the rotating frame, only the component rotating in the same direction need be considered; the other component would fluctuate at $2\omega_0$ and would have little effect on the spins. In the lab frame one can write

$$\mathbf{B}_1(t) = B_1(\cos \omega t \, \mathbf{i} - \sin \omega t \, \mathbf{j}) \tag{2.30}$$

so eqn (2.27) becomes

$$\frac{\partial \mathbf{M}}{\partial t} = \mathbf{M} \times \gamma(\mathbf{B}_0 + \mathbf{B}_1(t)) \tag{2.31}$$

which would give

$$\begin{aligned}
\frac{dM_x}{dt} &= \gamma(M_z B_1 \sin \omega_0 t + M_y B_0) \\
\frac{dM_y}{dt} &= \gamma(M_z B_1 \cos \omega_0 t - M_x B_0) \\
\frac{dM_z}{dt} &= \gamma(-M_x B_1 \sin \omega_0 t - M_y B_1 \cos \omega_0 t).
\end{aligned} \tag{2.32}$$
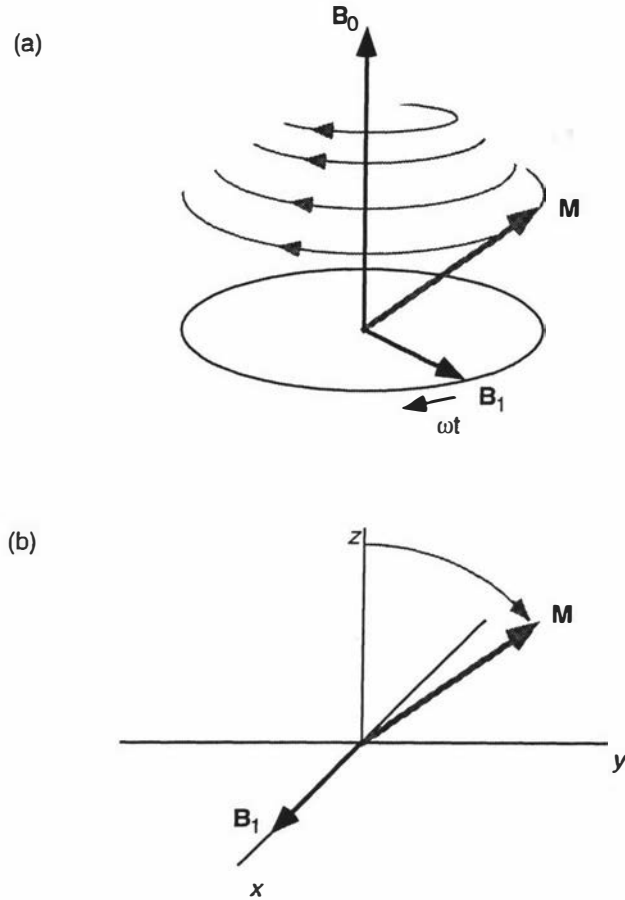
Figure 2.3: (a) The laboratory frame evolution of the magnetization vector $\mathbf{M}$ about $\mathbf{B}_0$ and $\mathbf{B}_1$. (b) The rotating frame evolution of $\mathbf{M}$ about $\mathbf{B}_1$.

Under the initial condition that the magnetization is aligned along the z-axis one gets solutions

$$
\begin{aligned}
M_x &= M_0 \sin \omega_1 t \sin \omega_0 t \\
M_y &= M_0 \sin \omega_1 t \cos \omega_0 t \\
M_z &= M_0 \cos \omega_0 t
\end{aligned}
\tag{2.33}
$$

which implies that the magnetization simultaneously precesses about $\mathbf{B}_0$ at a rate ω_0 and about $\mathbf{B}_1$ at a rate ω_1 as shown in Figure 2.3a. By switching to a frame of reference rotating with B_1 about B_0, eqn (2.28) becomes

$$
\frac{\delta \mathbf{M}}{\delta t} = \mathbf{M} \times \gamma B_1 \mathbf{i}.
\tag{2.34}
$$

The solution of which under the same initial conditions as before gives

$$
\begin{aligned}
M_x &= 0 \\
M_y &= M_0 \sin \omega_1 t \\
M_z &= M_0 \cos \omega_1 t
\end{aligned}
\tag{2.35}
$$

a rotation about B_1. In rotating frame coordinates, the vector $\mathbf{M}$ will precess about the x axis at a rate $\omega_1 = \gamma B_1$. If B_1 is applied as a pulse of duration t, it will

cause the magnetization to rotate an angle $\phi = \gamma B_1 t$ about the x axis as shown in Figure 2.3b. In the laboratory frame it is also simultaneously rotating around the z axis at the Larmor frequency.

Quantum mechanical excitation

It is interesting to briefly consider the effect of the B_1 field quantum mechanically. If one is applying alternating magnetic fields to the sample one has to consider the effect of a time dependant Hamiltonian on our spins. The Hamiltonian contains a static term from eqn (2.5) and a time dependant term from eqn (2.13) and can be written

$$\mathcal{H}_{\text{lab}} = -\gamma \hbar B_0 I_z - \gamma \hbar B_1 \cos \omega t I_x. \tag{2.36}$$

Using the idea discussed above one can transform to the rotating frame where

$$\mathcal{H}_{\text{rot}} = -\gamma \hbar (B_0 - \Omega/\gamma) I_z - \gamma \hbar B_1 I_x, \tag{2.37}$$

and at the resonant frequency where $\Omega = \gamma B_0$ one gets

$$\mathcal{H}_{\text{rot}} = -\gamma \hbar B_1 I_x. \tag{2.38}$$

From eqn (2.9)the evolution operator for the wavefunction can be written as

$$U(t) = \exp(\mathrm{i}\gamma B_1 I_x t) \tag{2.39}$$

which is from eqn (2.11) a rotation about the x axis at a rate $\omega_1 = \gamma B_1$ identical to the classical prediction. In fact eqn (2.38) has a subtle difference to the classical picture. It can be shown that a rotation of 2π about $\mathbf{B}_1$ does not return the wavefunction Ψ to its original value. A rotation of 4π is needed to return Ψ to its initial value, this general property is known as the "spinor" property[2] of Ψ. However, ingenious NMR experiments are needed to demonstrate this property which is mentioned here purely for interest.

2.2.3   Relaxation

We return now to the classical picture of our magnetization vector $\mathbf{M}$ rotating around the z axes at a rate ω_0. If we apply an r.f. field B_1 then $\mathbf{M}$ also rotates about that field at a rate ω_1 such that it gets "tipped" away from its equilibrium position. An r.f. pulse of duration t such that $\omega_1 t = \pi/2$ is called a 90° pulse. In our picture so far $\mathbf{M}$ would continue to precess around the z axis after the r.f. field was turned off endlessly. In reality there are mechanisms that return $\mathbf{M}$ to its equilibrium position along the z axis.

The equilibrium is restored by a process known as spin-lattice or longitudinal relaxation. The mechanism for this relaxation is a coupling between the spins and their surrounding thermal reservoir. As time progresses the z component of $\mathbf{M}$ will be restored to its thermal equilibrium value M_0. This effect can be incorporated in eqn (2.27) by writing

$$\frac{\mathrm{d}M_z}{\mathrm{d}t} = \gamma (\mathbf{M} \times \mathbf{B})_z + \frac{M_0 - M_z}{T_1} \tag{2.40}$$

where T_1 is a characteristic relaxation time peculiar to the sample. For the x and y components of $\mathbf{M}$, the effect of relaxation will be to decay them back

to zero as $\mathbf{M}$ returns parallel to the z axis. However the relaxation rate will be increased by additional spin-spin interactions. The time constant for this transverse relaxation, T_2, reflects the rate at which the spins come into thermal equilibrium with themselves. This means T_2 will always be equal to or shorter than T_1, although in liquids the two are nearly always similar. Thus

$$\frac{\mathrm{d}M_x}{\mathrm{d}t} = \gamma(\mathbf{M} \times \mathbf{B})_x - \frac{M_x}{T_2} \qquad (2.41)$$

$$\frac{\mathrm{d}M_y}{\mathrm{d}t} = \gamma(\mathbf{M} \times \mathbf{B})_y - \frac{M_y}{T_2}. \qquad (2.42)$$

In the rotating frame, these equations yield a set of relationships which are known as the Bloch Equations.

$$\frac{\mathrm{d}M_x}{\mathrm{d}t} = \gamma(M_z B_1 \sin \omega_0 t + M_y B_0) - \frac{M_x}{T_2}$$

$$\frac{\mathrm{d}M_y}{\mathrm{d}t} = \gamma(M_z B_1 \cos \omega_0 t - M_x B_0) - \frac{M_y}{T_2}$$

$$\frac{\mathrm{d}M_z}{\mathrm{d}t} = \gamma(-M_x B_1 \sin \omega_0 t - M_y B_1 \cos \omega_0 t) - \frac{M_z - M_0}{T_1} \qquad (2.43)$$

The relaxation times T_1 and T_2 can be used to extract useful information about the state of the nucleus because they are sensitive to terms in the Hamiltonian coupling spins to other spins and the thermal reservoir.

2.2.4 Bloch equations

Equations (2.40), (2.41) and (2.42) can be solved for many situations and are a useful reference point in describing many of the NMR phenomena discussed in this work. If a B_1 field is applied to the equilibrium magnetization for a time t such that the vector $\mathbf{M}$ is rotated 90 degrees onto the transverse plane one can observe the full evolution of the spin system. The solution to the Bloch equations for $\mathbf{M} = M_0 \mathbf{j}$, i.e. directly after the 90° r.f. pulse, are

$$M_x = M_0 \sin \omega_0 t \exp(-t/T_2)$$

$$M_y = M_0 \cos \omega_0 t \exp(-t/T_2)$$

$$M_z = M_0(1 - \exp(-t/T_1)) \qquad (2.44)$$

This oscillating and decaying signal is know as a Free Induction Decay (FID) and the M_y and M_x components are detected by the r.f. coil around the sample. A typical FID is shown in Figure 2.4.

The Fourier transform of the detected signal is a Lorentzian of half width $1/\pi T_2$ in the frequency domain, of which an example is shown in Figure 2.5. In the usual heterodyne detection scheme the peak will appear at an offset frequency $\Delta\omega = \omega_0 - \omega_r$ where ω_r is the reference frequency of the mixing stage.

The integral of the peak in the frequency domain gives the amplitude of the signal immediately after the 90° pulse.

2.2.5 Signal-to-noise ratio

The e.m.f. voltage typically induced in the r.f. coil is of the order of microvolts. This voltage has to compete with the Johnson noise arising from the thermal motion of
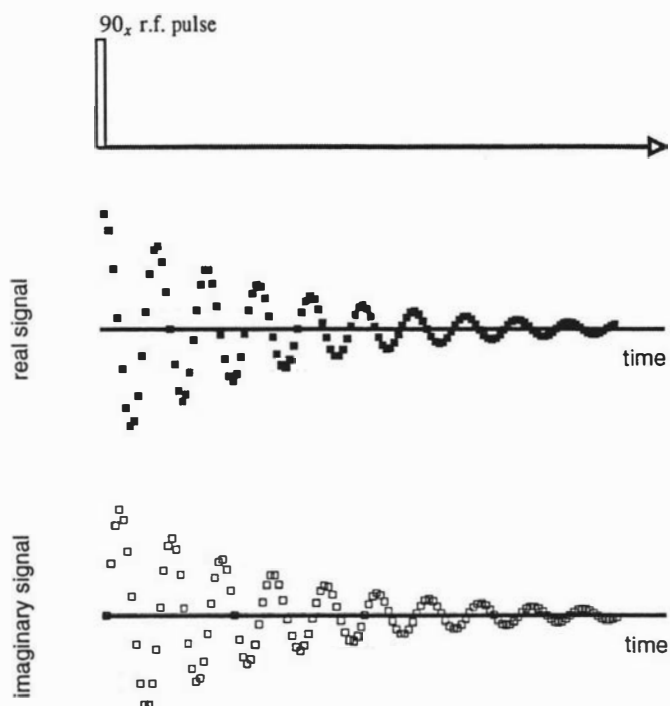
Figure 2.4: A typical Free Induction Decay (FID) following a 90° r.f. pulse where the filled squares represent the real part and the open squares the imaginary part of the signal. The real and imaginary parts are acquired by mixing the receiver signal with an in-phase and quadrature reference frequency respectively.
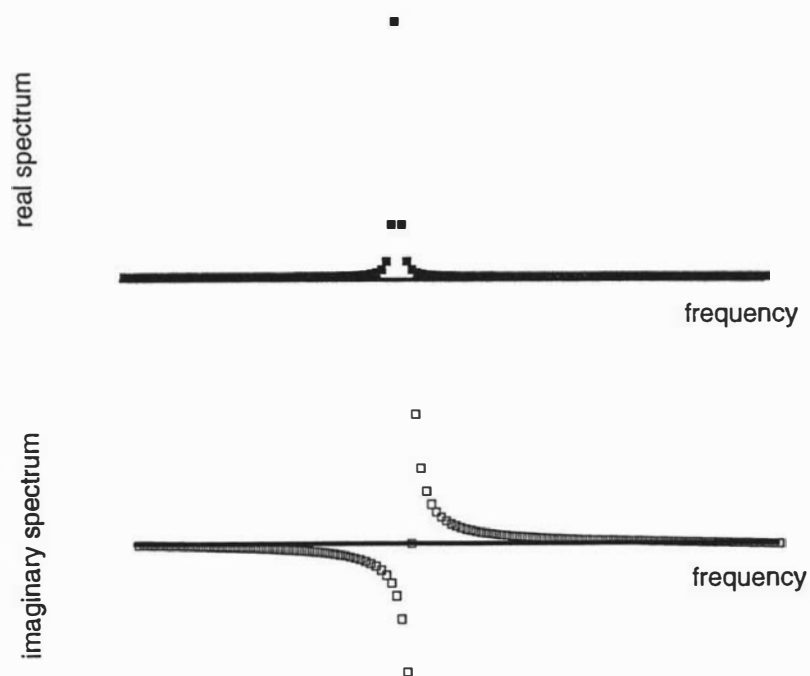
Figure 2.5: Fourier transformation of the FID shown in Figure 2.4 gives the real absorption and imaginary dispersion spectra shown here.

electrons in the coil. The ratio of the signal voltage to the noise voltage (the signal-to-noise ratio) is an important consideration in any NMR experiment. The signal strength is proportional to the size of the magnetization, which is increased by using large magnetic fields and higher gyromagnetic ratio nuclei. The signal is also proportional to the volume of the sample and the "filling factor", the fraction of the r.f. coil volume that contains sample. In the following short calculation, the example numbers given are for the r.f. coil, probe and spectrometer used for the NMR experiments in this thesis.

The r.m.s. noise voltage of an r.f coil is given by[5]

$$\sigma_t = (4k_B T_c \Delta f R F)^{1/2} \tag{2.45}$$

where k_B is Boltzmann's constant, T_c the coil temperature, Δf the receiver bandwidth, R the coil resistance and F the spectrometer noise figure. One must take into account the skin depth[6] when calculating resistances at r.f. frequencies although inductive losses can be ignored for small samples. The resistance is then

$$R = \sigma(\frac{l}{p})(\frac{\mu_r \mu_0 \omega_0 \rho}{2})^{1/2} \tag{2.46}$$

where l is the conductor length, p its circumference, $\mu_R \mu_0$ the conductor permeability and ρ its resistivity. An additional factor σ allows for a reduction in the skin depth due to the close proximity of other conductors and is approximately 5 for a solenoid coil. Hoult and Richards[7] have shown that a solenoidal coil r.f. coil has optimal homogeneity if $2a = L$ where L is the length of the coil. For a coil with N_t turns they show that $l = 6.3 N_t a$ and $p = 4.2 a / N_t$. A five turn copper coil of length 5 mm and radius 2.5 mm therefore has a resistance of 0.4 Ω at 60 MHz. Eqn (2.45) therefore implies about 0.04 μV of noise with our spectrometer, which has a noise figure of around 12.

The signal induced in the coil is[7]

$$S_0 = \omega_0 (B_1/\mathrm{i})_{xy} M_0 V_s \tag{2.47}$$

where $(B_1/\mathrm{i})_{xy}$ is the transverse component of the magnetic field at the center of the receiver coil and is approximately $\mu_0 N_t / \sqrt{2} L$ for a solenoid. Assuming a pure water sample with volume, V_s, is about 1/3 of the r.f. coil volume, our 60 MHz solenoid coil gives about 20 μV peak signal for water at room temperature, where the magnetization per unit volume, M_0, is calculated from eqn (2.25). A signal to noise ratio of around 500 is therefore indicated for the r.f. coil in our probe.

2.3 Nuclear interactions

The dominant interaction of the nucleus is the Zeeman interaction which has an interaction energy in frequency units of γB_0. This frequency is typically in the tens to hundreds of MHz range. However, due to the unusually long coherence times exhibited by spin systems, it is possible to observe weaker nuclear interactions present in the Hamiltonian down to only a few Hz. A brief summary of some of these finer interactions is given here.

2.3.1 Magnetic field inhomogeneity

Although NMR magnets are designed to provide a homogeneous magnetic field region around the sample space, there is inevitably some variation in B_0. Shim coils which provide first, second and higher order corrections to the field are used to minimise these inhomogeneities, but may not be enough, especially where additional field gradients are induced by susceptibility variations from structures in the sample. This is, of course, more likely to occur in microimaging type samples rather than the traditional liquid samples used in the chemistry applications of NMR. The field variations typically lead to a broadening of several Hz in the NMR spectrum. This results in a a decay of the FID more rapid than due to T_2 effects alone.

The resultant decay time is often labelled T_2^* and may be significantly smaller than T_2. However, the coherence loss due to field inhomogeneity is essentially ordered and given the appropriate pulse sequence, such as the spin-echo sequence discussed below, can be reversed. Coherence loss due to relaxation is inherently random and irreversible and therefore cannot be refocused by a pulse sequence. This is distinguished by the label 'homogeneous broadening', as opposed to the reversible inhomogeneous broadening due to magnetic field variations. In structural PGSE experiments, which are the focus of this thesis, there is often significant broadening of this type which must be taken into consideration.

2.3.2 Chemical shift

The nuclei under observation in NMR are surrounded by atomic or molecular electron clouds which interact with the nuclear spin angular momentum. These interactions lead to a shift in Larmor frequency of the nuclei, enabling a kind of chemical fingerprinting used extensively in organic chemistry since the 1950's. This change in frequency, known as the chemical shift, results from magnetic shielding by the surrounding electrons. The shift can be used in PGSE to chemically distinguish different parts of the sample, for example the solvent peak can often be separated from a polymer peak when trying to measure diffusion of semi-dilute entangled polymers. In this way the motion of polymer molecules can be measured separately from the faster diffusing solvent molecules.

2.4 Pulse sequences

In NMR, an experiment can consist of one or many r.f. pulses applied at certain times before signal acquisition. The simplest pulse sequence is the $90°|_x$-acquire sequence described above. However, many other pulse sequences exist, all with a different experimental effect. In this section a brief description of the two varieties of NMR spin echo pulse sequence, used in this thesis, will be described, as well as two simple techniques used to increase the signal-to-noise ratio.

2.4.1 Signal averaging

The signal acquired from a single NMR experiment, in most cases, would have a signal-to-noise ratio too small to enable the extraction of meaningful data. For this reason the NMR experiment is repeated N times and the signals acquired are co-added. The signal strength is then proportional to N while the noise amplitude is

proportional to $N^{1/2}$. As a result, the signal-to-noise ratio increases as $N^{1/2}$. The limiting factor in this process is the repetition time of the experiment compared to the longitudinal relaxation time T_1. The spin system must be given enough time to fully recover its z-axis magnetization between experiments. Normally a time period of 2-3 times T_1 is long enough. The T_1 value for protons in liquids is typically less than a second, allowing many accumulations to occur in an experiment of only a few minutes. However there are situations where experiments lasting several hours are required to accumulate a detectable signal.

In PGSE work, signal averaging is essential due to the inherent nature of the experiment where data is collected by deliberate attenuation of the signal. In some experiments in this thesis up to 8000 transients were averaged in order to accumulate enough signal to make a meaningful measurement.

2.4.2 Phase cycling

Because the signal detected in NMR is relatively weak, any possible decrease in background noise is advantageous. One primary method of coherent noise cancellation is through r.f. phase cycling. Inverting the phase of the r.f. transmitter by 180° will invert the NMR signal but leave any outside signal unaffected. Inverting the phase of the receiver will cause the signal to be subtracted from the data in memory, which, if the signal is inverted, will actually co-add the NMR signal, but subtract background interference. This simple phase cycling can also be modified to cancel any artifacts due to differences between the two quadrature channels. A phase shift of 90° (or 270°) will effectively swap the real and imaginary channels, allowing both phase and magnitude errors between the channels to be cancelled. This four-step CYCLOPS[8] phase sequence of Hoult and Richards is so useful that it forms the basis for most other phase cycling schemes in NMR pulse sequences.

2.4.3 Spin echo

In any NMR magnet there will always be some degree of inhomogeneity in the magnetic field. If there is a spread ΔB_0 in field across the sample, spins on one side of the sample will precess fractionally faster than spins on the other side. The coherence between spins will only last for a time $1/(\gamma \Delta B_0)$ before they become dephased with respect to each other. Each group of spins for which B_0 is essentially constant is often referred to as a "spin isochromat" for which an individual magnetization vector can be assigned, the bulk magnetization being found by summing over all isochromat vectors.

Observed from a rotating frame at ω_0 some spin isochromats will "fan out" away from their initial orientation. This dephasing or fanning out can reduce the bulk magnetization vector at a rate faster than the inherent $1/T_2$ relaxation rate. However this phase loss is inhomogeneous and inherently reversible. Applying a 180° pulse at time τ will invert the phase of all the spins. Now the fast spin isochromats will be lagging and the slow isochromats leading. At a time 2τ after the initial 90° pulse all spins will be back in phase and a Hahn, or Spin, echo[9] will occur. The magnitude of the echo will depend only on the transverse relaxation rate,

$$M_y(2\tau) = M_0 \exp(-2\tau/T_2).$$ (2.48)
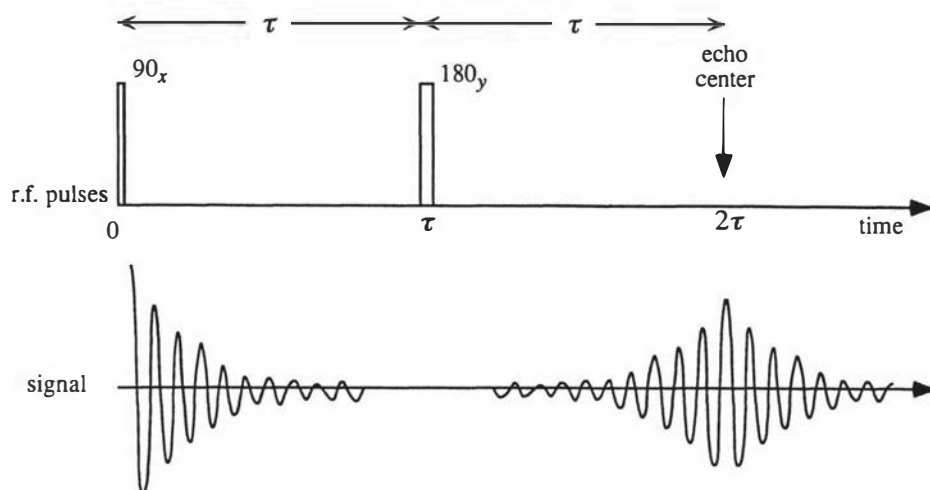
Figure 2.6: The spin echo sequence showing the r.f. pulse sequence and a typical spin echo signal. The decay envelope of the FID is due to T_2^* relaxation whereas the height of the echo is dependent only on T_2 relaxation.

The phase of the 180° r.f. pulse will affect the sign of the echo. A $180°|_y$ pulse produces a positive echo whilst a $180°|_x$ produces a negative echo. This can be utilised to implement a phase cycling scheme as detailed above. The full pulse sequence could be written, $90°|_x - \tau - 180°|_y - \tau -$acquire.

2.4.4   Stimulated echo

In many samples, especially the slow moving or viscous samples, the transverse relaxation time T_2 is considerably longer than the longitudinal relaxation time T_1. In such cases the stimulated echo sequence shown in Figure 2.7 is often used. This stimulated echo sequence[9] allows the transverse magnetization to be stored along the z-axis for a finite time before being tipped back to the transverse plane for signal acquisition. The advantage of this method is that the magnetization only suffers the less severe T_1 relaxation while aligned along the z-axis. This can allow the formation of echoes over time intervals that would be impossible with the spin echo sequence.

A further problem with long time spin echoes on electromagnet systems is that the main field stability is often insufficient to allow phase coherence over time intervals longer than about 100 ms. However, for the stimulated echo sequence, the absolute stability of the main field is unimportant while the magnetization is stored along the z-axis. The method does have disadvantages, only half the magnetization is stored along the longitudinal axis, and hence only half the signal is available at the echo. Also additional spin echoes can be formed from the pulses after the stimulated echo, but these can be removed by using a homospoil gradient pulse to dephase any unwanted transverse magnetization.

The magnitude of the echo is given by

$$M_y(2\tau_1 + \tau_2) = \frac{1}{2}M_0 \exp(-2\tau_1/T_2)\exp(-\tau_2/T_1) \tag{2.49}$$

In this thesis, a stimulated echo sequence was used to collect all the data where the echo time was above 100 ms. In some cases, where T_2 was particularly short, stimulated echoes were used for echo times smaller than this. The spin echo sequence
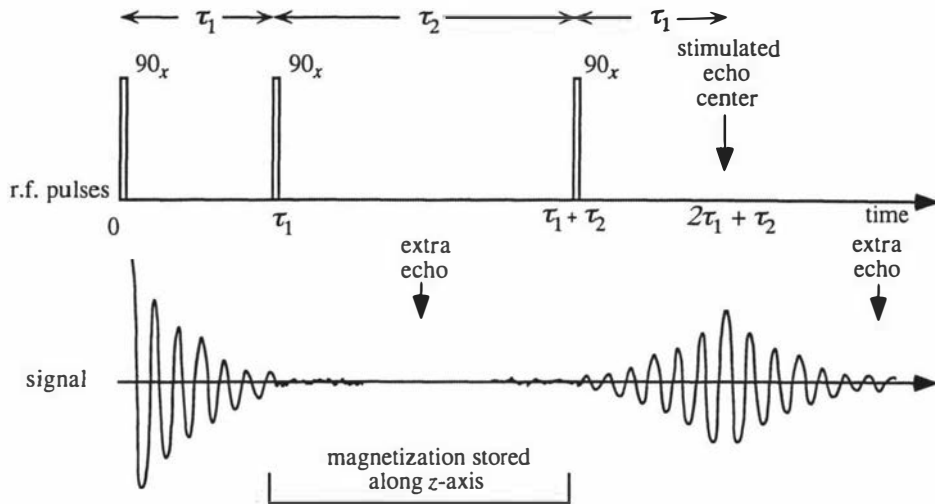
Figure 2.7: The stimulated echo sequence showing the r.f. pulse sequence and a typical signal. The labels "extra echo" indicate the position of possible extra spin echoes resulting from pairs of pulses. The first occurs at a time $2\tau_1$ from the first two r.f. pulses and the second occurs at $\tau_1 + 2\tau_2$ from the second two r.f. pulses. A gradient homospoil pulse is often applied in the interval τ_2 to remove unwanted transverse magnetization.

showed phase instabilities and artificially large attenuation if an echo time over 100 ms was used.

Chapter 3

PGSE Theory

3.1 Magnetic field gradients

In the domain of NMR Spectroscopy many techniques are used to ensure that the polarising magnetic field is as uniform as possible. Several layers of shim coils and many ingenious techniques are used to ensure minimal interference to the acquired NMR spectrum from magnet inhomogeneities. However, in order to extract the spatial dependence of molecules in our sample, it is necessary to deliberately vary the magnetic field across the sample and observe the difference in the resulting Larmor frequencies. These magnetic field gradients are added to the main field by using specially designed gradient coils through which large switchable currents can be passed. In this chapter I shall review the central role of gradients in measuring spin motion and outline the hardware and software used in this thesis to perform such experiments.

3.1.1 Effect of gradients

The magnetic field that is added by the gradient coil is normally much smaller than the magnitude of the main polarising field B_0. Because of this difference in the size of the fields, only components of the gradient which are parallel to $\mathbf{B}_0$ will affect the magnitude of the resulting effective field. The gradient field can be defined as

$$\mathbf{G} = \nabla |\mathbf{B}_0| \qquad (3.1)$$

or in terms of specific components when $\mathbf{B}_0$ is along the z-axis

$$\begin{aligned}
\mathbf{G} &= G_x \hat{\mathbf{i}} + G_y \hat{\mathbf{j}} + G_z \hat{\mathbf{k}} & (3.2) \\
G_x &= \frac{\partial B_z}{\partial x} & (3.3) \\
G_y &= \frac{\partial B_z}{\partial y} & (3.4) \\
G_z &= \frac{\partial B_z}{\partial z}. & (3.5)
\end{aligned}$$

The effect of the gradient is to change the Larmor frequency of nuclear spins in the sample, due to the field magnitude B_0, depending on their spatial position $\mathbf{r}$ such that

$$\omega(\mathbf{r}) = \gamma B_0 + \gamma \mathbf{G} \cdot \mathbf{r}. \qquad (3.6)$$

Eqn (3.6) provides the basis for NMR imaging[10, 11] as well as all the pulsed gradient experiments contained in this thesis. Although gradients were used to measure diffusion coefficients[9, 12] well before the first NMR image was published, it is appropriate to discuss the later briefly before the former.

3.1.2 k-space imaging and the Fourier transform

In a normal free induction decay, if the effects of relaxation are ignored, the acquired signal from an element of volume dV can be written as

$$dS = \exp[i\omega_0 t]\rho(\mathbf{r})dV \tag{3.7}$$

where ω_0 is the Larmor frequency of the spins. If however a gradient is applied then the Larmor frequency of each spin is affected by its spatial position, hence

$$dS(\mathbf{G}, t) = \exp[i\omega(\mathbf{r})t]\rho(\mathbf{r})dV. \tag{3.8}$$

By using eqn (3.6) the signal from this element can be written as

$$dS(\mathbf{G}, t) = \exp[i(\gamma B_0 + \gamma \mathbf{G} \cdot \mathbf{r})t]\rho(\mathbf{r})dV. \tag{3.9}$$

No phase factor is introduced in eqn (3.9) because fixed phase offsets are nearly always removed by either autophasing the image or taking the magnitude at the end of processing. The absence of relaxation in eqn (3.9) is unimportant if the dephasing due to gradients is stronger than dephasing due to T_2. In fact this is a necessary condition for obtaining a 'high-resolution' image. A further simplification can be made by utilising the 'on-resonance' condition, where the acquired signal is mixed with the original γB_0 frequency. This is called heterodyne mixing and is employed in all high frequency spectrometers today, although often one or more intermediate frequencies are used to step the signal down to the 'audio' range. The volume integral of eqn (3.9) yields

$$S(\mathbf{G}, t) = \int\int\int \rho(\mathbf{r}) \exp[i\gamma \mathbf{G} \cdot \mathbf{r}t]d\mathbf{r}. \tag{3.10}$$

In fact this equation is no more than a Fourier transform between $\mathbf{r}$ and some reciprocal space. A reciprocal space vector $\mathbf{k}$ can be defined as[13]

$$\mathbf{k} = \frac{1}{2\pi}\gamma \mathbf{G}t \tag{3.11}$$

then eqn (3.10) can be written as

$$S(\mathbf{k}) = \int\int\int \rho(\mathbf{r}) \exp[i2\pi\mathbf{k} \cdot \mathbf{r}]d\mathbf{r} \tag{3.12}$$

which shows clearly the Fourier relationship between $\mathbf{r}$ and $\mathbf{k}$. The inverse transform can easily be shown to be

$$\rho(\mathbf{r}) = \int\int\int S(\mathbf{k}) \exp[-i2\pi\mathbf{k} \cdot \mathbf{r}]d\mathbf{k}. \tag{3.13}$$

Therefore one can reconstruct the original image from $S(\mathbf{k})$ by applying eqn (3.13) and obtaining $\rho(\mathbf{r})$ as shown in Figure 3.1.

In effect, the gradient "spreads" out the signal from the sample in the frequency domain. For a single gradient strength and direction, the frequency profile is the one
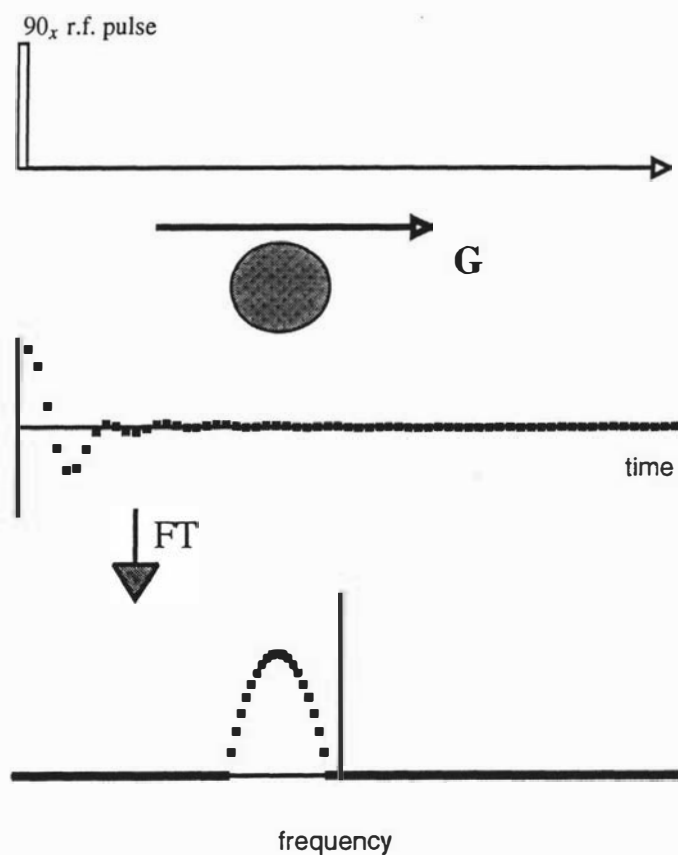
Figure 3.1: Diagram showing the NMR time domain signal acquired for a uniform cylindrical sample with the gradient direction as indicated above. The frequency spectra obtained by Fourier transforming the time domain signal corresponds to the spin density function projected along the direction of the gradient **G**.

dimensional density projection of the sample along the gradient direction. As the gradient is increased, the profile is more "spread out" across the frequency spectrum, revealing finer details. However, the maximum resolution is limited, because the larger spectral bandwidth would include more noise. Eventually the signal is so spread out, that the noise dominates over the whole spectrum. Often other 'signal-decreasing' effects come into play before this situation occurs. Some of them are discussed further in Section 6.5.

3.2   Gradients and spin motion

In direct contrast to NMR imaging, where it is the *static* position of molecules that is of interest, we are instead interested in the *dynamic* movement of molecules over a certain time interval. The specific starting and finishing position of the molecules are unknown but any displacement can be detected.

In Section 3.1.2 it was noted that any motion of the molecules along the gradient direction can lead to fluctuations in the Larmor frequency and some distribution of residual phase shifts. In fact Hahn[9] noted the effect of self-diffusion on spin echoes in his original 1950 paper. The Carr and Purcell sequence[12] utilising multiple echoes was proposed in order to minimise such effects.

In this thesis we are concerned with measuring the motion of molecules. It turns out that the effect that the diffusion process has on the NMR signal, in the presence of a gradient, is both measurable and useful.

3.2.1   Gradients and diffusion

Self-diffusion can classically be characterised in one dimension as a series of hops of distance ξ with a time τ_s between steps. The hops have equal probability of being to the left or right so that the displacement is[12]

$$Z(n\tau_s) = \sum_{i=1}^{n} \xi a_i \tag{3.14}$$

after a time $t = n\tau_s$. The variable a_i is a number equal to ± 1 to represent a jump to the left or right. By squaring and taking the ensemble average it can be shown that for $t = n\tau_s$

$$\overline{Z^2(t)} = 2Dt \tag{3.15}$$

where

$$D = \xi^2/2\tau_s \tag{3.16}$$

If one introduces a magnetic field gradient along the z diffusion direction, a phase shift will be acquired due to the changing precession frequency as the spin moves. If we assume that $Z(t) = 0$ at $t = 0$ and ignore the constant Larmor precession due to B_0, then the change in frequency of the molecules, from eqn (3.6), will be

$$\Delta\omega(t) = \gamma G Z(t) \tag{3.17}$$

and the phase shift, $\Delta\phi$, acquired by the spin after a time $t = n\tau_s$, using eqn (3.14) will be[12]

$$
\begin{aligned}
\Delta\phi(t) &= \sum_{m=1}^{n} \gamma G\tau_s \sum_{i=1}^{m} \xi a_i \\
&= \gamma G\tau_s \xi \sum_{i=1}^{n} (n+1-i)a_i.
\end{aligned}
\tag{3.18}
$$

The ensemble average

When dealing with a real sample with an Avogadro's number of spins we need some technique for calculating the final signal. Typically there is an echo sequence involved and so, with the exception of the steady gradient case which follows, the echo signal is labelled E. Because the diffusion process is random each spin will acquire a different phase shift. To calculate the final result of adding all the spin vectors, $e^{i\Delta\phi}$, together, each with a phase shift $\Delta\phi$, an ensemble average over the whole sample is used.

In order to find the coefficient by which the ensemble-averaged transverse magnetization will be attenuated we need to calculate $\overline{\exp(i\Delta\phi)}$, additional attenuation due to T_2 relaxation effects will be ignored. Therefore

$$
\overline{\exp(i\Delta\phi)} = \int_{-\infty}^{\infty} P(\Delta\phi) \exp(i\Delta\phi) \mathrm{d}(\Delta\phi)
\tag{3.19}
$$

where $P(\Delta\phi)$ is the distribution of phase shifts $\Delta\phi(t)$. This integral is most simply done by assuming that the distribution of phase shifts $P(\Delta\phi)$ will be Gaussian[14] which makes eqn (3.19) yield

$$
\overline{\exp(i\Delta\phi)} = \exp(-\overline{\Delta\phi^2}/2)
\tag{3.20}
$$

By squaring eqn (3.18) and taking an ensemble average one obtains

$$
\begin{aligned}
\overline{\Delta\phi^2} &= \gamma^2 G^2 \tau_s^2 \xi^2 \sum_{i=1}^{n} (n+1-i)^2 \\
&= \gamma^2 G^2 \tau_s^2 \xi^2 \sum_{j=1}^{n} j^2 \\
&= \frac{1}{3} \gamma^2 G^2 \tau_s^2 \xi^2 n^3
\end{aligned}
\tag{3.21}
$$

where $\sum_{j=1}^{n} j^2 = \frac{1}{3}n^3$ is evaluated by assuming that n is large. Substituting this result and eqn (3.16) into eqn (3.20) one finds the signal attenuation due to diffusion in the presence of a steady gradient is[12]

$$
S(t) = \overline{\exp(i\Delta\phi)} = \exp(-\frac{1}{3}\gamma^2 G^2 D t^3).
\tag{3.22}
$$

Often in NMR there are inhomogeneities in the local field throughout the sample, as discussed in Section 2.3.1, and these can be refocused though the use of a spin echo. If a 180° pulse is applied at a time t after the initial 90° excitation pulse then an echo will form at $2t$.
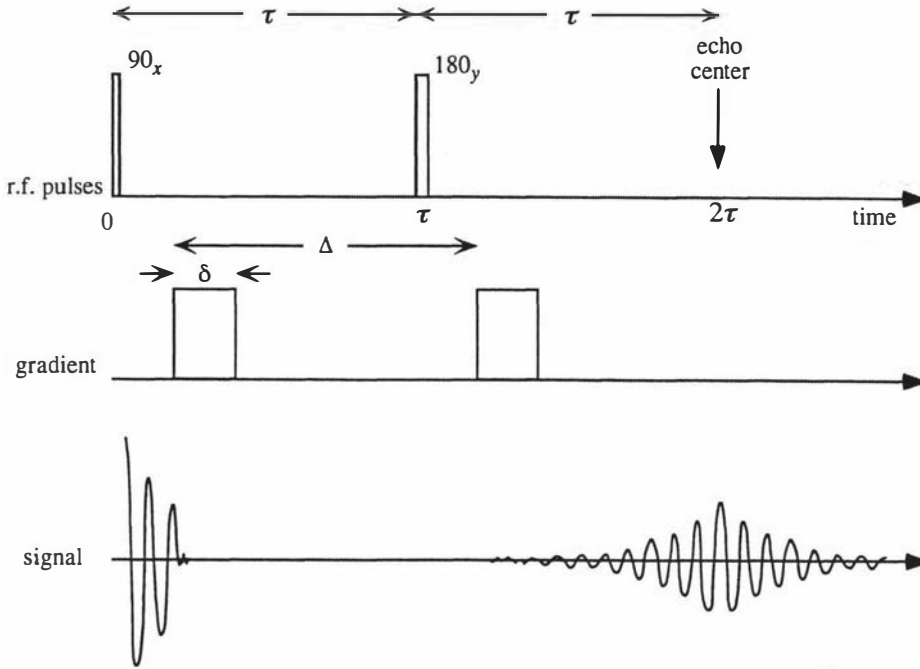
Figure 3.2: The pulsed gradient spin echo sequence (PGSE) with the r.f. and gradient pulses shown on separate time lines. The attenuation of the echo acquired at time 2τ due to the presence of the gradient pulses is given by eqn (3.25).

The signal attenuation of the echo occurring at $2t$ in the presence of a steady gradient is then[12]

$$
\begin{aligned}
S(2t) = \overline{\exp(i\Delta\phi)} &= \exp(-\frac{2}{3}\gamma^2 G^2 D t^3) \\
&= \exp(-\frac{1}{12}\gamma^2 G^2 D (2t)^3)
\end{aligned}
\tag{3.23}
$$

3.2.2   Pulsed field gradients

A major inconvenience of the steady gradient method[15, 16] is that the gradient is applied to the sample for the whole experiment. In particular for the times when the r.f. pulses are being applied, and when the signal is being acquired. The resultant spread of the Larmor spectrum and the effective bandwidth of the receiver and transmitter will limit the maximum strength of gradient that can be applied to the sample. It is however easy to modify the hardware so that the gradients can be applied as pulses at the appropriate time, and a spin echo sequence can be used to form an echo at an appropriate time when the gradients are off. This modification, called Pulsed Gradient Spin Echo (PGSE), first suggested by McCall, Douglas and Anderson[16] in 1963, was demonstrated by Stejskal and Tanner[17] in 1965, and is shown in Figure 3.2. If the gradient pulses have a duration δ and a separation Δ then the mean square phase shift is given by[18, 17, 19]

$$
\overline{\Delta\phi^2} = 2\gamma^2 g^2 \delta^2 D(\Delta - \delta/3)
\tag{3.24}
$$

The echo amplitude at 2τ will be attenuated by both relaxation and the gradient. The effects of any T_2 relaxation can be removed by normalising the echo signal to

its value with no gradient applied. The ratio $S(g)/S(0)$ is often labelled $E(g)$. The signal strength of the echo at 2τ is therefore given by

$$E(g) = \exp(-\gamma^2 g^2 \delta^2 D(\Delta - \delta/3)) \quad (3.25)$$

which is the well known Stejskal-Tanner equation[17]. A plot of the natural logarithm of the echo against $\gamma^2 g^2 \delta^2(\Delta - \delta/3)$ will give a straight line with a slope of $-D$ for a sample exhibiting unrestricted Brownian diffusion. This type of graph is often referred to as a Stejskal-Tanner plot and has been used extensively to measure self-diffusion coefficients from PGSE experiments[20, 21, 22]. The effect of any relaxation can be removed by normalising the echo signal to the value when no gradient is applied.

Eqn (3.25) has also been derived by Stepisnik[23] using a density matrix formalism that is especially useful for finding expressions for $E(q)$ for oscillating rather than pulsed gradients.

3.2.3   Stimulated echo

The PGSE experiment can be altered to take advantage of the stimulated echo sequence[24] of Section 2.4.4 as shown in Figure 3.3. The echo attenuation is still given by eqn (3.25) but the normal reduction of signal by a factor of two is still present. However the spins now only suffer T_2 relaxation during the two periods τ_1. During the longer period τ_2 the spins suffer the normally less severe T_1 relaxation. However the gradient pulses can only be applied during the intervals where the magnetization is in the transverse plane which often limits the duration of τ_1. In some recent experiments, utilising the fringe field of superconducting magnets[25] to obtain large field gradients, this pulse sequence has been used to define narrow gradient pulses. Five pulse variations[26] of the stimulated echo sequence are used in the fringe field experiments to remove relaxation dependance of the echo signal.

3.3   PGSE, scattering and q-space

In order to discuss diffusion in PGSE experiments certain tools are needed to describe the motion of the particles. A molecule i can be characterized by a function $\mathbf{r}_i(t)$ which describes its position at any time t. By taking an ensemble average over all particles we can find the probability of the particle moving from an initial position $\mathbf{r}$ to a position $\mathbf{r}'$ a time t later. These probabilities form the Van Hove correlation function[27] $P(\mathbf{r}|\mathbf{r}', t)$ a well known function in scattering theory. This function tells the probability of finding any scattering center at $(\mathbf{r}', t)$ if there was one at $(\mathbf{r}, 0)$. However this function describes relative motion between particles as well as the self-motion. The correct function for use in PGSE is the self-correlation function[28] $P_s(\mathbf{r}|\mathbf{r}', t)$ which gives the probability of a molecule initially at $\mathbf{r}$ moving to $\mathbf{r}'$ after a time t. This inherent labelling of the molecules by PGSE NMR is only shared by the incoherent fraction of polarised neutron scattering. All other forms of dynamic measurement, such as dynamic light scattering, measure the Van Hove correlation function.
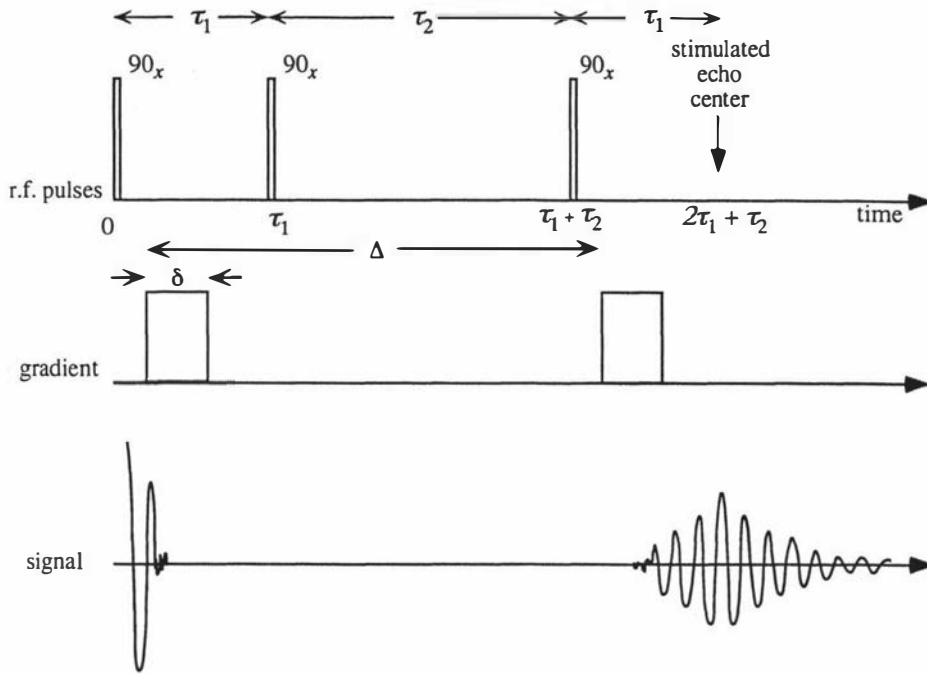
Figure 3.3: The stimulated echo variation of the PGSE sequence. The attenuation of the echo is given by eqn (3.25).

3.3.1   The conditional probability function and the average propagator

Fick's law

The probability of finding a particle at position $\mathbf{r}'$ at a time t, $\Psi(\mathbf{r}', t)$, is given by

$$\Psi(\mathbf{r}', t) = \int \Psi(\mathbf{r}, 0) P_s(\mathbf{r}|\mathbf{r}', t) \mathrm{d}\mathbf{r} \tag{3.26}$$

The diffusion process can be described by Fick's law[29] which sets the particle concentration gradient proportional to the particle flux per unit area per unit time. Although there is no net concentration gradient for self-diffusion, a description using $\Psi(\mathbf{r}', t)$ is possible as it describes a sort of ensemble-averaged probability concentration for a single particle. Fick's law can therefore be written in terms of P_s as

$$\frac{\partial P_s}{\partial t} = D\nabla'^2 P_s \tag{3.27}$$

where the constant of proportionality, D, is the self-diffusion coefficient. The initial condition required is.

$$P_s(\mathbf{r}|\mathbf{r}', 0) = \delta(\mathbf{r}' - \mathbf{r}) \tag{3.28}$$

Unrestricted self-diffusion

A solution to eqn (3.27) can easily be obtained for the special case of unrestricted self-diffusion[18]. The initial boundary condition of eqn (3.28) combined with the condition that $P_s \to 0$ as $\mathbf{r}' \to \infty$ gives

$$P_s(\mathbf{r}|\mathbf{r}', t) = \frac{1}{(4\pi Dt)^{3/2}} \exp[-\frac{(\mathbf{r}' - \mathbf{r})^2}{4Dt}] \tag{3.29}$$

Notice P_s is independent of the initial position $\mathbf{r}$ and depends only on the net displacement $(\mathbf{r}' - \mathbf{r})$. The vector $\mathbf{r}' - \mathbf{r}$ can be referred to as $\mathbf{R}$, the dynamic displacement. A useful function to describe is the averaged propagator[30] $\overline{P_s}(\mathbf{R}, t)$ which gives the probability of any particle having a displacement $\mathbf{R}$ over a time t. This function can be evaluated by

$$\overline{P_s}(\mathbf{R}, t) = \int P_s(\mathbf{r}|\mathbf{r} + \mathbf{R}, t)\rho(\mathbf{r})d\mathbf{r} \tag{3.30}$$

For the case of unrestricted self-diffusion it can then be written that

$$\overline{P_s}(\mathbf{R}, t) = \frac{1}{(4\pi Dt)^{3/2}} \exp[-\frac{\mathbf{R}^2}{4Dt}] \tag{3.31}$$

In PGSE the dynamic measurement is only made along the gradient (z) direction and hence we are only concerned with motions in one dimension. Integrating over the other two dimensions eqn (3.31) becomes

$$\overline{P_s}(Z, t) = \frac{1}{(4\pi Dt)^{1/2}} \exp[-\frac{Z^2}{4Dt}] \tag{3.32}$$

The ensemble averaged mean-square dynamic displacement can also be evaluated from the averaged propagator and yields

$$\begin{aligned} \overline{Z^2} &= \int_{-\infty}^{\infty} Z^2 \overline{P_s}(Z, t)\mathrm{d}Z \\ &= 2Dt \end{aligned} \tag{3.33}$$

as expected.

3.3.2 The narrow-pulse approximation

If the gradient pulse is applied to the sample over a short enough time period δ such that the molecules do not move significantly over the period δ then a useful approximation can be made. For a spin at position $\mathbf{r}$ when the first gradient pulse is applied, a phase shift $\gamma\delta\mathbf{g} \cdot \mathbf{r}$ will be acquired. This phase shift will be inverted by the 180° r.f. pulse. Suppose the molecule moves to a position $\mathbf{r}'$ at the time the second gradient pulse is applied. The net phase shift acquired by the spin due to the gradient pulses would then be $\gamma\delta\mathbf{g} \cdot (\mathbf{r}' - \mathbf{r})$. To calculate the ensemble averaged echo signal the phase term $\exp[i\gamma\delta\mathbf{g} \cdot (\mathbf{r}' - \mathbf{r})]$ must be weighted by the probability for a spin to start at $\mathbf{r}$, namely $\rho(\mathbf{r})$, and the probability for it to move from $\mathbf{r}$ to $\mathbf{r}'$, namely $P_s(\mathbf{r}|\mathbf{r}', t)$. The echo signal will therefore be[18]

$$E(\mathbf{g}) = \int \rho(\mathbf{r}) \int P_s(\mathbf{r}|\mathbf{r}', \Delta) \exp[i\gamma\delta\mathbf{g} \cdot (\mathbf{r}' - \mathbf{r})]d\mathbf{r}'d\mathbf{r} \tag{3.34}$$

assuming any relaxation effects are normalized out. In the static imaging discussed earlier a vector $\mathbf{k}$ was introduced to describe a reciprocal space to the molecular positions. For PGSE, as well, a vector $\mathbf{q}$ can be used to describe a reciprocal space to displacement where[31]

$$\mathbf{q} = \frac{\gamma\delta\mathbf{g}}{2\pi} \tag{3.35}$$

This allows eqn (3.34) to be rewritten

$$E(\mathbf{q}) = \int \rho(\mathbf{r}) \int P_s(\mathbf{r}|\mathbf{r}', \Delta) \exp[\mathrm{i}2\pi\mathbf{q} \cdot (\mathbf{r}' - \mathbf{r})]\mathrm{d}\mathbf{r}'\mathrm{d}\mathbf{r} \qquad (3.36)$$

It is interesting to note that eqn (3.36) is equivalent to the neutron scattering function of the incoherent fraction, namely

$$S_{\mathrm{incoherent}} = \overline{N^{-1}\sum_i \exp[\mathrm{i}2\pi\mathbf{q} \cdot (\mathbf{r}_i(t) - \mathbf{r}_i(0))]} \qquad (3.37)$$

This is in contrast to the coherent neutron scattering function

$$S_{\mathrm{coherent}} = \overline{N^{-2}\sum_i \sum_j \exp[\mathrm{i}2\pi\mathbf{q} \cdot (\mathbf{r}_j(t) - \mathbf{r}_i(0))]} \qquad (3.38)$$

which is sensitive to relative motions between molecules as discussed before. The ability of PGSE to measure the self-motion of molecules is of major importance to the technique.

The concept of reciprocal $\mathbf{q}$-space can easily be seen by making the substitution $\mathbf{r}' = \mathbf{r} + \mathbf{R}$ allowing eqn (3.36) to be rewritten[18, 31]

$$E(\mathbf{q}) = \int \overline{P_s}(\mathbf{R}, \Delta) \exp[\mathrm{i}2\pi\mathbf{q} \cdot \mathbf{R}]\mathrm{d}\mathbf{R} \qquad (3.39)$$

Eqn (3.39) represents a simple Fourier relationship between $E(\mathbf{q})$ and $\overline{P_s}(\mathbf{R}, \Delta)$[32, 31]. In fact $\mathbf{q}$ is the reciprocal space to $\mathbf{R}$. By acquiring signal in $\mathbf{q}$-space we can image $\overline{P_s}(\mathbf{R}, \Delta)$, just as acquiring signal in $\mathbf{k}$-space allows one to image $\rho(\mathbf{r})$.

For the one dimensional case where $\mathbf{q}$ is aligned along the z-axis eqn (3.39) is

$$E(q) = \int \overline{P_s}(Z, \Delta) \exp[\mathrm{i}2\pi qZ]\mathrm{d}Z \qquad (3.40)$$

By combining eqn (3.40) and eqn (3.32) one gets

$$E(q) = \int_{-\infty}^{\infty} \frac{1}{(4\pi Dt)^{1/2}} \exp[-\frac{Z^2}{4Dt}] \exp[\mathrm{i}2\pi qZ]\mathrm{d}Z \qquad (3.41)$$

The Fourier transform of a Gaussian is itself a Gaussian giving

$$\begin{aligned} E(q) &= \exp[-4\pi^2 q^2 D\Delta] \\ &= \exp[-\gamma^2 \delta^2 g^2 D\Delta] \end{aligned} \qquad (3.42)$$

as in the Stejskal-Tanner equation, except $(\Delta - \delta/3)$ is replaced by Δ as one would expect if $\delta \ll \Delta$. Using eqn (3.33) this result can be expressed in terms of the mean-squared displacement of the molecules as[18]

$$\begin{aligned} E(q) &= \exp[-2\pi^2 q^2 \overline{Z^2}] \\ &= \exp[-\tfrac{1}{2}\gamma^2 \delta^2 g^2 \overline{Z^2}] \end{aligned} \qquad (3.43)$$

Throughout this thesis the echo attenuation function will be referred to as $E(q)$, although strictly speaking, it is a function of Δ as well. This is done deliberately to emphasise the q-space approach, taken by this author, in analysing PGSE data, where q is varied and Δ held constant. This approach is in contrast to the traditional approaches that were taken by other workers in this field.

3.4 Hardware

3.4.1 FX-60

All the PGSE experiments performed in this thesis were carried out on the JEOL FX-60 spectrometer in our laboratory. A home-built sequencer was added to the machine as a result of developing an NMR imaging system[33, 34, 35]. The high gradient PGSE probe was also home-built and features a quadrupolar gradient coil capable of producing 1.21 T m^{-1} A^{-1}. A modified KEPCO current supply[35] is capable of supplying up to 15 A to the gradient coil with nominally less than 0.006% noise. For currents less than 10 A the gradient pulses are generally well matched, but for experiments requiring greater currents the PGSE-MASSEY technique described later must be used.

The r.f. coil is a solenoid of length 5 mm providing excellent signal-to-noise for most samples. The sample tube sits directly inside the r.f. coil and has a 4 mm outside diameter and a 3.2 mm internal diameter providing good volume filling of the r.f. coil space. A 70 W r.f. power amplifier enables short 90° pulse times of around 7 μs. An external deuterium lock keeps the water-cooled electromagnet stable, although for echo times greater than 100 ms a stimulated echo sequence is normally used.

Temperature control was available but generally not used, the ambient temperature inside the probe of 28 °C was stable enough for most experiments.

A TI-980A computer provides the means for controlling the spectrometer and runs a variety of factory supplied and home-modified software to implement the various pulse sequences required. The PGSE version enables the user to specify all timing parameters for a series of experiments which are then run sequentially with the data being transferred to another computer between each run. Additionally an "ngain" parameter can be specified for each experiment increasing the number of acquisitions for the particular run as required. Good use of this feature dramatically reduces the time required to perform some of the experiments performed in the experimental sections of this thesis.

The signal data is acquired on a single A-D converter and so a time-sharing feature was added to enable quadrature acquisition. While this feature is adequate to enable coherent noise cancellation through the techniques outlined in Section 2.4.2, it was a limiting aspect when trying to implement PGSE-MASSEY which requires simultaneous quadrature acquisition.

The time domain data is transferred via a serial port to an external computer, initially a Hitachi PC clone, and later a Macintosh II, to facilitate automated analysis of the spectra. On the Macintosh version of this software, written by the author, the data is Fourier transformed and the necessary peak integration performed to reveal the echo signal strength as required. The data is saved in a file for use by the PGSEPLOT analysis program developed as part of this thesis. This software allows the user to view the data and perform various linear and non-linear fits to the data. Not only is the Stejskal-Tanner equation available for fitting, but also a full range of the various restricted diffusion equations found in this thesis. Spurious data points can easily be removed from the fit by the user, with the final graph including all fit parameters. This software was used extensively throughout this thesis. Source code can be obtained for viewing by contacting the author through e-mail at A.Coy@massey.ac.nz

At the time of writing the TI-908A computer has been replaced by a separate TECMAG LEO/J sequencer run from a Macintosh computer. However none of the experiments in this thesis were performed on this new hardware.

3.4.2   AMX-300

The NMR images in Section 6.4 and Section 6.5 were acquired on the Bruker AMX300 system in our laboratory. Routine pulse sequences supplied by the manufacturer were used with the final data being transferred to Macintosh computers to enable further analysis and hard copy output.

3.4.3   GX-270

The JEOL GX-270 spectrometer was used to provide simultaneous quadrature acquisition for the PGSE-MASSEY experiments in this thesis and its specific use is described in Section 5.2.

Chapter 4

PGSE and restricted diffusion

In many samples a diffusing liquid will encounter boundaries to its motion. These may be hard walls impermeable to the molecule, walls with relaxation sinks, walls with holes or softer boundaries through which a molecule diffuses at a slower rate. In any case the conditional probability function $P_s(\mathbf{r}|\mathbf{r}', \Delta)$ will be altered. Since the echo attenuation function $E(q)$ in PGSE is related to the conditional probability function through eqn (3.36) we can often determine structural parameters associated with the boundaries from $E(q)$. In this chapter we will discuss the PGSE theory associated with fully enclosing boundaries which restrict diffusion. By using the narrow-gradient-pulse formalism presented in Section 3.3 it has been shown[31] that PGSE is an imaging experiment in its own right. This q-space imaging principle is a fundamental feature of the work presented in this thesis.

It is important to remember that the PGSE method collects signal from the whole sample and that a real sample is made up of one particular heterogeneous structure repeated homogenously through the full sample space. In fact this feature allows a form of signal averaging not possible in NMR microscopy. One acquires the signal from tens or millions of samples in one experiment. As long as the fundamental structure is homogeneous then the signal acquired would be the same as if there were only one instance of the structure.

4.1 Long time limit case for average propagator

The concept of q-space imaging is best introduced by considering the long time limit case when $\Delta \to \infty$. If the molecules are contained by some boundaries to their motion then the long time limit case implies that they would no longer have any memory of their starting position. In effect, the multiple collisions with the boundaries mean that the molecule is equally likely to be found anywhere inside the container irrespective of its initial starting position. If the dimensions of the container is a then the long time limit case can be estimated as when $\Delta \gg a^2/D$. In this case the molecules have an equal probability of moving to any position in the container. Therefore, $P_s(\mathbf{r}|\mathbf{r}', \infty)$ is equivalent to the starting density $\rho(\mathbf{r}')$, and the average propagator can be written from eqn (3.30) as

$$\overline{P_s}(\mathbf{R}, \infty) = \int \rho(\mathbf{r} + \mathbf{R})\rho(\mathbf{r})\mathrm{d}\mathbf{r} \qquad (4.1)$$

This equation can be recognised as the autocorrelation function of the molecular density. For this special case the echo attenuation function takes on a special form

when the narrow pulse approximation is used. By using $\rho(\mathbf{r}')$ for the conditional probability function in eqn (3.34) we can write

$$
\begin{aligned}
E_\infty(\mathbf{q}) &= \int\int \rho(\mathbf{r})\rho(\mathbf{r}')\exp[\mathrm{i}2\pi\mathbf{q}\cdot(\mathbf{r}'-\mathbf{r})]\mathrm{d}\mathbf{r}'\mathrm{d}\mathbf{r} \\
&= \int \rho(\mathbf{r})\exp[\mathrm{i}2\pi\mathbf{q}\cdot\mathbf{r}]\mathrm{d}\mathbf{r}\int \rho(\mathbf{r}')\exp[\mathrm{i}2\pi\mathbf{q}\cdot\mathbf{r}']\mathrm{d}\mathbf{r}' \\
&= S^*(\mathbf{q})S(\mathbf{q}) \\
&= |S(\mathbf{q})|^2
\end{aligned}
\tag{4.2}
$$

where $E_\infty(\mathbf{q})$ represents the long time limit of $E(\mathbf{q})$.

The expression $S(\mathbf{q})$ is in fact the reciprocal lattice acquired by a conventional k-space imaging experiment. This relationship is remarkable because it says the long time limit echo attenuation function is the same as the modulus squared of the reciprocal lattice. This tells us that it is possible to image a sample using PGSE, however, with the disadvantage that phase information is lost. The relationship between the Fourier transform of the autocorrelation function and the frequency power spectrum is known as the Wiener-Khintchine theorem[36]. Its use in PGSE was initially pointed out by Cory and Garroway[32] who inverted the echo attenuation data to reveal the average propagator and hence the autocorrelation of the density function of the sample, in this case yeast cells, that they were observing. PGSE q-space imaging does have one advantage over conventional NMR microscopy, the resolution is not limited by signal-to-noise considerations because the signal is collected from the whole sample, not just a single voxel. The only limitation is the size of the gradient pulses and the condition that they are well matched. In this thesis experiments have been performed where structural information has been obtained at resolutions beyond the capabilities of NMR microscopy to date.

4.1.1 Parallel plane pore

For molecules trapped between two parallel planes in the gradient direction with separation a, the density function $\rho(z)$ is a hat function of width a. The Fourier transform of a hat function gives $S(q)$, a sinc function[12], as shown in Figure 4.1.

$$
\begin{aligned}
S(q) &= \int_{-a/2}^{a/2} \frac{1}{a}\exp(\mathrm{i}2\pi qz)\,\mathrm{d}z \\
&= \frac{\sin(\pi qa)}{\pi qa} = \mathrm{sinc}(\pi qa)
\end{aligned}
\tag{4.3}
$$

Thus from eqn (4.2) one gets[32]

$$
E_\infty(q) = |\mathrm{sinc}(\pi qa)|^2 = \frac{2[1-\cos(2\pi qa)]}{2\pi qa}
\tag{4.4}
$$

which is the Fourier transform of the long time limit average propagator $\overline{P_s}(Z,\infty)$. Of most interest in eqn (4.4) is the null at $q=a^{-1}$ analogous to the optical diffraction pattern of a single slit. These "diffraction-like" effects in PGSE, where the echo signal passes through a minimum, was first observed during the experimental work for this thesis in both the parallel plane case[37] and for the more complicated porous case[38] discussed later. It is also important to notice that $E_\infty(q)$ is now time independent as expected. The autocorrelation of the hat function gives

$$
\overline{P_s}(Z,\infty) = \begin{cases} (a+Z)/a^2 & -a \le Z \le 0 \\ (a-Z)/a^2 & 0 \le Z \le a \end{cases}
\tag{4.5}
$$
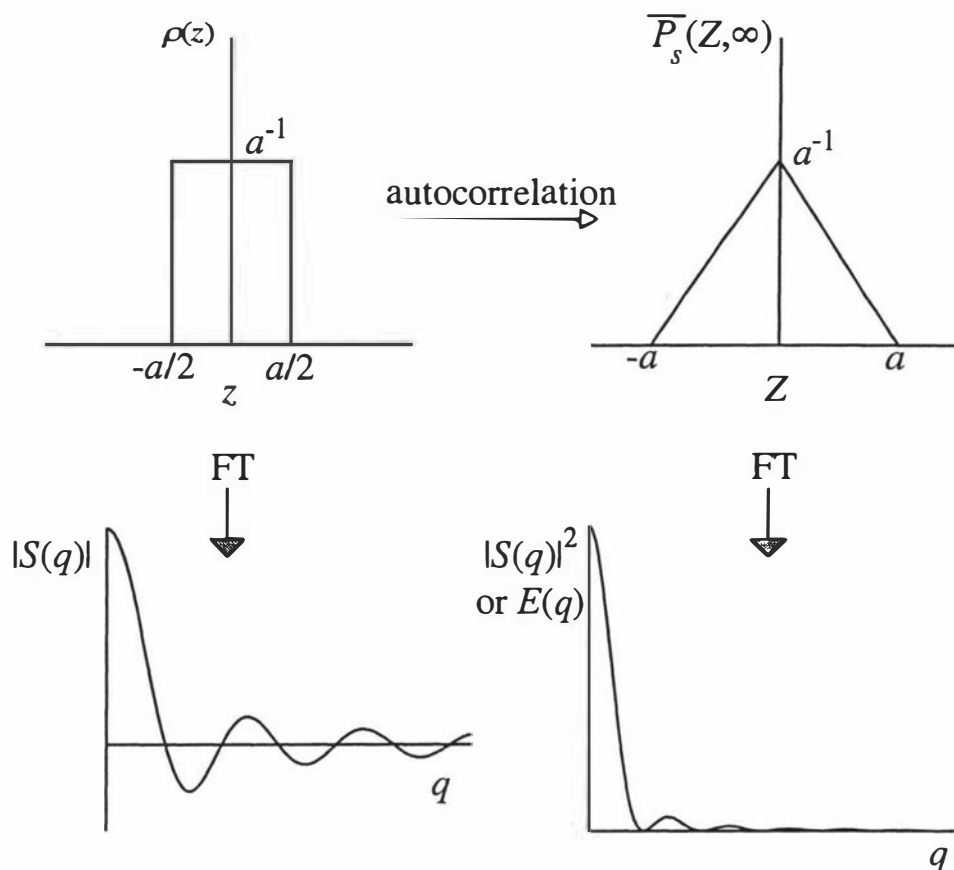
Figure 4.1: Diagram, adapted from Figure 7.4, ref [31], showing the relationship between the density function, $\rho(z)$, and the echo attenuation function, $E(q)$ of a sample. $\rho(z)$ is shown top left for molecules confined to rectangular box, with the corresponding Fourier transform $S(q)$, a sinc function, the signal that would be acquired in an imaging experiment on the sample. Top right shows the long time limit averaged propagator $\overline{P_s}(Z, \infty)$, equivalent to the autocorrelation of $\rho(z)$. The Fourier transform of $\overline{P_s}(Z, \infty)$ gives $E(q)$, a sinc^2 function shown bottom right. Through the Wiener-Khintchine theorem it can be seen that $E(q)$ is the power spectrum of $S(q)$, or, by analogy to diffraction, the diffraction pattern of a single slit described by $\rho(z)$.

The mean squared displacement of this autocorrelation function would then be

$$\overline{Z^2} = \int_{-\infty}^{\infty} \overline{P_s}(Z,\infty)\mathrm{d}Z = \frac{1}{6}a^2 \tag{4.6}$$

which would imply that for $q \ll a^{-1}$ the molecules would seem to have an apparent diffusion coefficient of

$$D_{\mathrm{app}} = \frac{\overline{Z^2}}{2\Delta} = \frac{a^2}{12\Delta} \tag{4.7}$$

which would lead to an initial echo attenuation of

$$E_\infty(q) \approx \exp(-4\pi^2 q^2 D_{\mathrm{app}}\Delta) \approx \exp(-\frac{4}{12}\pi^2 q^2 a^2)$$

$$\approx 1 - \frac{1}{12}(2\pi q a)^2 \tag{4.8}$$

Expansion of eqn (4.4) to fourth order, where $\pi q a \ll 1$ gives

$$|\mathrm{sinc}(\pi q a)|^2 = 1 - \frac{1}{12}(2\pi q a)^2 + \frac{1}{90}(2\pi q a)^4 - \cdots$$

$$\approx \exp(-4\pi^2 q^2(\frac{1}{12}a^2)) \tag{4.9}$$

an identical result. Taking the initial slope on a Stejskal-Tanner plot will always yield $\overline{Z^2}/2\Delta$ in the narrow gradient pulse limit.

4.1.2   Cylinders

The normalised density function for a cylindrical sample of radius a with the gradient directed perpendicular to the longitudinal axis of the cylinder is

$$\rho(z) = \left(\frac{2}{\pi a^2}\right)(a^2 - z^2)^{1/2} \text{ for } -a \le z \le a \tag{4.10}$$

Fourier transforming this function gives $S(q)$, the signal that would be acquired by an imaging experiment on the sample[12]

$$S(q) = \int_{-a}^{a} \left(\frac{2}{\pi a^2}\right)(a^2 - z^2)^{1/2}\exp(\mathrm{i}2\pi q z)\,\mathrm{d}z$$

$$= \frac{2J_1(2\pi q a)}{2\pi q a} \tag{4.11}$$

where $J_1(x)$ is the first-order Bessel function. The echo attenuation function in the long time limit is simply the modulus squared of $S(q)$ and gives

$$E_\infty(q) = |S(q)|^2 = \frac{4(J_1(2\pi q a))^2}{(2\pi q a)^2} \tag{4.12}$$

This function has a null close to $qa \approx 0.61$ and has a less pronounced diffraction peak than the parallel plane case. Expansion of eqn (4.12) to fourth order gives

$$\frac{4(J_1(2\pi q a))^2}{(2\pi q a)^2} = 1 - \frac{1}{4}(2\pi q a)^2 + \frac{5}{192}(2\pi q a)^4 - \cdots$$

$$\approx \exp(-4\pi^2 q^2(\frac{1}{4}a^2)) \tag{4.13}$$

which implies a mean square displacement in the long time limit of $\overline{Z^2} = a^2/2$. On a Stejskal-Tanner plot the initial slope in the long time limit will yield an apparent diffusion coefficient

$$D_{\mathrm{app}} = \frac{a^2}{4\Delta} \tag{4.14}$$

4.1.3   Spheres

The normalized density function for a sphere projected along an axis (z) with radius a is given by

$$\rho(z) = \left(\frac{3}{4a^3}\right)(a^2 - z^2) \text{ for } -a \leq z \leq a \tag{4.15}$$

which upon Fourier transformation gives

$$
\begin{aligned}
S(q) &= \int_{-a}^{a} \left(\frac{3}{4a^3}\right)(z^2 - a^2)\exp(\mathrm{i}2\pi qz)\mathrm{d}z \\
&= \frac{3[\sin(2\pi qa) - (2\pi qa)\cos(2\pi qa)]}{(2\pi qa)^3}
\end{aligned}
\tag{4.16}
$$

which yields the echo attenuation function[31] by applying eqn (4.2)

$$E_\infty(q) = \frac{9[\sin(2\pi qa) - (2\pi qa)\cos(2\pi qa)]^2}{(2\pi qa)^6} \tag{4.17}$$

This expression has a null when $qa \approx 0.73$ and the "diffraction bumps" in the function are less pronounced than either the parallel plane or cylindrical case. For $q \ll a^{-1}$ expansion of eqn (4.17) gives

$$
\begin{aligned}
E_\infty(q) &= 1 - \frac{1}{5}(2\pi qa)^2 + \frac{3}{175}(2\pi qa)^4 - \cdots \\
&\approx \exp(-4\pi^2 q^2(\frac{1}{5}a^2))
\end{aligned}
\tag{4.18}
$$

for $E(q)$ in the low-q long time limit. This expression for spheres is particularly useful because of its wide relevance to colloidal systems and many biological samples. It is also particularly useful in droplet size distribution analysis. The mean square displacement for molecules in a sphere in the long time limit is $\overline{Z^2} = 2a^2/5$ implying a measure apparent diffusion coefficient of $D_{\mathrm{app}} = a^2/5\Delta$.

4.1.4   Comparison of planes, cylinders and spheres

In comparing the expressions for the three geometries given above one must note that the expression for planes is for a sample half the width of both the cylinder and sphere expressions. For a true comparison, parallel barriers separated by a distance $2a$ should be used, with the first minimum in $E(q)$ occurring at $qa = 0.5$. This gives $D_{\mathrm{app}} = a^2/3\Delta$ for the apparent diffusion coefficient at low-q revealing the simple sequence of 1/3, 1/4 and 1/5 for the factor in D_{app} for planes, cylinders and spheres respectively.

Figure 4.2 shows the long-time expressions for each of the geometries on a log-linear plot. Note the less pronounced diffraction peak for cylinders, and even more so spheres, compared to planes.

4.1.5   Reciprocal q-space

The inversion of the echo attenuation data to reveal the average propagator can have many advantages[32, 31, 38, 37]. However, the inherent loss of phase information can make the data in real space confusing unless some specific information about
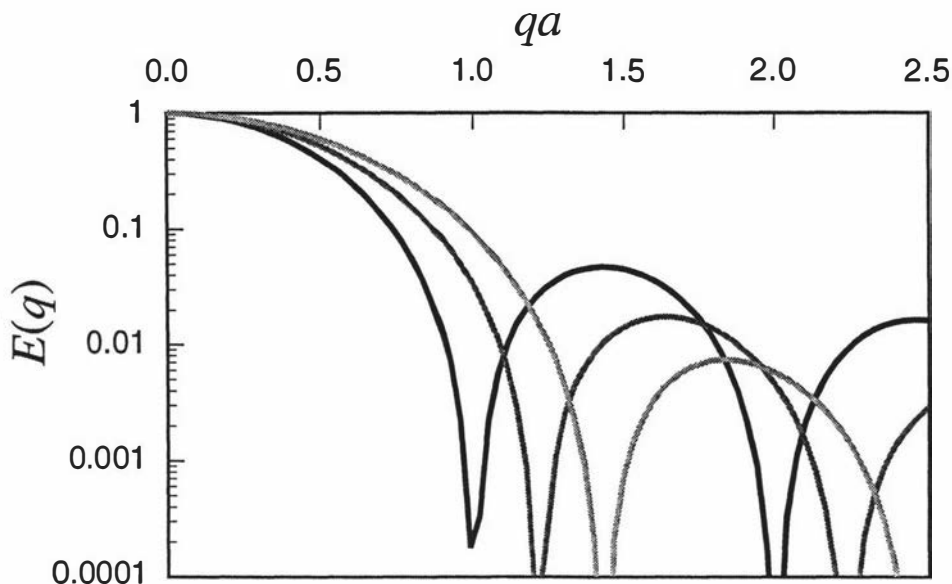
Figure 4.2: Long time limit expressions for plane(black), cylinders(grey) and spheres(light grey). The nulls occurs at $qa = 0.5$ (planes) , $qa \approx 0.61$ (cylinders) and $qa \approx 0.73$ (spheres). Note that a parallel plane spacing of $2a$ is used to be consistent with the cylinder and sphere radii of a.

the original sample is know. In most cases analysis of the echo data is best done in reciprocal space especially where an analytic expression exists for the sample geometry in question. Most of the structural information obtained in this thesis work was done so using non-linear least-squares fitting methods in a specialised PGSE program I wrote called PGSEPLOT.

In reciprocal space structures associated with boundary dimensions and boundary repetitions reveal themselves as large "bumps" and "nulls" in the data, whereas in real space the edge of the average propagator may be hard to determine precisely. In fact, working in reciprocal space ties in extensively with conventional methodologies used in other scattering type experiments. The similarities between neutron, laser and X-ray scattering and PGSE are numerous as stated before, and working in reciprocal space is a common feature of these experimental methods.

4.2   Finite time expressions for $E(q)$

When dealing with finite values of Δ the expressions for $E(q)$ are more complex. Essentially they describe the transition from free diffusion at very short diffusion times Δ, where most molecules have not encountered the restricting walls, to long Δ where the expressions described above are relevant. Fortunately, in the narrow gradient pulse situation, the propagator is analytically solvable for the three geometries described above. By solving Ficks equation, eqn (3.27), with the appropriate boundary conditions, $P_s(z|z', \Delta)$ can be found which leads to $E(q)$ through the narrow-pulse expression eqn (3.36).

4.2.1   Parallel planes

A rigorous solution is presented for $P_s(z|z', \Delta)$ and $E(q)$ in Section 6.2 where the effects of boundary relaxation are incorporated into the equations. For the case of
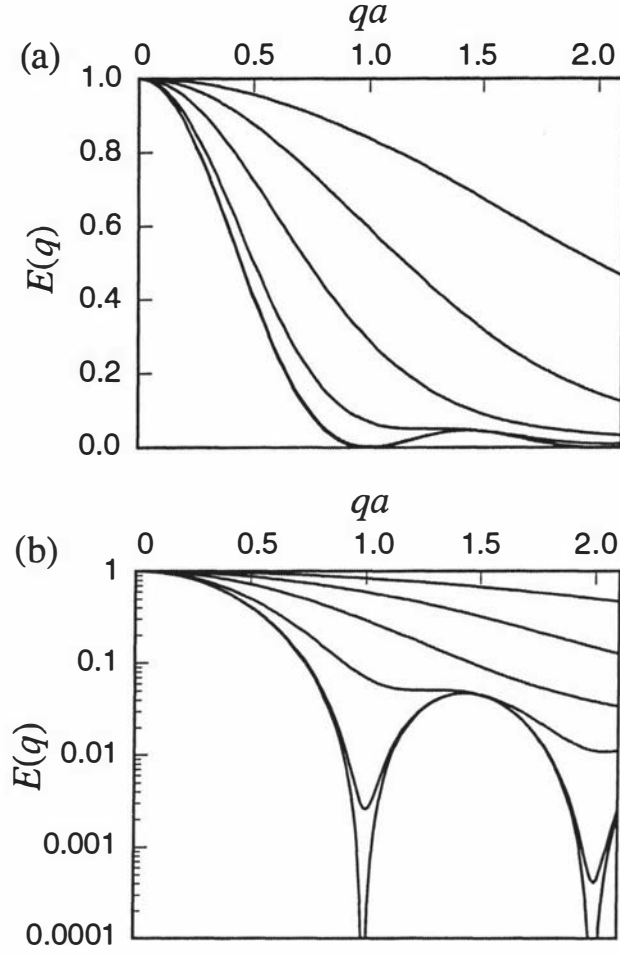
Figure 4.3: (a)Theoretical curves for the echo attenuation function $E(q)$ for molecules diffusing between plane restricting barriers of separation a assuming narrow gradient pulses. The time Δ as a fraction of $a^2/2D$ for curves of increasing attenuation is 0.01, 0.3, 0.1, 0.3, 1.0 and 10.0 respectively. The diffraction minima occur when qa has integer values and $\Delta \geq a^2/2D$. At short times the curves approach a Gaussian shape representing Brownian motion with self-diffusion coefficient D. (b) The same curves plotted on a log-linear scale.

no relaxation the solution for

$$\Psi(\mathbf{r}', t) = \int \Psi(\mathbf{r}, 0) P_s(\mathbf{r}|\mathbf{r}', t) d\mathbf{r} \tag{4.19}$$

with the reflecting boundary condition $\nabla P_s = 0$ at the walls $z = \pm a/2$, is

$$P_s(z|z', \Delta) = \frac{1}{a} + \frac{2}{a} \sum_{n=1}^{\infty} \exp\left(-\frac{n^2 \pi^2 D \Delta}{a^2}\right) \cos\left(\frac{n\pi z}{a}\right) \cos\left(\frac{n\pi z'}{a}\right) \tag{4.20}$$

an expression obtained by Tanner and Stejskal[39] through an analogy to heat diffusion. Using eqn (3.36) it can be easily shown that the echo attenuation function in the narrow-pulse limit is[39]

$$E(q) = \frac{2(1 - \cos(2\pi qa))}{(2\pi qa)^2}$$
$$+ 4(2\pi qa)^2 \sum_{k=1}^{\infty} \exp\left[-\frac{k^2 \pi^2 D \Delta}{a^2}\right] \frac{1 - (-1)^k \cos(2\pi qa)}{((2\pi qa)^2 - (k\pi)^2)^2} \tag{4.21}$$

Short time Limit

The limiting behaviour in short times can be shown to be

$$E(q) = \exp(-4\pi^2 q^2 D\Delta) \tag{4.22}$$

as expected. However eqn (4.22) applies strictly only in a lograthmic sense. Even at very short times some fraction of the molecules will be close enough to the walls to have their diffusion perturbed. This fraction will depend on the r.m.s. diffusion distance $\sqrt{2D\Delta}$ and the surface-to-volume ration, S/V, of the sample. A simple calculation might propose that a fraction $(2D\Delta)^{1/2}S/V$ would be immobilised. In fact it has been shown analytically[40, 41] that the apparent diffusion coefficient, $D_{\text{app}}(\Delta)$, observed deviates approximately from D as

$$\frac{D_{\text{app}}(\Delta)}{D} = 1 - \frac{4}{3d\sqrt{\pi}}\frac{S}{V}D^{1/2}\Delta^{1/2} + \text{higher order terms} \tag{4.23}$$

where d is the spatial dimension.

We have demonstrated this effect by evaluating eqn (4.21) for a range of times and finding $D_{\text{eff}}(\Delta)$ using the low-q limit[42]. Figure 4.4 shows graphs of such an exercise on both log and linear scales. The wall spacing a of 100 μm gives a theoretical surface-to-volume ratio of $2/a = 2.0 \times 10^{-4}$ m^{-1}. From the initial slope in Figure 4.4b , and eqn 4.23 we obtain a value for $S/V = 1.9 \times 10^{-4}$ m^{-1}, in good agreement with the expected value. Latour *et al.*[43] have found good agreement of eqn (4.23) with PGSE experiments on model porous samples.

Söderman[44] has shown that with more accurate data eqn (4.23) is exact for parallel planes, however results for cylinders and spheres show consistent errors, suggesting the numerical prefactor may be incorrect for these geometries.

Long time Limit

In the long time limit where $\Delta \gg a^2/2D$ the first term in eqn (4.21) dominates, which gives

$$E(q) = \frac{2(1 - \cos(2\pi qa))}{(2\pi qa)^2} = \frac{\sin^2(\pi qa)}{(\pi qa)^2} \tag{4.24}$$

identical to the expression found before in eqn 4.4.

4.2.2   Cylinders

The expression for $E(q)$ in cylindrical geometry in the narrow gradient pulse limit is[45, 46]

$$E(q) = 4(2\pi qa)^2 \left(\sum_{k=1}^{\infty}\sum_{m=0}^{\infty}\frac{K_m\alpha_{km}^2\left[J_m'(2\pi qa)\right]^2\exp(-D\Delta\alpha_{km}^2/a)}{(\alpha_{km}^2 - (2\pi qa)^2)^2(\alpha_{km}^2 - m^2)}\right) \tag{4.25}$$

where a is the radius of the cylinders. K_m is a constant with value 1 if $m = 0$ and 2 if $m \neq 0$. The quantity α_{km} is the roots of the Bessel equation $J_m'(\alpha) = 0$. In the long time limit this equation reduces to the expression in eqn (4.12). The behaviour at finite times is similar to the plane expression showing a transition from free Gaussian behaviour to the diffraction-like expression for restricted diffusion as Δ passes through $a^2/2D$. Söderman *et al.*[45] have also found a PGSE expression for the case of a fixed length cylinder (as in a beer can) orientated at any angle.
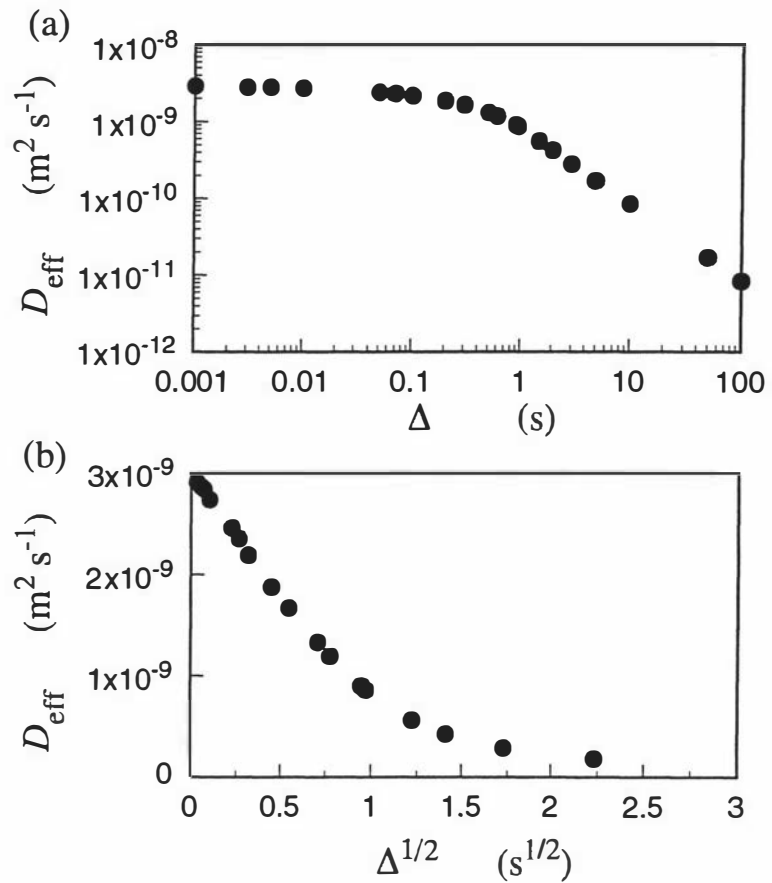
Figure 4.4: (a) D_{eff} vs Δ on a log-log scale for water diffusion between parallel plates, calculated using eqn (4.21) using low-q values. The plane separation a is 100 μm and $D = 2.5 \times 10^{-9}$ m^2 s^{-1}. The transition to restricted diffusion is apparent at $\Delta \sim a^2/2D$ a value of 2 s. (b) The same data on a linear scale plotting D_{eff} against $\Delta^{1/2}$. The linear region at short times can be used to calculate the surface-to-volume ratio through eqn (4.23).

4.2.3   Spheres

The solution for narrow-pulse approximation for spheres[47] involves the use of spherical Bessel functions.

$$
\begin{aligned}
E(q) = {} & \frac{9(2\pi qa \cos(2\pi qa) - \sin(2\pi qa))^2}{(2\pi qa)^6} \\
& - 6(2\pi qa)^2 \sum_{n=0}^{\infty} (j_n'(2\pi qa))^2 \sum_m \frac{(2n+1)\alpha_{nm}^2}{\alpha_{nm}^2 - n^2 - n} \\
& \times \exp(-\frac{\alpha_{nm}^2 D\Delta}{a^2}) \frac{1}{(\alpha_{nm}^2 - (2\pi qa)^2)^2}
\end{aligned}
\tag{4.26}
$$

where $j_n(x)$ is the spherical Bessel function of the first kind and α_{nm} is the mth root of the equation $j_n'(\alpha) = 0$. This equation reduces to the expression in eqn (4.17) in the long time limit. Only the long-time limit expression for spheres is used in this thesis but there are many systems, especially biological ones, where a spherical, rather than planer, restriction may be encountered and the full expression shown here would be essential.

4.3   The effect of finite gradient pulses

One of the limiting aspects of all these equations is the assertion that the gradient pulses are short with respect to the time taken for the molecules to diffuse between the sample barriers. This criteria has meant that very small restriction samples, which are easily accessible to PGSE in terms of q, are often difficult to use because the gradients cannot be applied over a suitably short interval. One of the key considerations has been as to whether the diffraction minima used to indicate structural features in these experiments are still apparent if finite duration gradient pulses are used. It was initially thought that intuitively the structural features would be "blurred" by the significant molecular motion over the gradient pulse interval[31].

4.3.1   Gaussian phase approximation

An accepted way to model finite gradient pulse experiments is through the Gaussian phase approximation method proposed by Neuman[48]. In calculating the echo attenuation from eqn (3.19) one assumes that the distribution of phases are Gaussian, an approximation which is strictly valid only for the case of free diffusion. However Neuman[48] derived the equations for the echo attenuation function for the case of steady gradients where spins are confined between parallel planes, in a cylinder or in a sphere. Murday and Cotts[49] derived the equation for the case of pulsed gradients for spheres and recently Balinov *et al.* [47] derived the pulsed gradient expression for planes and cylinders.

One characteristic of the Gaussian phase approximation is that no diffraction-type peaks or minima are apparent. In fact the Gaussian nature of the phase distribution necessarily implies that the echo will always decay with increasing gradient. However these equations are remarkably good at approximating the echo attenuation function and simulations show that they are normally within 5% of the simulated value for $E(q)$ at attenuations greater than 0.1[47].
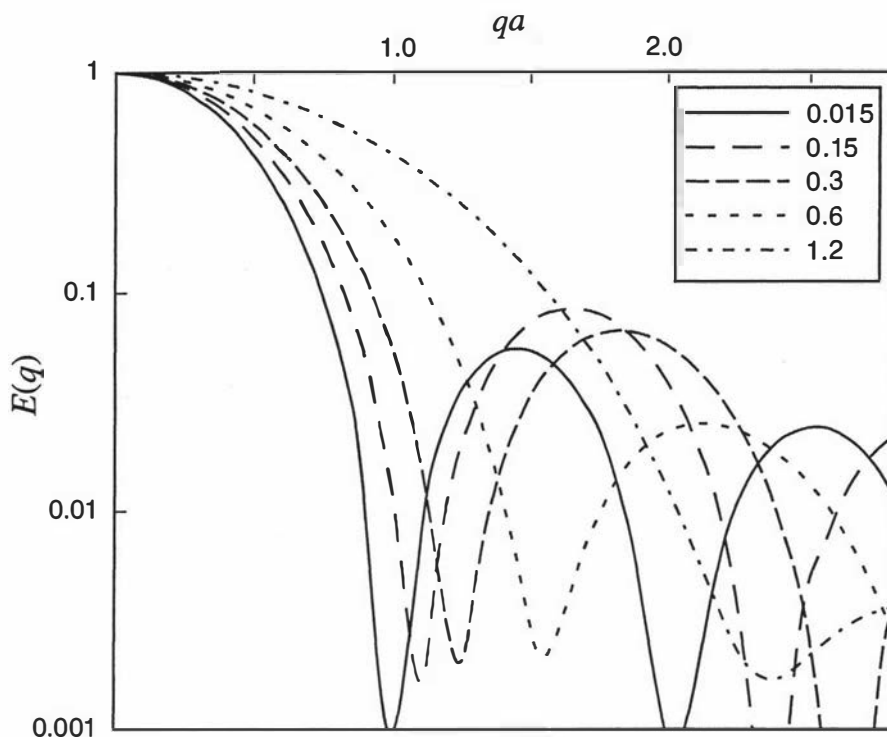
Figure 4.5: Echo attenuation, $E(q)$, for perfectly reflecting walls predicted by simulations for the case of finite gradient pulses. In each case the pulse separation, Δ, is fixed at $1.2a^2/2D$. The gradient pulse duration, δ, varies from 0.015 to 1.2 in units of $a^2/2D$. Note that even in the steady gradient case , $\delta = 1.2a^2/2D$, a diffraction minimum is apparent for $qa \sim 2.5$.

However, I have performed computer simulation experiments that show the minimum in the echo attenuation function is still very apparent even for very long gradient duration times[37]. The position of the minima are shifted to higher q, indicating that the Gaussian phase approximation is at best a crude approximation of the PGSE experiment and lacks the structural detail necessary to evaluate correctly such experiments.

4.3.2 Computer simulations

The details of the computer simulations method are outlined in Section 6.3. The simulations are for molecules diffusing between plane parallel barriers of width a with perfectly reflecting walls.

The simulation used a range of δ values where Δ is held at a fixed value and the gradient strength adjusted to keep q constant. The results for $\Delta = 1.2a^2/2D$ are shown in Figure 4.5. As δ is increased, the position of the diffraction minimum shifts above $qa = 1$. It also seems that this shift would continue to increase monotonically as δ is increased. There seems to be no fundamental limit on the size of this increase as long as Δ can be increased, and g decreased, to keep q constant.

This shift of the minimum has also been observed in simulations by Söderman and co-workers[44] , and using a different simulation technique by M.H. Blees[50]. A finite difference numerical simulation of the Bloch-Torrey equation was performed by Blees using a method proposed by Zientara and Freed[51]. In this article the author numerically solved the Bloch-Torrey equation for the magnetization evolution under the influence of diffusion, wall reflection and phase precession due to the magnetic field gradient. The echo attenuation curves shown here agree precisely with the
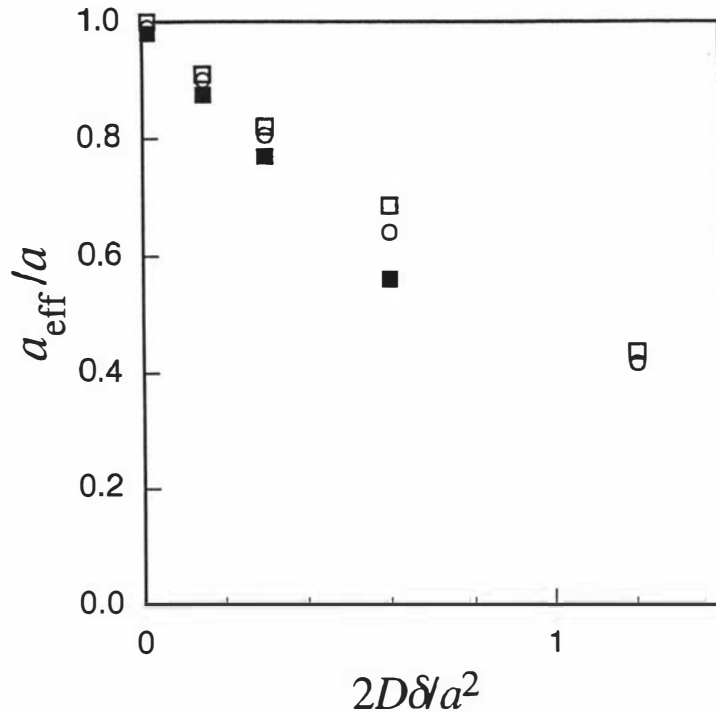
Figure 4.6: The dependance of the diffraction minimum position, a_{eff}^{-1} for perfectly reflecting walls as a function of the gradient pulse duration, δ, for three different observation times, Δ, given by 0.6 (solid squares), 1.2 (open circles), and 2.4 (open squares) in units of $a^2/2D$. The points shown are obtained from the position of the diffraction minimum derived from simulations, such as the one show from in Figure 4.5.

results of Blees.

It is remarkable that the coherences which lead to the diffraction minimum are still strongly in evidence, albeit "shifted in q-space", in the case where the gradient pulse has finite width. This contradicts the predictions of the Gaussian phase approximation which is commonly used in analytic treatments where the gradient pulse width is large. Such a treatment, which corresponds to retaining only the leading term in a cumulant expansion of the phase factor, cannot possibly lead to such q-space structure.

The influence of pulse width, over a range of experimental observation times Δ, are shown in Figure 4.6. Here the position of the minimum is shown as a function of gradient pulse width, for δ varying from $0.6a^2/2D$ to $2.4a^2/2D$.

A recent paper by Mitra and Halperin[52] explains this shifting of the minimum by using a center-of-mass (COM) propagator in place of the normal propagator function. In their "ansatz" the molecule acquires a phase shift equivalent to its COM position over the duration of the gradient pulse. For two finite gradient pulses this has the effect of reducing the effective displacement and hence reducing the phase shift acquired by the molecules. The effect is that the pore distances appear smaller and the q-space minimum is shifted to higher q. They also predict that in the very long time limit case, many times $a^2/2D$, the COM propagator will be shifted closer to the center of the pore and appear more Gaussian-like, slowly reducing the diffraction-like effect.

4.3.3 Harmonic potential

There is in fact one restricted diffusion problem for which a complete analytic solution is known for any gradient pulse duration or separation. Terentjev *et al.*[53] have recently found the echo attenuation function for a particle confined by a harmonic potential. Because the problem remains Gaussian it can be solved completely, the only case known to date for which this can be done. The solution may have particular relevance to the problem of measuring restricted diffusion in polymers where the confining tube can be modelled by such a harmonic well.

CHAPTER 4.   PGSE AND RESTRICTED DIFFUSION

Chapter 5

PGSE-MASSEY

In Pulsed Gradient Spin Echo experiments, there is no fundamental limitation on the size of the dynamic displacements one can measure. However, in real PGSE experiments, one finds it increasingly difficult to accurately measure displacements of less than 100 nm. This in turn leads to a lowest measurable self-diffusion coefficient of around 10^{-14} m^2 s^{-1}. The main problem is that the two gradient pulses have to be matched to an exceedingly high accuracy. One of the primary considerations in gradient switching units is the ability to correctly deliver the same amount of charge to the gradient coils during each pulse. It is also important that the sample does not move, in the time between the two gradient pulses, as additional artifacts can be introduced.

One method proposed to overcome these limitations is to use the large, stable field gradients found in the fringe field of superconducting magnets[25, 26]. Alternatively one can use a standard PGSE sequence and correct for the artifacts generated by gradient pulse mismatch and sample movement using a method dubbed PGSE-MASSEY[54] by its creator. The acronym stands for *modulus addition using spatially separated echo spectroscopy*. As part of the work in this thesis, I implemented the PGSE-MASSEY on our spectrometer as outlined below. This technique was used to acquire the data for the polymer structure functions in Section 8.4.3.

5.1 Theory

5.1.1 The cause of Echo instabilities

The effect of sample movement between the two gradient pulses would be to introduce a common displacement to all the spins. This results in a net phase shift for all spins at the echo. Gradient mismatch would result in a local phase shift dependent on the position of the spin within the sample. Both these effects are complicated by the fact that they may, and usually will, differ from one individual acquisition to the next due to irregular movement of the sample in the first case, or noise or current ripple in the second. The average propagator, eqn (3.39), can be modified to

$$E(\mathbf{q}) = \int \rho(\mathbf{r}) \int \overline{P_s}(\mathbf{R}, \Delta) \exp[\mathrm{i}2\pi\mathbf{q} \cdot \mathbf{R} + \mathrm{i}\Phi]\mathrm{d}\mathbf{R}\mathrm{d}\mathbf{r} \tag{5.1}$$

where the phase shift Φ accounts for the sample movement or gradient mismatch. If the sample moves by $\Delta\mathbf{r}$ between the gradient pulses and the pulses themselves

have a mismatch of strength $\Delta \mathbf{q}$ then

$$2\pi \mathbf{q} \cdot \mathbf{R} + \Phi = 2\pi[(\mathbf{q} + \Delta \mathbf{q}) \cdot (\mathbf{r} + \mathbf{R} + \Delta \mathbf{r}) - \mathbf{q} \cdot \mathbf{r}] \tag{5.2}$$

If we define the z-axis so that the static and dynamic displacements are z and Z respectively and insist that the direction of the two gradient pulses are the same then one can write

$$\begin{align}
2\pi \mathbf{q} \cdot \mathbf{R} + \Phi &= 2\pi[(q + \Delta q)(z + Z + \Delta z) - qz] \tag{5.3} \\
&= 2\pi[qZ + (q + \Delta q)\Delta z + \Delta qz] \tag{5.4}
\end{align}$$

Notice the term ΔqZ is removed since qZ is only on the order of unity and $\Delta q \ll q$. Eqn (5.1) can now be written using eqn (5.4) as

$$\begin{align}
E(q) &= \left\{ \int \overline{P_s}(Z, \Delta) \exp[\text{i}2\pi qZ] \mathrm{d}Z \right\} \exp[\text{i}2\pi(q + \Delta q)\Delta z] \\
&\quad \times \left\{ \int \rho(z) \exp[\text{i}2\pi \Delta qz] \mathrm{d}z \right\} \tag{5.5}
\end{align}$$

The first bracketed term in eqn (5.5) is the normal echo attenuation function expected from the PGSE experiment free from artifacts. This term can be called $E_0(q)$. The second term is the phase shift resulting from the Δz movement of the sample. The third term in brackets is the integral of the position-dependent phase shifts. This final term is only correctable if the position dependence of the phase shifts can be removed. This is readily achieved by using a read gradient.

5.1.2 Effect of a read gradient

By applying a k-space read gradient, G, with the same gradient coil that generated the PGSE gradient g it is possible to resolve the phase shifts. The pulse sequence used to implement this is shown in Figure 5.1. The spatial separation of the pixels is $2\pi/\gamma GNT$ where N is the number of points acquired at a sampling interval T. This spatial resolution must be less than the "wavelength" of the phase oscillation in the sample. We therefore require

$$\frac{2\pi}{\gamma GNT} \le \frac{1}{\Delta q} \tag{5.6}$$

which implies that

$$G \ge \frac{2\pi \Delta q}{\gamma NT} \ge \frac{\delta \Delta g}{NT} \tag{5.7}$$

The final term in eqn (5.7) assumes the mismatch in q is due to a variation in g and not δ. Since δ and NT will both be of the order of milliseconds this implies that G will have to be comparable to the gradient fluctuation Δg.

A coherent superposition will now occur at the time $t = -2\pi \Delta q/\gamma G$, either before or after the echo depending upon the sign of the mismatch. Full echo acquisition is therefore essential if this scheme is going to work. Long acquisition times will reduce the bandwidth and improve signal-to-noise if bandpass filtering is used. However the pixel separation must be greater then the homogeneous linewidth setting a lower limit on the bandwidth of

$$\frac{1}{T} \ge \frac{N}{\pi T_2} \tag{5.8}$$
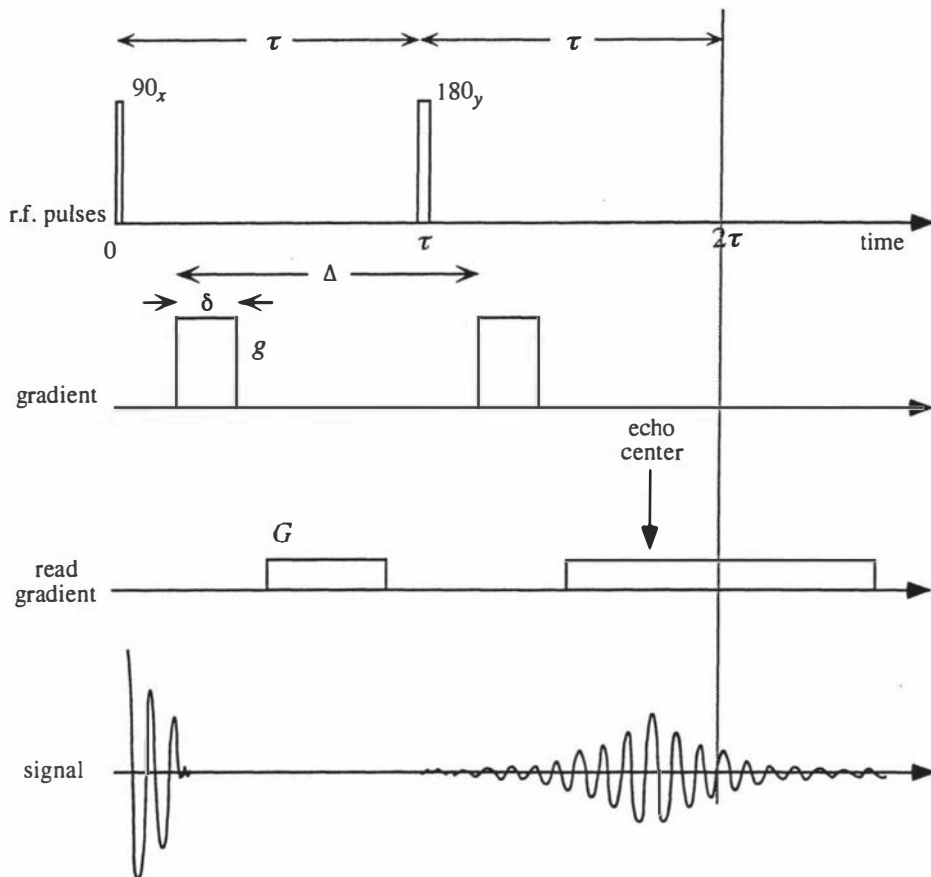
Figure 5.1: The PGSE-MASSEY pulse sequence. Both the read gradient and the PGSE gradient are applied to the same gradient coil but the current is supplied from different sources. Notice the exaggerated displacement of the echo center from 2τ to indicate the effect of a mismatch in the two PGSE gradient pulses. For this reason full echo acquisition must be used as the echo center can vary significantly from one acquisition to the next.

With the full echo acquisition, the Fourier transform of the time domain data will contain no dispersion term. For a read gradient k and a PGSE gradient q the echo is[54]

$$E(q, k) = E_0(q) \exp[\mathrm{i}2\pi(q + \Delta q)\Delta z] \int_{-\infty}^{\infty} \rho(z) \exp[\mathrm{i}2\pi\Delta qz] \exp[\mathrm{i}2\pi kz]\mathrm{d}z \quad (5.9)$$

which upon Fourier transformation with respect to k yields

$$E(q, z) = E_0(q) \left\{ \exp[\mathrm{i}2\pi(q + \Delta q)\Delta z] \right\} \rho(z) \left\{ \exp[\mathrm{i}2\pi\Delta qz] \right\} \quad (5.10)$$

This one-dimensional projection image $\rho(z)$ weighted by the *true* echo attenuation function $E_0(q)$ has two additional terms in the expression; a zeroth order phase shift $\{\exp[\mathrm{i}2\pi(q + \Delta q)\Delta z]\}$ due to sample movement, and a first order phase shift $\{\exp[\mathrm{i}2\pi\Delta qz]\}$ due to pulse mismatch.

Analysis of the data must be performed on an individual acquisition basis as Δz and Δq may and probably will fluctuate from one FID to the next. Once the phase shifts are resolved, individual spectra can be co-added and upon integration of the projection image a value for $E_0(q)$ can be determined. The experiment can then be repeated for different values of q.

Two procedures are possible for removing the phase artifacts. If the signal-to-noise ratios are good then the spectra could be autophased for maximum integrated area. For the majority of cases, where signal-to-noise will be poor, a modulus calculation can be performed to remove phase twists on the spectrum. However, a modulus calculation leads to a finite noise baseline and forbids the use of phase cycling to remove coherent noise.

It is important to consider the noise power baseline in such experiments. To illustrate the process we consider n acquisitions, labelled by i of m pixels in a spectrum, labelled by j where the signal per pixel is a_j and the noise per pixel is σ_{ij} where σ is the r.m.s. noise power per pixel. By squaring the signal we find the power for pixel j is

$$\mathrm{Power}(j) = \sum_{i=1}^{n}(a_j + \sigma_{ij})^2 = na_j^2 + n\sigma^2 + 2a_j \sum_{i=1}^{n} \sigma_{ij} \quad (5.11)$$

The second term is the noise baseline, common to all points which can be subtracted from the final spectrum. The summation in the last term can be replaced with $n^{1/2}\sigma_j$ to give after baseline subtraction

$$\mathrm{Power}(j) = na_j^2(1 + \frac{2\sigma_j}{n^{1/2}a_j}) \quad (5.12)$$

Therefore the square root of the net power is $n^{1/2}a_j + \sigma_j$ and the integral over the m points of the spectrum gives

$$\mathrm{Signal} = n^{\frac{1}{2}} \sum_{j=1}^{m} a_j + \sum_{j=1}^{m} \sigma_j = n^{\frac{1}{2}}A + \sum_{j=1}^{m} \sigma_j \quad (5.13)$$

The noise sum is a random variable centered about zero with standard deviation $m^{1/2}\sigma$. Hence the overall signal-to-noise ratio is $n^{1/2}A/m^{1/2}\sigma$.
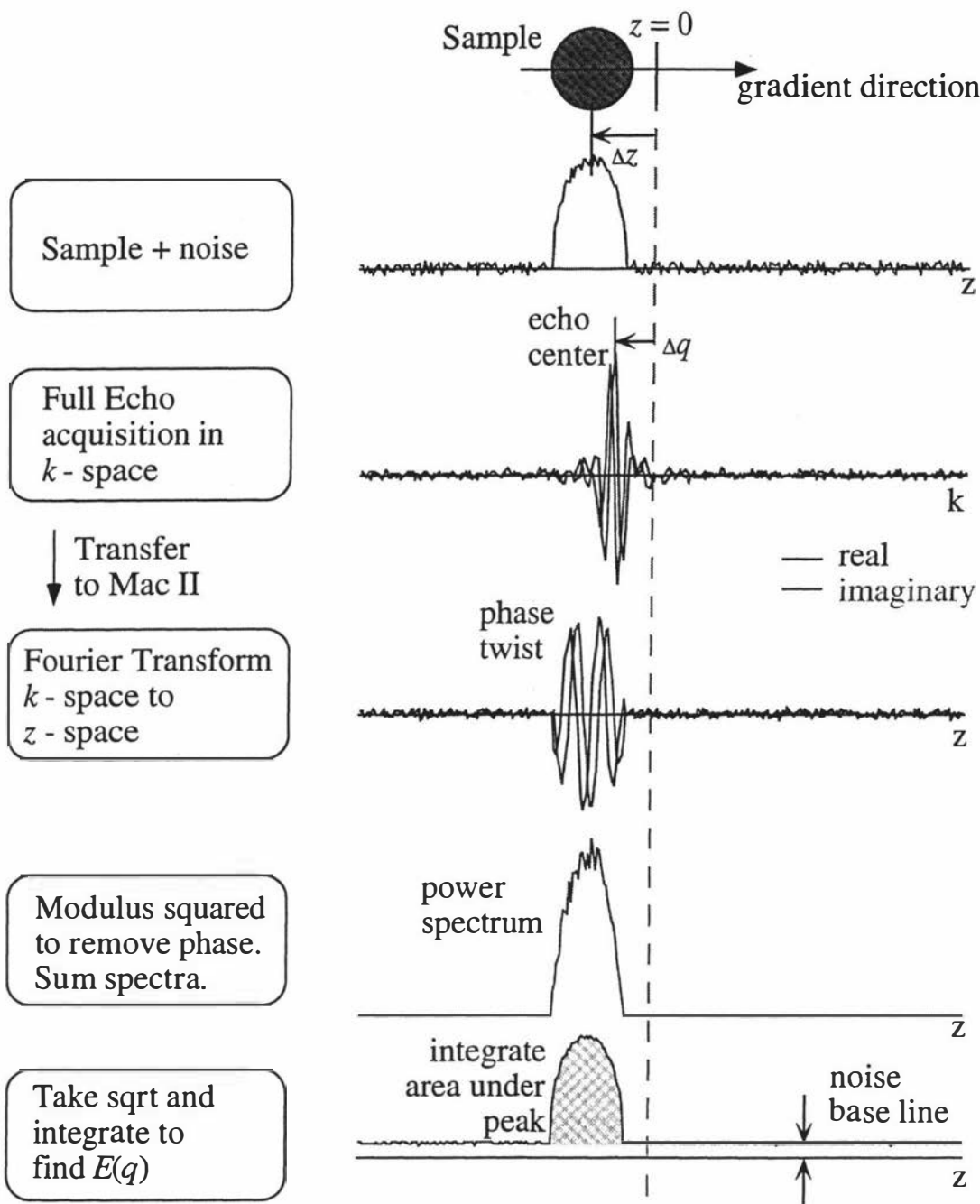
Figure 5.2: Diagram showing the various steps involved in PGSE-MASSEY analysis. For the cylindrical sample shown a hypothetical position shift Δz and gradient mismatch Δq are included. Fourier transformation of the echo yields a normal projection image of the sample but with an arbitrary phase shift and phase twist due to Δz and Δq respectively. The modulus addition removes these artifacts but leaves a noise baseline which must be removed before final integration of the peak.
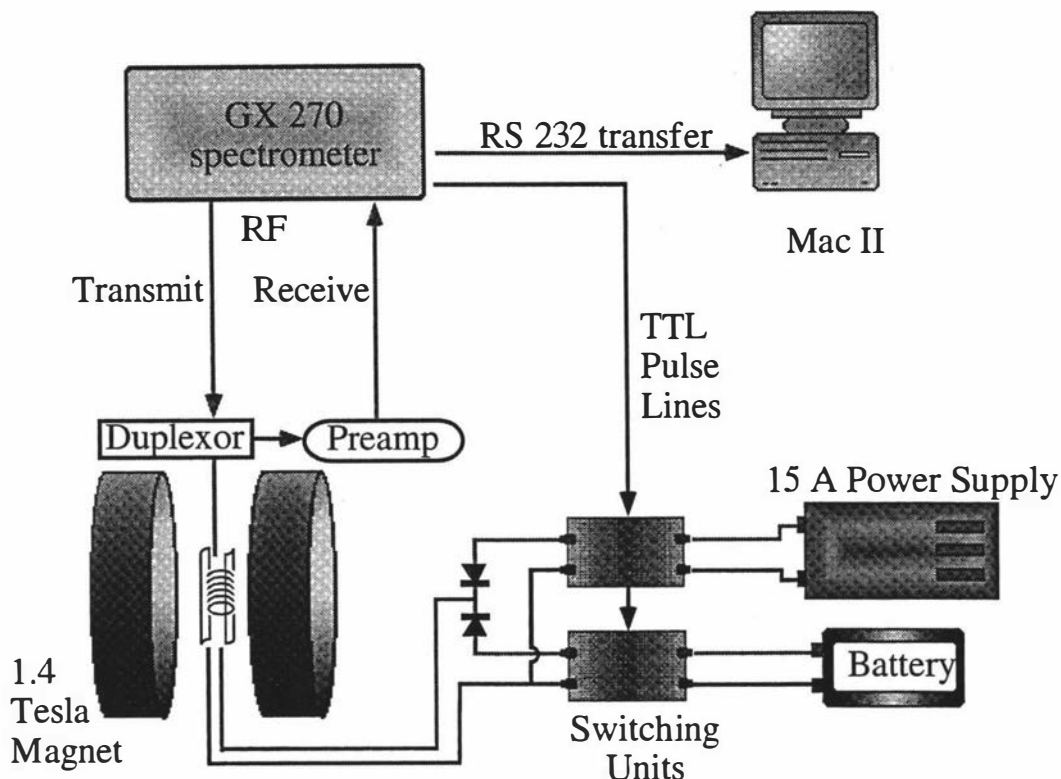
Figure 5.3: Diagram of hardware setup used to implement PGSE-MASSEY. The GX-270 spectrometer is used as it has simultaneous quadrature acquisition. The two power supplies are switched by standard TTL controlled current switching boxes. A battery is used to supply current for the small read gradient. Data is transferred via an RS-232 serial port and analysis of the data is performed on a program written on a Macintosh computer.

5.2   Hardware and Software

Some modifications are necessary in order to implement this technique. The read gradient is typically several orders of magnitude smaller than the PGSE gradient and hence requires a separate power supply. Also the need for full quadrature acquisition, and not the time share quadrature on the FX-60, meant it was necessary to use the GX-270 spectrometer for signal acquisition.

5.2.1   Combining gradients

When connecting two power supplies to the same coil, care must be taken not to directly connect the supply terminals to each other. A pair of crossed, high power diodes provided the necessary isolation between each supply. A further problem is that of earth loops, especially if the ground wires are made common. In fact the best supply for the read gradient I found was a rechargeable battery and a variable resistor, which removed the possibility of getting extensive hum in the gradient circuit due to earthing problems, and gave excellent control of the small currents necessary for the read gradient.

5.2.2   Signal acquisition

The GX-270 spectrometer was used for the PGSE-MASSEY experiments as, at the time, it was the only spectrometer with full complex echo acquisition. TTL outputs were required for switching both gradients and for turning on the current of the PGSE gradient at the required time. The magnet used however was the 60MHz electromagnet and the usual PGSE probe. Only the external lock was used on the FX-60 spectrometer. The r.f. pulses were fed out of the power amp on the GX-270 and into the crossed diodes of the 60MHz quarter wavelength trap. The homebuilt preamp was used before the signal was returned to the A-D converters on the GX-270. Although the cables to connect the spectrometers were long compared with typical lengths I found the reduction in signal-to-noise was not excessive.

Because all processing of the signal had to occur after the acquisition, the data was collected in a 2-D file with one single FID per row. Typically between 32 to 128 acquisitions, and therefore rows, were used for one single q-space point. The experiment was then repeated for additional q points.

5.2.3   Software

Once acquired the data was transferred via serial port to a Macintosh computer where the FT, baseline subtraction and modulus addition were performed by a program written by this author. The program then integrated the spectrum between predefined points and displayed the result. Once all q-space points were acquired, the echo attenuation data was saved in a file in a format suitable for use by the PGSEPLOT analysis program.

Chapter 6

PGSE experiments on parallel barrier samples

6.1   Introduction

Until recently[37] the PGSE diffraction-like effects, discussed in Chapter 4, had not been investigated or observed experimentally. As pointed out in ref [31], the use of eqn (4.21) had been through varying Δ, the observation time, and not q. None of the diffraction-like effects discussed had been observed in experiments before the work done in this thesis[38]. To examine this fundamental problem of the "single slit", or parallel barrier, we performed PGSE experiments[37] on rectangular microslides with an internal gap of 100 μm, which showed the expected diffraction effects[32, 37, 31]. Initial fitting of the theory to the experimental data was good, but showed some consistent errors which suggested that there may be relaxation of spins occurring at the walls of the microslides. We have extended the theory for parallel planes, given in Section 4.2.1 to include the effects of relaxation at the walls and find a new closed form expression[37, 46]. This theory was also recently derived by Snaar and Van As[55], but although mathematically equivalent, their expression is not as simple as the one summarised here. I performed computer simulations to examine the effects of wall relaxation and to compare with the analytic theory. These simulations have provided an important test of some of the assumptions implicit in the theory.

6.2   Theory of enclosing boundaries with edge relaxation

We show here how the theory presented in Section 4.2.1 can be expanded to include the effects of relaxation at the barrier walls.

Full solutions for $\rho(\mathbf{r}', t)$ and $P_s(\mathbf{r}|\mathbf{r}', t)$ are possible for the three fundamental geometries[46] under the narrow gradient pulse condition along with corresponding expressions for $E(q)$. These solutions involve expanding ρ or P_s on some orthogonal basis set appropriate to the geometry. The solution for containers of arbitrary shape would best be obtained using a numerical approach on a computer.

To evaluate the time and space evolution of $\rho(\mathbf{r}, t)$ we need to evaluate the partial differential equation

$$D\nabla^2 \rho(\mathbf{r}, t) = \frac{\partial \rho(\mathbf{r}, t)}{\partial t} \tag{6.1}$$

which can be solved using a "separation of variables" technique where $\rho(\mathbf{r}, t) = u(\mathbf{r})v(t)$. Substituting into eqn (6.1) and rearranging one gets

$$\frac{D\nabla^2 u(\mathbf{r})}{u(\mathbf{r})} = \frac{\partial v(t)}{\partial t}\frac{1}{v(t)} \tag{6.2}$$

Since both sides must be constant, we can set them equal to $-k^2$, given that the exponential form for $v(t)$ must have a negative coefficient to satisfy the limit $t \to \infty$. This leads to the Helmholtz equations

$$\nabla^2 u(\mathbf{r}) + k^2 u(\mathbf{r}) = 0 \tag{6.3}$$

$$\frac{\partial v(t)}{\partial t} + Dk^2 v(t) = 0 \tag{6.4}$$

with solutions for $v(t)$ of the form

$$v_n(t) = A_n \exp(-Dk_n^2 t) \tag{6.5}$$

and for $u(\mathbf{r})$ of the form

$$\nabla^2 u_n(\mathbf{r}) = -k_n^2 u_n(\mathbf{r}) \tag{6.6}$$

This leads to a general solution for $\rho(\mathbf{r}, t)$ of the form

$$\rho(\mathbf{r}, t) = \sum_n A_n u_n(\mathbf{r})\exp(-Dk_n^2 t) \tag{6.7}$$

where A_n will be determined by the initial conditions and k_n will be determined by the boundary conditions. The differential equation governing $P_s(\mathbf{r}|\mathbf{r}', t)$ is the same diffusion equation, namely,

$$D\nabla'^2 P_s = \frac{\partial P_s}{\partial t} \tag{6.8}$$

where D is the self-diffusion coefficient again. P_s must satisfy the different initial condition

$$P_s(\mathbf{r}|\mathbf{r}', 0) = \delta(\mathbf{r} - \mathbf{r}') \tag{6.9}$$

An eigenfunction expansion of P_s can also be made because

$$\delta(\mathbf{r} - \mathbf{r}') = \sum_{n=0}^{\infty} u_n(\mathbf{r})u_n(\mathbf{r}') \tag{6.10}$$

where u_n are the orthonormal set of solutions to the Helmholtz equation. This leads to the eigenfunction expansion

$$P_s(\mathbf{r}|\mathbf{r}', t) = \sum_{n=0}^{\infty} \exp(-Dk_n^2 t)u_n(\mathbf{r})u_n(\mathbf{r}') \tag{6.11}$$

where λ_n are the eigenvalues of $u_n(\mathbf{r})$. In order to be finite as $t \to \infty$ we make $\lambda_n = -k_n^2$. P_s can then be found, using eqn (6.11), by setting the appropriate boundary conditions and finding the eigenfunctions.

6.2.1 Boundary conditions

It is possible for the boundaries to provide some mechanism for extra relaxation of the spins when they strike the surface[56, 57]. Any pause in the rotation of the molecule as it hits the surface could be a mechanism for such relaxation. Field gradients, caused by susceptibility changes, may also be responsible. This relaxation leads to a loss of signal from the spins *as if* the molecules themselves had been removed from the sample. This will lead to a reduction in the spin density $\rho(\mathbf{r}, t)$ over time. Consider a volume element of thickness δx against a boundary surface of area δA. If the spins decay exponentially as $\exp(-t/T)$, with a local relaxation time T within this element, then the rate of loss of spins at the surface will be

$$
\begin{aligned}
\text{loss rate} \quad &= \quad \frac{\delta x\, \delta A\, \rho}{T} \\
&= \quad M\, \delta A\, \rho
\end{aligned}
\tag{6.12}
$$

where M is the "surface magnetization sink density". This loss will be fed by a flux, $\mathbf{J}$, that is driven by any spatial variation in spin density such that

$$
\mathbf{J} = \hat{\mathbf{n}} \cdot (-D\nabla\rho).
\tag{6.13}
$$

and the "gain" rate of spins into the volume element will be

$$
\text{gain rate} = \mathbf{J}\, \delta A = \hat{\mathbf{n}} \cdot (-D\nabla\rho)\, \delta A
\tag{6.14}
$$

Equating eqn (6.12) and eqn (6.14) leads to the Brownstein-Tarr condition

$$
D\hat{\mathbf{n}} \cdot \nabla\rho + M\rho = 0
\tag{6.15}
$$

For the case of perfectly reflecting walls where $M = 0$ it is obvious that the density will remain constant across the sample and therefore $\hat{\mathbf{n}} \cdot \nabla\rho = 0$. For perfectly absorbing walls where $M \to \infty$ we find $\rho = 0$ at the walls. From the relationship between P_s and ρ we find that P_s is governed by the same boundary condition

$$
D\hat{\mathbf{n}} \cdot \nabla P_s + M P_s = 0
\tag{6.16}
$$

with identical limiting cases.

6.2.2 Parallel plane pore

This is a one dimensional problem in which the gradient is applied along the z-direction normal to two parallel boundaries. The walls are placed at $z = \pm a/2$ and are allowed to be partially absorbing. The resulting general expression can be simplified to the limiting cases discussed previously.

The eigenmode expansion

To solve eqn (6.10) we use as our orthonormal basis set the function

$$
u_n(z) = A_n \cos(k_n z) + B_n \sin(k_n z)
\tag{6.17}
$$

which when put into the boundary conditions given by eqn (6.15) at the points $z = a/2$ and $z = -a/2$ yields the two possible solutions

$$
k_n \tan\left(\frac{k_n a}{2}\right) = \frac{M}{D} \quad \text{and} \quad B_n = 0
\tag{6.18}
$$

or

$$
k_n \cot\left(\frac{k_n a}{2}\right) = -\frac{M}{D} \quad \text{and} \quad A_n = 0
\tag{6.19}
$$

The pore density function

An expression for the pore density function can now be obtained using eqn (6.7) and eqn (6.18). We make a switch to the dimensionless variable $\xi_n = k_n a/2$ for convenience. Only the cosine basis function is needed to fully describe $\rho(z,t)$ and with appropriate normalisation we get the following expression for the density function across the sample

$$\rho(z,t) = \exp\left[-\frac{(2\xi_n)^2 Dt}{a^2}\right] \frac{2}{a[1 + \sin(2\xi_n)/2\xi_n]} \frac{sin(\xi_n)}{\xi_n} \cos(2\xi_n z/a) \qquad (6.20)$$

where the ξ_n are the roots of the modified eqn (6.18) namely

$$\xi_n \tan(\xi_n) = \frac{Ma}{2D} \qquad (6.21)$$

By integrating eqn (6.20) over the whole sample one can obtain the signal relaxation function

$$S(t) = \exp\left[-\frac{(2\xi_n)^2 Dt}{a^2}\right] \frac{4\sin^2(\xi_n)}{2\xi_n[\xi_n + \sin(2\xi_n)]} \qquad (6.22)$$

which is identical to the expression found by Brownstein and Tarr[57] to describe the net relaxation in a container due to relaxation at the walls. This expression is used as an initial check in computer simulations as it predicts the echo attenuation for the $q = 0$ point, the fraction of spins unrelaxed after a time Δ.

The propagator

The propagator can also be evaluated from the basis functions using eqn (6.11). However both cosine and sine like solutions will be in the expression. Again we make a switch to the dimensionless variables $\xi_n = k_n a/2$ and $\zeta_m = k_m a/2$ and making the PGSE substitution of Δ for t we get

$$\begin{aligned}
P_s(z|z',\Delta) = &\sum_{n=0}^{\infty} \exp[-\frac{(2\xi_n)^2 D\Delta}{a^2}]2[1 + \sin(2\xi_n)/2\xi_n]^{-1} \\
&\times \cos(2\xi_n z/a)\cos(2\xi_n z'/a) \\
+ &\sum_{m=0}^{\infty} \exp[-\frac{(2\zeta_m)^2 D\Delta}{a^2}]2[1 - \sin(2\zeta_m)/2\zeta_m]^{-1} \\
&\times \sin(2\zeta_m z/a)\sin(2\zeta_m z'/a)
\end{aligned} \qquad (6.23)$$

where ξ_n and ζ_m are roots of the transcendental equations

$$\xi_n \tan(\xi_n) = \frac{Ma}{2D} \qquad (6.24)$$

$$\zeta_m \cot(\zeta_m) = -\frac{Ma}{2D} \qquad (6.25)$$

For perfectly reflecting walls ($M = 0$), the roots of these transcendental equations are $\xi_n = 0, \pi, 2\pi, \ldots$ and $\zeta_m = \pi/2, 3\pi/2, \ldots$. Substitution of these values into eqn (6.23) gives an identical expression to the one shown in eqn (4.20).

The average propagator $\overline{P_s}(Z, \Delta)$ can be evaluated, neglecting relaxation before and after the two gradient pulses, by using a^{-1} for $\rho(z,0)$. Substituting eqn (6.23) into eqn (3.30) yields[37]

$$
\begin{aligned}
\overline{P_s}(Z, \Delta) = & \sum_{n=1}^{\infty} \exp[-\frac{4{\xi_n}^2 D\Delta}{a^2}]a^{-2}[1 + \sin(2\xi_n)/2\xi_n]^{-1} \\
& \times(\{a - Z + (a/4\xi_n)[\sin(2\xi_n - 4\xi_n Z/a) + \sin(2\xi_n)]\}\cos(2\xi_n Z/a) \\
& \quad + (a/4\xi_n)[\cos(2\xi_n - 4\xi_n Z/a) - cos(2\xi_n)]\sin(\xi_n Z/a)) \\
& + \sum_{m=1}^{\infty} \exp[-\frac{4{\zeta_m}^2 D\Delta}{a^2}]a^{-2}[1 - \sin(2\zeta_m)/2\zeta_m]^{-1} \\
& \times(\{a - Z - (a/4\zeta_m)[\sin(2\zeta_m - 4\zeta_m Z/a) + \sin(2\zeta_m)]\}\cos(2\zeta_m Z/a) \\
& \quad - (a/4\zeta_m)[\cos(2\zeta_m - 4\zeta_m Z/a) - cos(2\zeta_m)]\sin(\zeta_m Z/a))
\end{aligned}
\tag{6.26}
$$

for the average propagator.

Echo attenuation function

The echo attenuation function can be evaluated using eqn (3.36) and gives[37, 46]

$$
\begin{aligned}
E(q, \Delta) = & \sum_{n=0}^{\infty} \exp[-\frac{(2\xi_n)^2 D\Delta}{a^2}]2[1 + \sin(2\xi_n)/2\xi_n]^{-1} \\
& \times \frac{[(\pi qa)\sin(\pi qa)\cos\xi_n - \xi_n \cos(\pi qa)sin\xi_n]^2}{[(\pi qa)^2 - \xi_n^2]^2} \\
& + \sum_{m=0}^{\infty} \exp[-\frac{(2\zeta_m)^2 D\Delta}{a^2}]2[1 - \sin(2\zeta_m)/2\zeta_m]^{-1} \\
& \times \frac{[(\pi qa)\cos(\pi qa)\sin\zeta_m - \zeta_m \sin(\pi qa)cos\zeta_m]^2}{[(\pi qa)^2 - \zeta_m^2]^2}
\end{aligned}
\tag{6.27}
$$

A simple check is done by evaluating it for the two limiting cases in M. For perfectly reflecting walls $M = 0$, this expression simplifies to the expression already given in eqn (4.21). For the perfectly absorbing walls ($M \to \infty$), the expression reduces to

$$
E(q) = \sum_{k=1}^{\infty} \exp\left[-\frac{k^2\pi^2 D\Delta}{a^2}\right] 4(k\pi)^2 \frac{1 - (-1)^k \cos(2\pi qa)}{((2\pi qa)^2 - (k\pi)^2)^2}
\tag{6.28}
$$

an expression originally derived by Frey *et al.*[58].

Long time limit

It is interesting to note at this stage that a long time limit expression can be found for the completely absorbing barrier case. Normalising eqn (6.28)to the $q = 0$ point in the long time limit we get

$$
E_\infty(q) = \frac{\pi^4 \cos(\pi qa)}{((2\pi qa)^2 - \pi^2)^2}
\tag{6.29}
$$

This expression still has a diffraction minimum as for reflecting edge walls. However, the null for this expression occurs at $qa = 1.5$, shifted from $qa = 1.0$ case for reflecting barriers. This indicates that the propagator appears to represent a smaller container, a situation not unreasonable if all spins near the walls are being completely relaxed.

While it is unlikely that eqn (6.29) could ever be used in a real experiment due to the overwhelming relaxation effects, it indicates that the echo function is significantly altered by the effects of relaxation[55, 37].

The full nature of the echo attenuation function given by eqn (6.29) will be discussed in conjunction with the computer simulation results in the following chapter. Analytic solutions for cylindrical and spherical geometry have also been found[46] along with extensions to eqn (6.29) to allow for the effect of relaxation before and after the gradient pulses[46].

6.3 Computer simulations

Several programs, written in C, were used to simulate the dynamics of molecules trapped between partially reflecting walls. The programs were compiled and executed on a SUN IPX workstation. This SPARC chip based computer is capable of, on average, 4.2 MFlops (million floating point operations per second) and 28 Mips (million integer operations per second). The UNIX multitasking setup also meant it was ideal for setting up multiple simulations over an extended period. Random Number generators from Numerical Methods in C[59] were tested and used. These random number generators did not suffer from pitfalls common to the simple, built-in random number generators supplied with most compilers.

6.3.1 Hopping method

Initially both the time and spatial dimensions were quantized. The advantages of such a constant are numerous. Integer based arithmetic can be used for all functions and as such is often much faster than floating point based programs. A simple left-or-right (1 or 0) random number generator can be used, this procedure was on average 7 times faster than the uniform distribution generator used later. Also a predefined lookup table could be used to calculate the accumulated phase shifts of the spins as only a fixed range of displacements were allowable.

Relaxation at the walls can be added by allowing a finite probability for the molecule to be removed if it lands in the lattice site next to a wall. This models the Brownstein-Tarr assumption that a relaxation layer of δx extends from a wall of relaxation sink density M.

However the disadvantage of the finite lattice or hopping method is the discrete nature of the molecular motion. I used a lattice of 100 sites between each barrier and a 0.1 ms time grid but found results converged slowly to a consistent value, especially for checks of simple free diffusion where a Gaussian distribution of displacements is expected. In Figure 6.1 a molecular density distribution $\rho(z,t)$ is shown in order to demonstrate this point. Notice that the theory lines of eqn (6.20) are above the simulation data towards the center of the sample. This strongly suggests that the random diffusion mechanism of the simulation does not accurately represent the Gaussian like motion of proper diffusion. A finer time or spatial grid would have corrected these errors but would have meant unreasonably long simulation times. This method was therefore rejected in favour of the following technique.

Figure 6.1: Nuclear spin magnetization densities $\rho(z, t)$ predicted by the *hopping* simulation technique and the theory of eqn (6.20), for partially absorbing walls with $Ma/2D = 20$. Note that for $t = 0$, the theoretical prediction is a constant, $1/a$. Six successive time intervals are displayed. In multiples of $a^2/2d$, t is, respectively, 0.0 (solid dots), 0.005 (solid triangles), 0.025 (open circles), 0.05 (solid circles), 0.25 (open squares), 0.5 (solid squares). Note the discrepancy between theory and simulation near the center of the sample.

6.3.2 Gaussian method

In order to remove the discrete nature of the spatial jump distance a Gaussian jump algorithm was developed. The program was rendered entirely in floating point arithmetic. All positions between $-a/2$ and $+a/2$ were available to the molecules. It was found that larger time steps could be used with no compromise in the accuracy of the simulation. Two types of simulations were performed. In the first type, to investigate partially absorbing barriers, the simulations assumed narrow gradient pulses in which the phase shift of the spins, due to an applied gradient, is acquired instantaneously.

In the second set of simulations the effect of finite gradient pulses was observed for the case of reflecting walls. The phase shift of the spins for this case was acquired over successive time intervals such that the effect of a finite gradient pulse was represented. For the first case the program calculated the molecular density $\rho(z, t)$, the average propagator, $\overline{P_s}(Z, t)$ and the echo attenuation function $E(q)$. For the finite gradient pulse simulations only the echo attenuation function was calculated. The results from the finite gradient pulse investigation have already been discussed in Section 4.3.

The effect of wall relaxation was simulated by allowing a relaxation layer next to each wall of thickness d. The molecules then have a finite probability, α, to relax if they are within d of the wall for each time interval τ. The proportion of molecules that relax would then be $2\alpha d/a$ for both walls. Over a time period $t = N\tau$ the number of molecules remaining would be

$$\left(1 - 2\alpha\frac{d}{a}\right)^N \tag{6.30}$$

which can be written in terms of an exponential, if $2\alpha d/a \ll 1$, as

$$\exp(-2\alpha Nd/a) \tag{6.31}$$

a (μm)	M (ms^{-1})	D (m^2 s^{-1})	τ (ms)	d (mm)	α	$Ma/2D$	$a^2/2D$ (s)
100	0.00001	2.5×10^{-9}	0.5	0.5	0.01	0.2	2.0
100	0.00010	2.5×10^{-9}	0.5	0.5	0.1	2.0	2.0
100	0.00100	2.5×10^{-9}	0.5	0.5	0.4	20.0	2.0

Table 6.1: Parameters used in partially reflecting barrier simulations with narrow gradient pulses using the Gaussian jump method. Resulting magnetization densities, average propagators and echo attenuation functions are shown in Figures 6.2, 6.3 and 6.4 respectively

or

$$\exp(-\alpha d/a\tau) \tag{6.32}$$

or

$$\exp(-t/T_2) \tag{6.33}$$

where we can define an effective T_2 due to relaxation as

$$T_2 = \frac{a\tau}{2d\alpha} \tag{6.34}$$

comparing this T_2 to Brownstein Tarr theory in case where $Ma/D \ll 1$ we can write

$$T_2 = \frac{a}{2M} = \frac{a\tau}{2d\alpha} \tag{6.35}$$

which results in

$$\alpha = \frac{M\tau}{d} \tag{6.36}$$

It is interesting to note that, if τ is too large, it is possible for α to take on non physical values (i.e. greater than unity). This would reflect a situation where the condition for eqn (6.36) is no longer valid and would require a decrease in the step time to remedy. In our simulations we normally limited α to values smaller than 0.1 and adjusted the step time τ as necessary, although for the most absorbing cases this proved difficult if simulation times were to be kept reasonable. The details of the particular simulations that were performed are given in Table 6.1. They correspond closely to reflecting, intermediate and absorbing situations respectively.

6.3.3 Effect of wall relaxation

The resulting magnetization densities, $\rho(z, t)$, are shown in Figure 6.2 for partially absorbing walls with three different values of M. Superposed on the simulation results in the same Figures are the theoretical $\rho(z, t)$ distributions obtained from the Brownstein-Tarr theory of eqn (6.20). In the highly reflective case shown in Figure 6.2a the spin density is almost constant, as expected for completely reflective walls. The almost fully absorbing wall shown in Figure 6.2c has virtually zero spin density at the walls, and the spin density is dominated by the lowest frequency cosine of the eigenmode expansion.

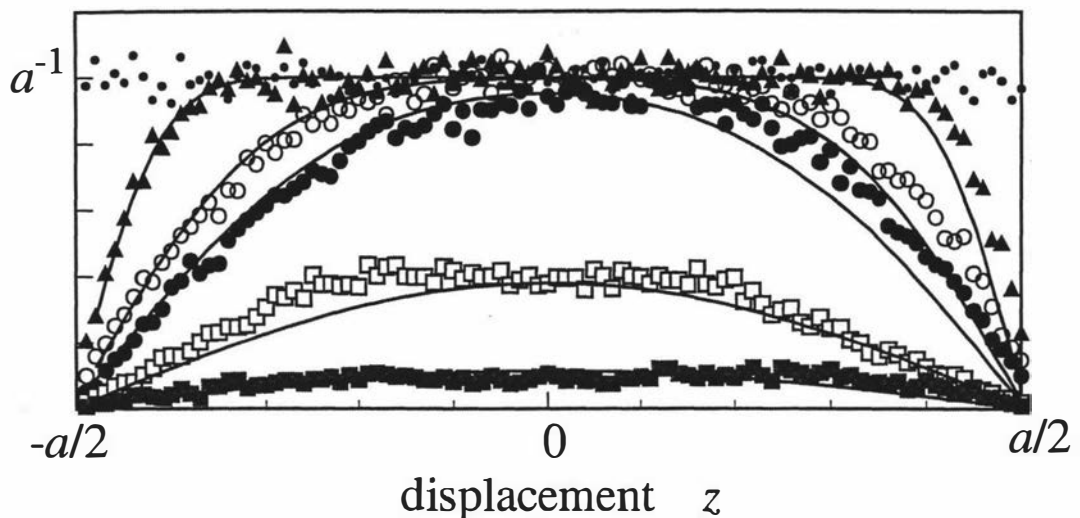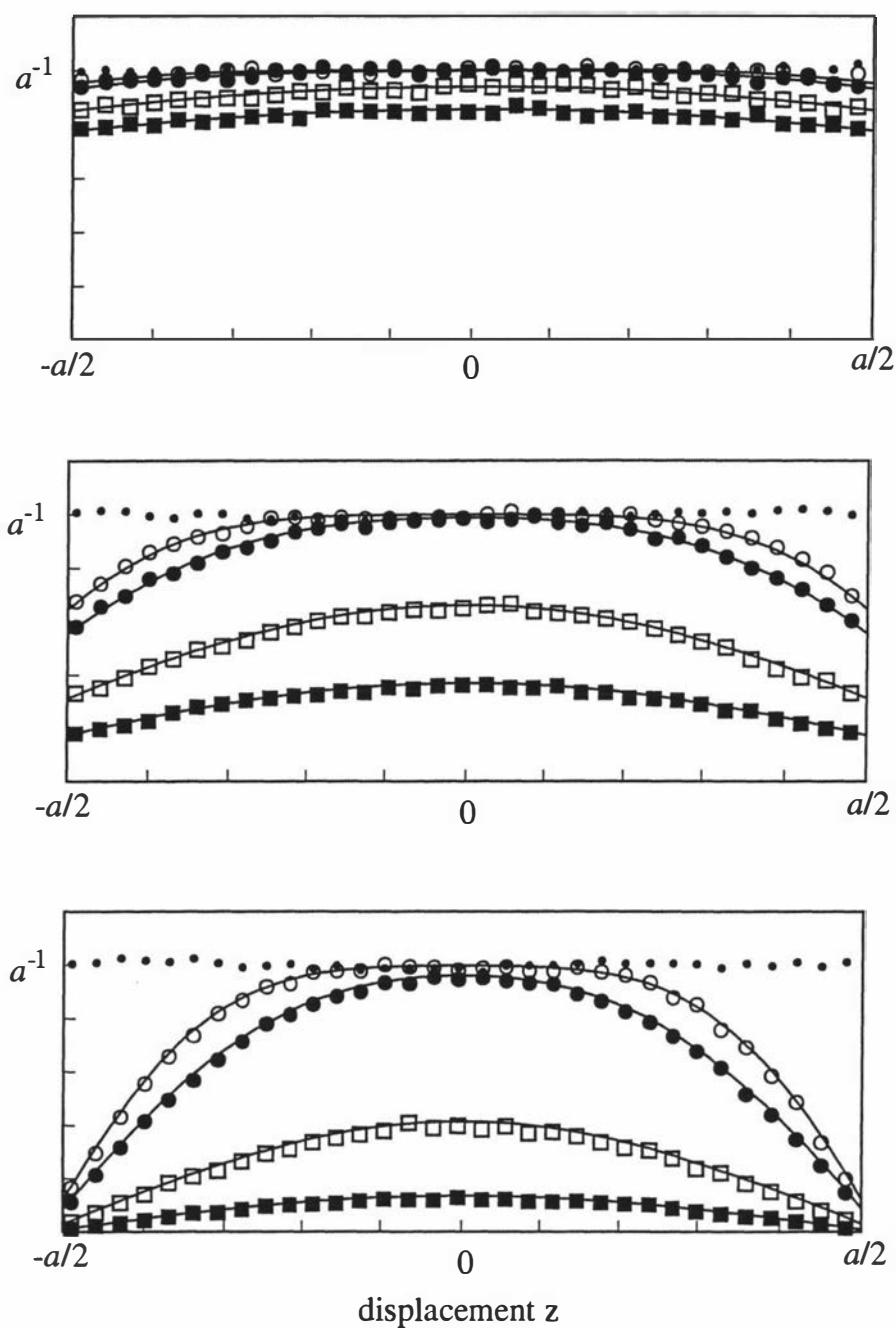**Figure 6.2**: Nuclear spin magnetization densities $\rho(z,t)$ predicted by the Gaussian jump simulation method and theory, eqn (6.20), for partially absorbing walls with $Ma/2D$ of 0.2 (upper), 2 (middle) and 20 (lower). Note that for $t = 0$, the theoretical prediction is a constant, $1/a$. Five successive time intervals are displayed. In multiples of $a^2/2d$, t is, respectively, 0.0 (solid dots), 0.025 (open circles), 0.05 (solid circles), 0.25 (open squares), 0.5 (solid squares).

Figure 6.3 shows the average propagator for each case with the theoretical lines of eqn (6.26) superposed. Since the barrier walls are placed at $\pm a/2$, the possible displacements of a molecule varies from $-a$ to $+a$. In the highly reflecting case Figure 6.3a the long time propagator is a triangular shape, as expected from eqn (4.5). This distribution corresponds to the autocorrelation function of the rectangular profile which describes the density of molecules between the barriers. By contrast, in the highly absorbing case of Figure 6.3c, the cosine-like lowest frequency eigenmode dominates indicated by eqn (6.29)

Figure 6.4 shows the echo attenuation functions, calculated directly from the numerical simulations along with theoretical lines from eqn (6.27). As expected there is a diffraction minimum which arises when qa is close to unity for each simulation. This minimum is consistently evident at each of the M values used here, and is apparent even when the experimental observation time, Δ, is considerably less that $a^2/2D$, the mean time taken to diffuse across the slit. In is also clear from Figure 6.4 that the effect of wall relaxation, $Ma/2D$, is to shift the position of the minimum to higher values of q, a point already noted before. However this shift is quite delicate, and becomes severe only when the wall relaxation is sufficiently strong to attenuate the signal intensity at zero gradient to below 10%. This fact is demonstrated by Figure 6.5.

In Figure 6.5a we show a family of curves corresponding to the position of the minimum as a function of wall relaxation, at different values of the observation time. This shift is plotted as a_{eff}/a where a_{eff} is the sample width one would obtain by assuming the minimum occurs at $qa = 1.0$. This Figure indicates that relaxation could cause discrepancies of up to 30% in structural parameters measured using PGSE. For comparison, in Figure 6.5b the corresponding zero gradient signal intensities are shown. Note that the limiting position of the minimum for perfectly absorbing walls is $1.5a^{-1}$.

6.4 Experiments

While the theoretical result for echo attenuation for plane reflecting barriers in the absence of wall relaxation has been well known for over 20 years, there have been no published results of a "diffraction curve" resulting from a real PSGE experiment on such a sample. Such an experiment would be able to provide direct measurement of the size of the restricting boundaries and would be able to probe distance scales smaller than those attainable by conventional NMR microscopy.

6.4.1 Sample and geometries

A sample comprising microcapillaries with approximately rectangular cross-section and internal width of 100 μm was used to test the restricted diffusion model. Although the application of q-space gradients of sufficient size was easily achieved, the time taken for molecules to diffuse across the width of the microcapillaries needed consideration. For water with a self-diffusion coefficient of 2.5×10^{-9} m^2 s^{-1} the time a^2/D is 4.0 s. The pulse sequencer on the modified FX60 has a maximum of 1×10^6 μs, or 1.0 s, of total time available for any one pulse sequence. Therefore a liquid with a higher self-diffusion coefficient was needed to decrease the time a^2/D. Pentane (C_5H_{12}) has a self-diffusion coefficient of around 5.0×10^{-9} m^2 s^{-1} , reduc-
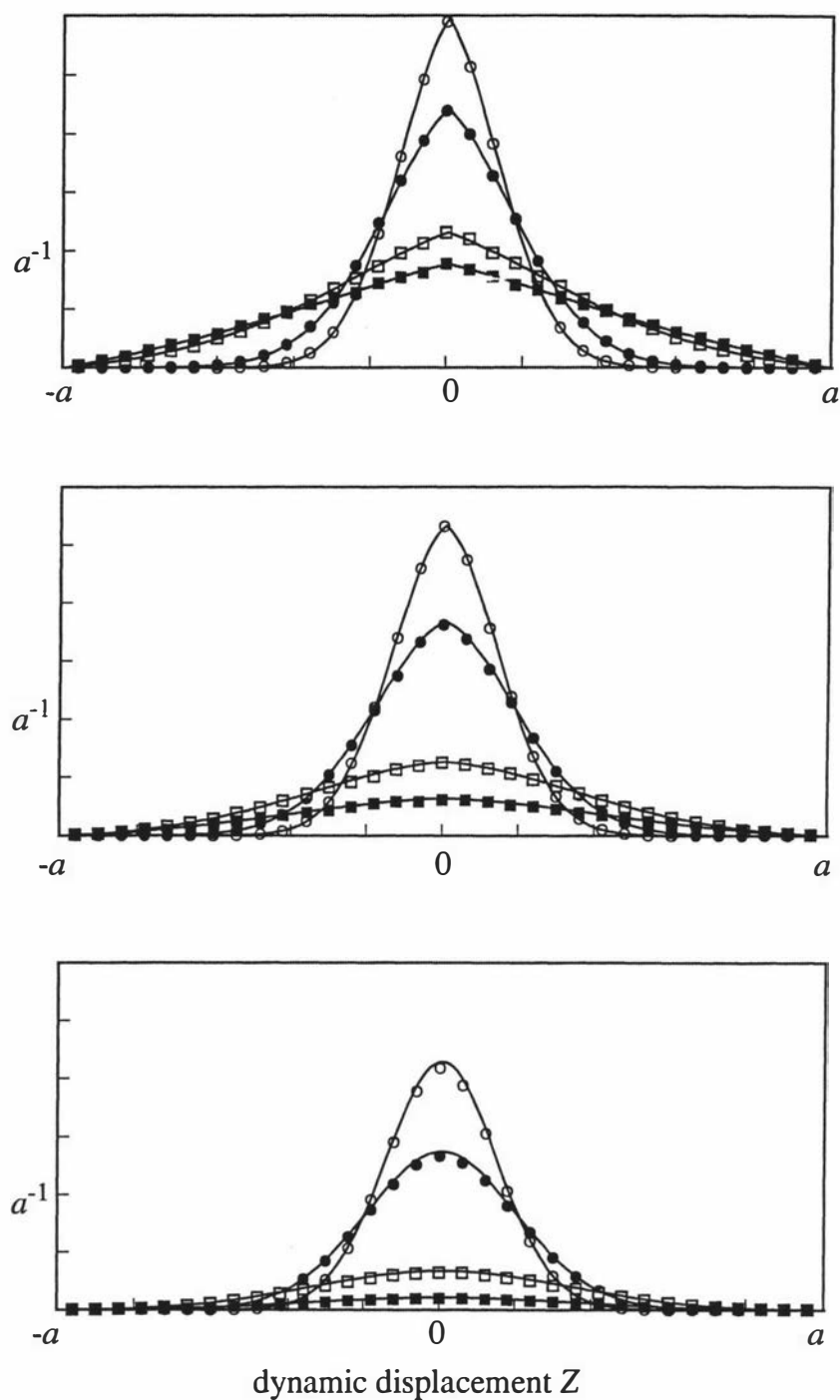
Figure 6.3: Average propagator, $P_s(Z, \Delta)$, for partially absorbing walls predicted by simulations and theory, eqn (6.26) with $Ma/2D$ of 0.2 (upper), 2 (middle) and 20 (lower). Four successive time intervals are displayed. In multiples of $a^2/2d$, Δ is, respectively, 0.025 (open circles), 0.05 (solid circles), 0.25 (open squares), 0.5 (solid squares).
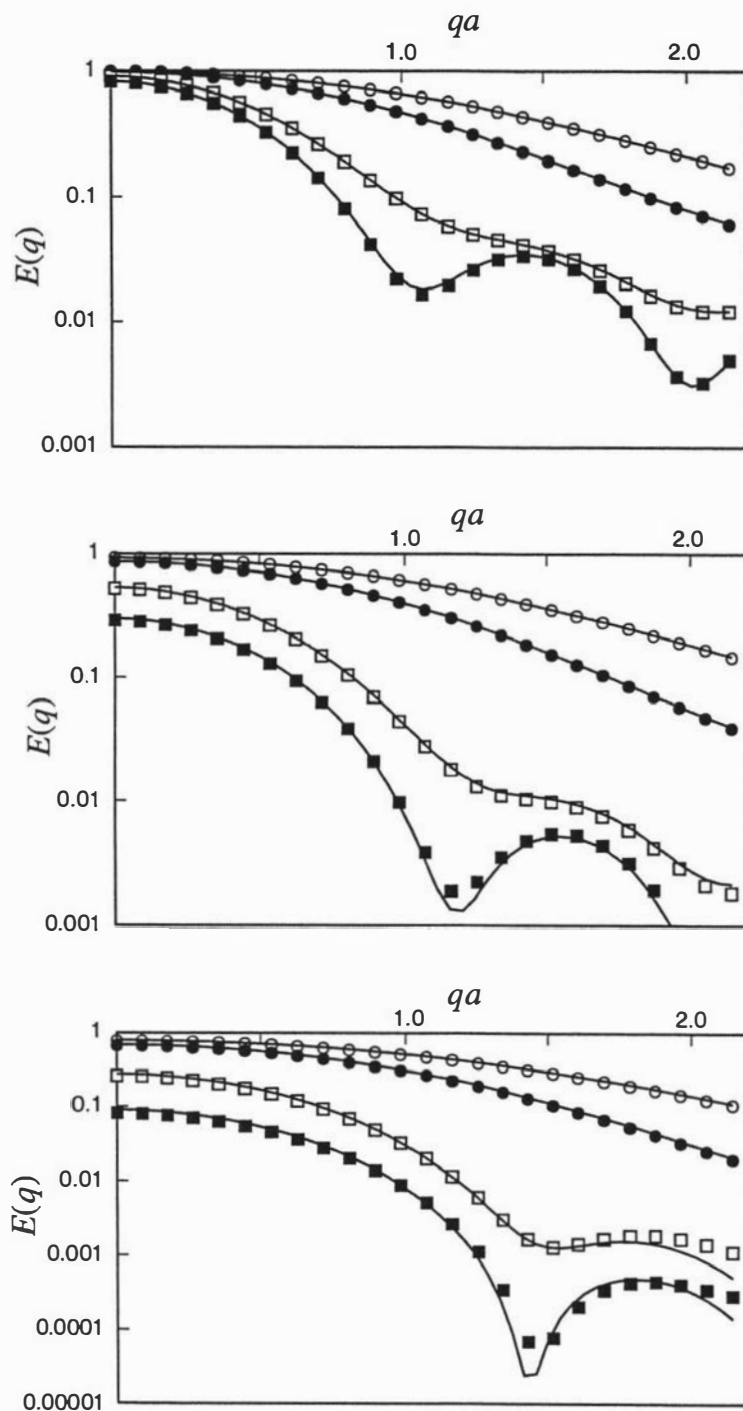
Figure 6.4: Echo attenuation, $E(q)$, for partially absorbing walls predicted by simulations and theory, eqn (6.27), with $Ma/2D$ of 0.2 (upper), 2 (middle) and 20 (lower). Four successive time intervals are displayed. In multiples of $a^2/2d$, Δ is, respectively, 0.025 (open circles), 0.05 (solid circles), 0.25 (open squares), 0.5 (solid squares).
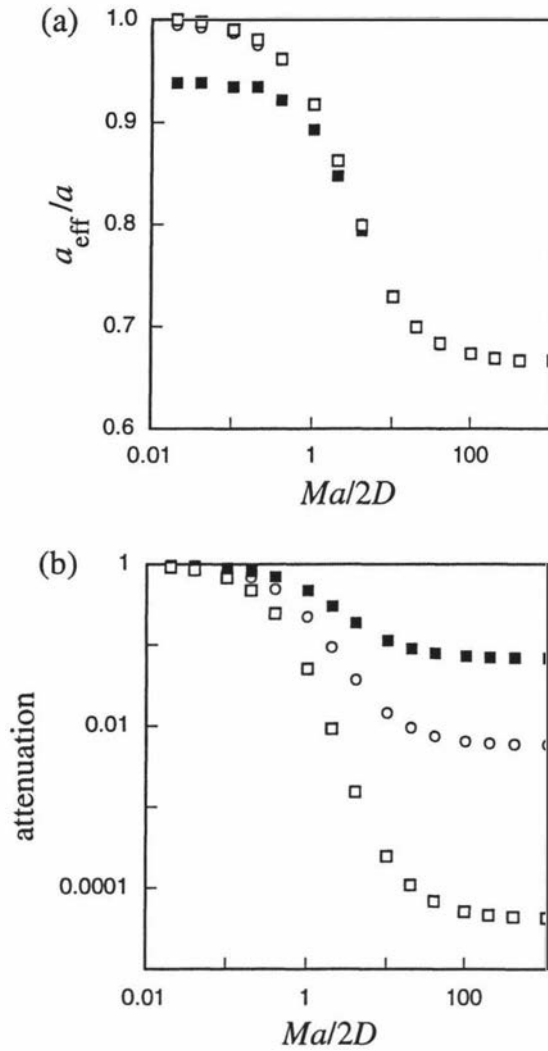
Figure 6.5: (a) shows the diffraction minimum position, a_{eff}^{-1} for partially absorbing walls as a function of $Ma/2D$ for three different observation times, Δ, given by 0.25 (solid squares), 0.5 (open circles), and 1.0 (open squares) in units of $a^2/2D$. The points shown are derived from calculations based on eqn (6.27). (b) shows a corresponding set of points indicating the degree of echo attenuation at $q = 0$.
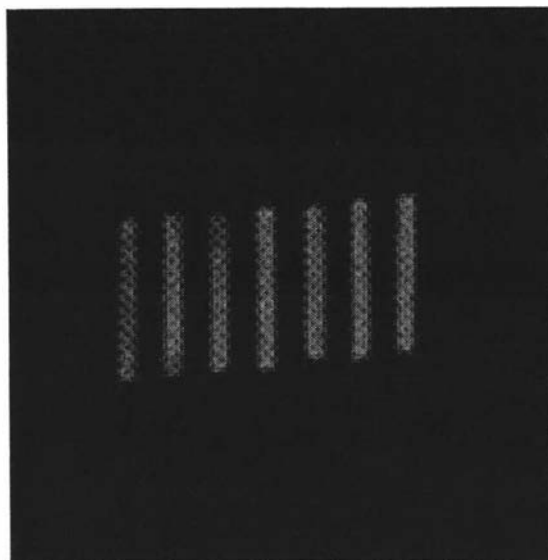
Figure 6.6: An NMR image of the microslide stack used in the PGSE experiments presented in this Chapter. The proton signal is from pentane contained inside each microslide. The narrow dimension between the plane parallel walls is 100 μm. Note that the stack is coincidentally regular and the spacing between each microslide is irrelevant to the diffusive-diffraction experiment of Section 6.5.

ing a^2/D to 2.0 s. After filling with pentane, 7 capillaries were sealed and glued in a parallel stack, in order to provide a sample which filled the r.f. coil volume and provided the maximum possible signal. Figure 6.6 shows a NMR image obtained from the pentane in the capillaries. The microcapillary stack had a square cross section and fitted into a 4 mm o.d. NMR tube. The experiments were carried out on the FX-60 spectrometer using the high gradient PGSE probe using gradients of 1.21 T m^{-1}. The temperature of the sample was maintained at an ambient 28 degrees.

6.4.2   100 μm microslides

In practice PGSE diffraction experiments are difficult due to signal-to-noise considerations. To observe an echo attenuation function with a sinc^2 like behaviour requires good signal acquisition at attenuations of 0.1% of the original echo signal. Even with the best of samples a criteria such as this would be difficult to meet. Liberal use of signal averaging especially at high attenuations and good system stability over a period of days are essential. In this case a variable "ngain" factor was used which increased signal averaging by a factor 2^{ngain} for data points as the expected attenuation of the echo signal increased.

PGSE NMR experiments were carried out with the stack carefully aligned so that the magnetic field gradient direction was normal to the parallel walls of the tubes. Stimulated echo pulse sequences were used in which the gradient pulse duration never exceeded 2 ms $(0.001a^2/D)$ justifying the narrow pulse approximation used in our analysis. The proton T_1 was measured as 1000 ms and the T_2 value as 20 ms. Because the time spent in the transverse plane was always less than 4 ms, the spin relaxation was dominated by T_1 and was never more severe than e^{-1} in the PGSE experiments reported here. It should be noted that the T_1 value observed here corresponded to $M = 0.00005$ and $Ma/2D$ of 0.5, sufficiently low that any shift to the echo minimum due to relaxation is less than 5% and the theory for perfectly reflecting walls provides a close approximation.

Figure 6.7 shows the echo attenuation, $E(q)$, obtained in the capillary stack, at different fixed times, Δ, ranging from 200 ms to 900 ms and corresponding to the range $0.1a^2/D$ to $0.45a^2/D$. Superposed in Figure 6.7a are the theoretical curves obtained using eqn (4.21) (the case of perfectly reflecting walls) in which the known parameters for D and a $(5.0 \times 10^{-9}$ m^2 s^{-1} and 100 μm respectively) are used. Allowance for relaxation $(M = 0.00005)$ using eqn (6.27) produces the results shown in Figure 6.7b. While the inclusion of relaxation leads to an improvement in the fit at shorter values of Δ, the longer time data is less well represented near $qa \approx 1$. In this region the echo amplitude is especially sensitive to the chosen value for D.

6.4.3 Fitting theory to data

In order to allow the theoretical parameters to be adjusted, we have fitted the experimental data to eqn (6.27) by a non-linear least squares method, adjusting the values of a and D, but keeping the wall relaxation M fixed at the measured value. This resulted in the theoretical curves shown in Figure 6.8a along with the parameter values given in Table 6.2.

In practice, there will be some variation in both the plane spacing and the alignment of the different microcapillaries in the stack. The effect of this variation on the echo attenuation data must be considered. We have incorporated such variation by the simple device of convolving a normal distribution of standard deviation σ with the average propagator, corresponding to a Gaussian multiplication of $E(q)$. This allowance for sample imperfection, in which the data is fitted for D, a, and the standard deviation σ, best accounts for the observed echo attenuation, as shown in Figure 6.8b. The results of the fitting are shown in Table 6.2. In each case a is within 7% of the manufacturer's specification while the alignment/spacing standard deviation value is less than 5%. D values, which arise predominantly from the fit to the low q part of the data, are all close to the known self-diffusion coefficient of pentane at 28 °C, 5×10^{-9} m^2 s^{-1}.

Although none of the theoretical curves completely and consistently fit the data they do give good indications of the size of the structural parameters being investigated in the microslide sample. The PGSE analysis also provides, at worst, an estimation of the upper limit of wall relaxation and width variation in the sample. Although such a well defined rectangular sample is unlikely to occur in most samples of interest it is useful in order to demonstrate the fundamental physics of the problem.

These experiments also show that the diffraction minimum in the echo attenuation function becomes apparent for times, Δ, considerably less than a^2/D. Given
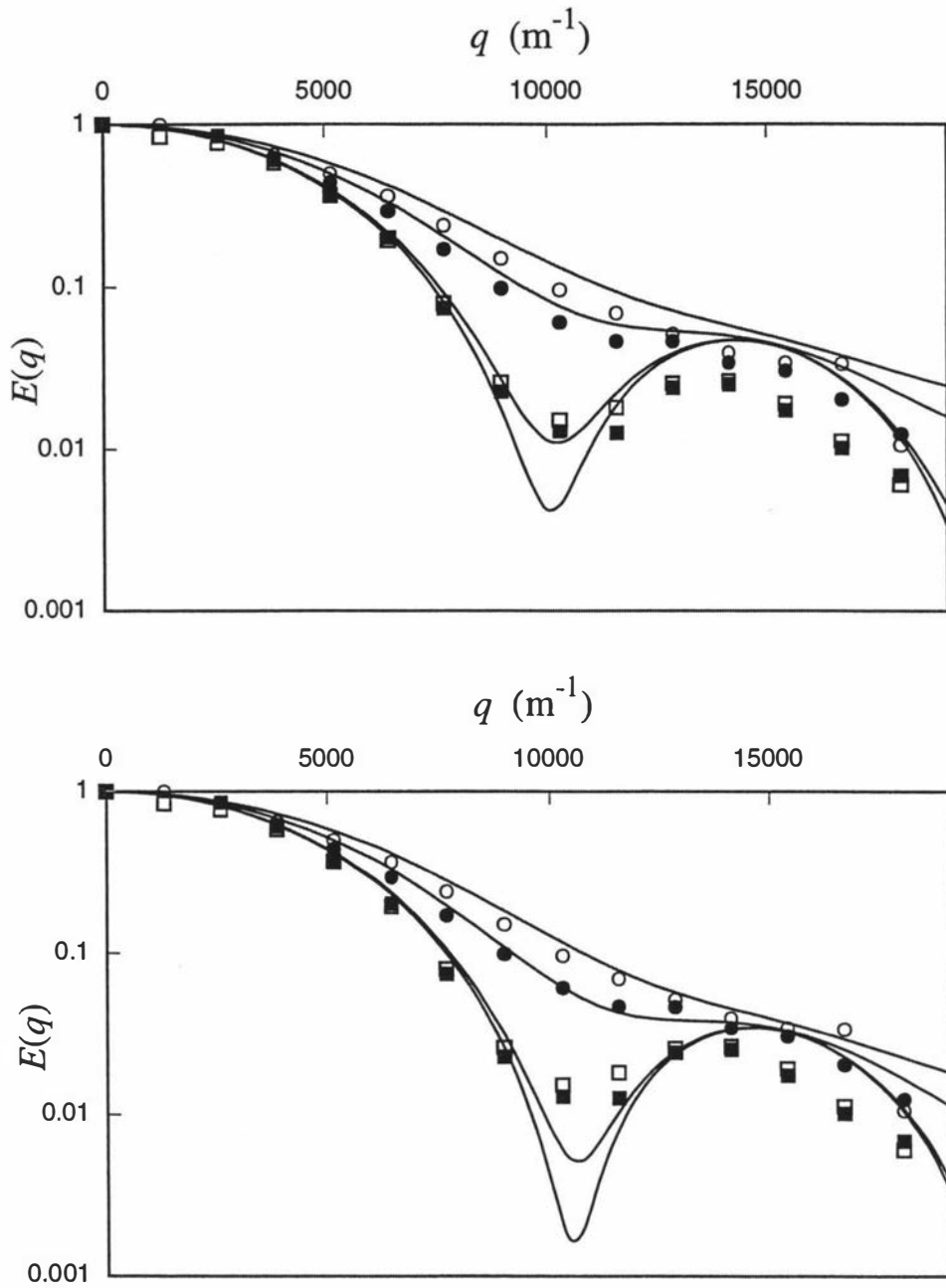
Figure 6.7: Echo attenuation data, $E(q)$, obtained from PGSE experiments using the microslide stack shown in Figure 6.6. The four different fixed times, Δ, are 200 ms (open circles), 300 ms (closed circles), 700 ms (open squares) and 900 ms (closed squares). These times correspond to the range $0.1\ a^2/D$ to $0.45\ a^2/D$. Theoretical curves from eqn (6.27) are shown where the known system parameters are used ($a = 100\ \mu$m, $D = 5.0 \times 10^{-9}$ m^2 s^{-1}. In the upper graph perfectly reflecting walls are assumed, $M = 0$, while in the lower graph partial absorption is allowed for, $M = 0.000\ 05$, consistent with the measured value of T_1.
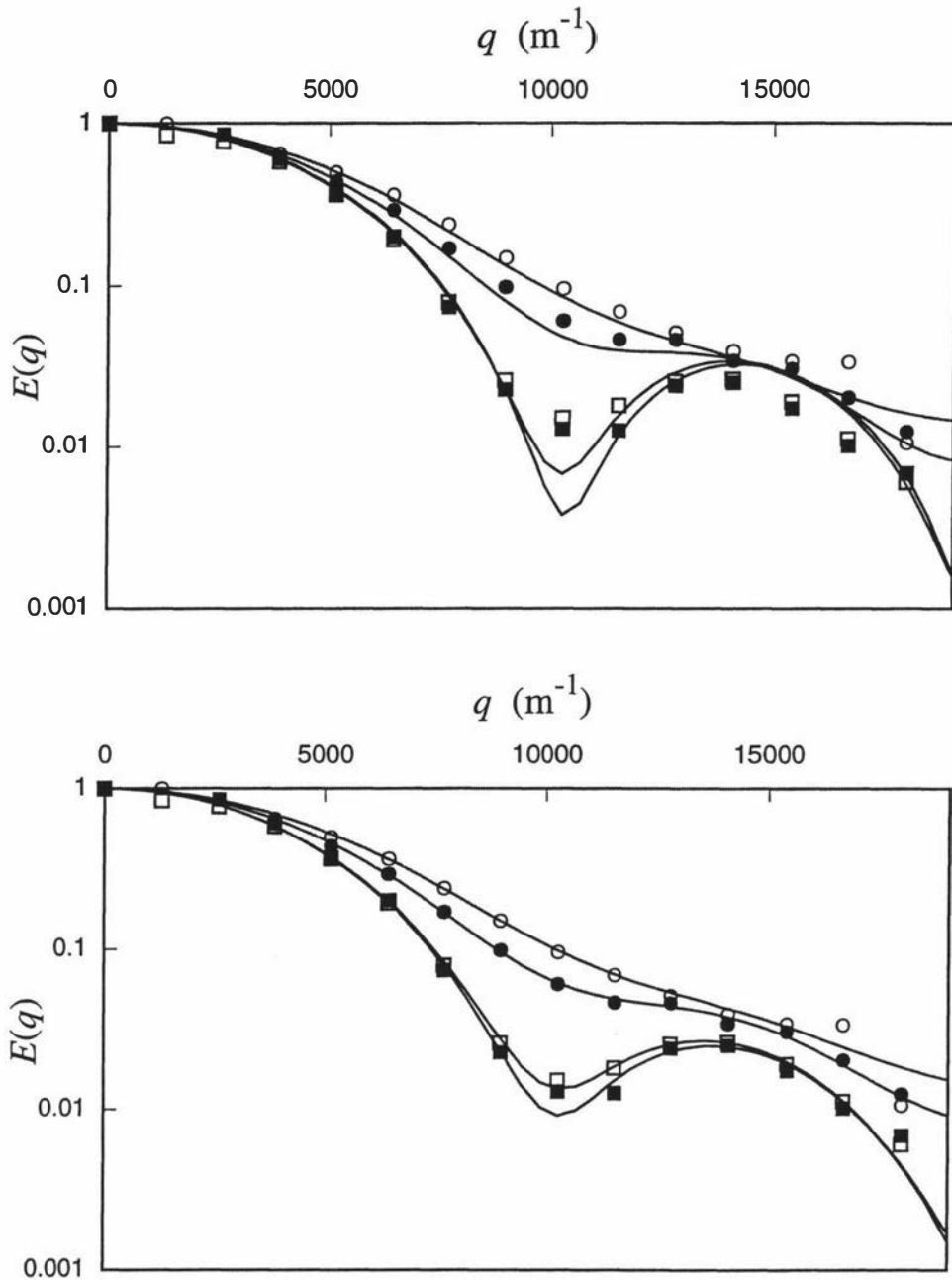
Figure 6.8: Echo attenuation data, $E(q)$, as for Figure 6.7 but in which the theoretical curves have been fitted to the data. In the upper graph the wall relaxation is held fixed at $M = 0.000\,05$ while a and D are varied to obtain best fits. In the lower graph no relaxation is assumed ($M = 0$), but a distribution, σ, of a values is allowed for. Both a and D are varied as well as σ to produce best fit lines. Values obtained for fits in both graphs are shown in Table 6.2.

	Best fitting with wall relaxation			Best fitting with variance in a		
Δ (ms)	a (μm)	D (m^2 s^{-1})	M (ms^{-1})	a (μm)	D (m^2 s^{-1})	σ (μm)
200	112	6.0	0.000 05	106	5.8	4.5
300	108	5.8	0.000 05	105	5.4	5.2
700	105	5.0	0.000 05	101	4.3	8.7
900	103	4.35	0.000 05	100	3.7	9.1

Table 6.2: Parameters a and D obtained by fitting the echo attenuation data. In one set the relaxation parameter M is kept at the known (experimental) value while in the other a distribution of a values is allowed and the variance σ fitted.

that neither wall relaxation nor finite gradient pulses destroy the q-space structural information, and noting that the gradients used here were weak compared to the available gradient strength, the possibility to extend this technique to smaller and more interesting samples appears promising for future work.

6.5 Edge enhancement effects

As part of the restricted diffusion experiments performed in the previous section, I acquired NMR images of the microslide stack sample using the commercial Bruker AMX300 (300MHz) system in our laboratory. During these experiments I noticed a remarkable edge-enhancement effect in some images of a nature that seemed similar to an edge-enhancement effect described by Pütz *et al.*[60] and Hyslop and Lauterber[61]. However, upon further investigation we found[62] that the mechanism for this phenomenon was a differing signal attenuation due to restricted diffusion rather than a line-narrowing diffusive effect.

6.5.1 Theory

Diffusive-spectral edge enhancement

The lineshape hypothesis of Pütz *et al.* is described in detail in their paper[60]. They obtain a result using a one-dimensional representation of diffusing molecules contained between parallel compartment walls of separation d. In the presence of a read (frequency-encoding) gradient of amplitude G, such as might be used in Spin Warp or Projection Reconstruction imaging, the nuclear spin spectrum for stationary molecules would be rectangular with spectral width $\omega = \gamma G \delta$, γ being the nuclear gyromagnetic ratio. However the translational motion associated with self-diffusion causes molecules to sample a variety of local Larmor frequencies, thus motionally narrowing the spectrum. The usual exchange criterion, determined by a relevant exchange time, τ, is $d^2/2D$, namely the time taken to traverse the compartment.

When $\omega\tau \ll 1$, the spectrum will reduce to a narrow line yielding an image of the compartment in which all the spins appear to reside at the compartment centre. It is in the intermediate exchange region, $\omega\tau \sim 1$, that surprising effects arise. Restricted diffusion near the compartment walls causes a "peaking of the spectrum" as reflections at the walls pushes the mean molecular positions slightly towards

the centre of the diffusion interval. We term this phenomenon "diffusive-spectral edge enhancement". The calculations of Pütz *et al.* showed that these spectral edge enhancement peaks may have a fractional amplitude of order 30% while their fractional displacement from the wall is of order $(4\pi D/\gamma G\delta^3)^{1/3}$ or $(2\pi/\omega\tau)^{1/3}$. In consequence, even such very slow exchange conditions as $\omega\tau \approx 10^4$, can lead to noticeable edge enhancement effects, according to this model.

To calculate the size of this effect in an NMR imaging experiment we assume a voxel dimension Δx with N voxels across the dimension d. The exchange criterion parameter is given by

$$\omega\tau = (\gamma G N^3 \Delta x^3 / 2D). \tag{6.37}$$

Taking a typical water diffusion value of 1×10^{-9} m^2 s^{-1}, $\Delta x = 10$ mm and $N = 256$, exchange narrowing $\omega\tau < 1$ requires gradients smaller than 5×10^{-10} T m^{-1}! Even the slow exchange condition $\omega\tau \approx 10^4$ requires gradients below 5×10^{-6} T m^{-1} to be visible. This corresponds to an unrealistically small image bandwidth of around 1 Hz. Such small gradients are impracticable because of the need to overcome magnet inhomogeneity and internal susceptibility inhomogeneity effects. Clearly the key factors determining scaling are Δx^3 and N^3. Even if the resolution limit could be improved to 5 mm, a maximum of 11 pixels across the compartment is permitted in order to observe diffusive-spectral enhancement at realistic bandwidths of a few kHz. This suggests that such effects are at the margins of attainability in practical NMR Microscopy.

Diffusive-relaxation edge enhancement

The mechanism for the effect we observed relates to the diffusion of the sample molecules in the presence of an imaging field gradient. Under certain conditions the imaging gradients can cause significant attenuation of the image signal dependent on the self-diffusion coefficient of the molecules. However near the walls of a container the self-diffusion of molecules is restricted and is significantly smaller than that for the bulk liquid. This reduces the attenuation of the signal from molecules at the walls, compared to the signal from the faster diffusing center of the sample, and leads to the apparently enhanced edges observed below.

This effect, which we term "diffusive-relaxation edge enhancement", is considerably more influential than spectral edge enhancement.

Consider the spin warp imaging sequence shown in Figure 6.9. Molecular self-diffusion in the presence of both the phase-encoding and frequency-encoding imaging gradients will result in image attenuation, the predominant signal reduction being caused by the read gradient whose total duration is greatest. According to the Stejskal-Tanner equation[17], eqn (3.25), the read gradient echo attenuation factor is[62]

$$E(G) = \exp(-\gamma^2 G^2 (NT/2)^2 (\Delta - NT/6)) \tag{6.38}$$

where Δ is the separation of the leading edges of the read gradient pulses and T is the acquisition dwell time, corresponding to an acquisition bandwidth $1/T$. For compression of Δ to the minimum possible duration, $NT/2$, this yields,

$$
\begin{aligned}
E(G) &= \exp(-\gamma^2 G^2 (NT/2)^2 (NT/3)) \\
&= \exp(-\frac{1}{3}\pi^2 NTD/\Delta x^2) \tag{6.39}
\end{aligned}
$$
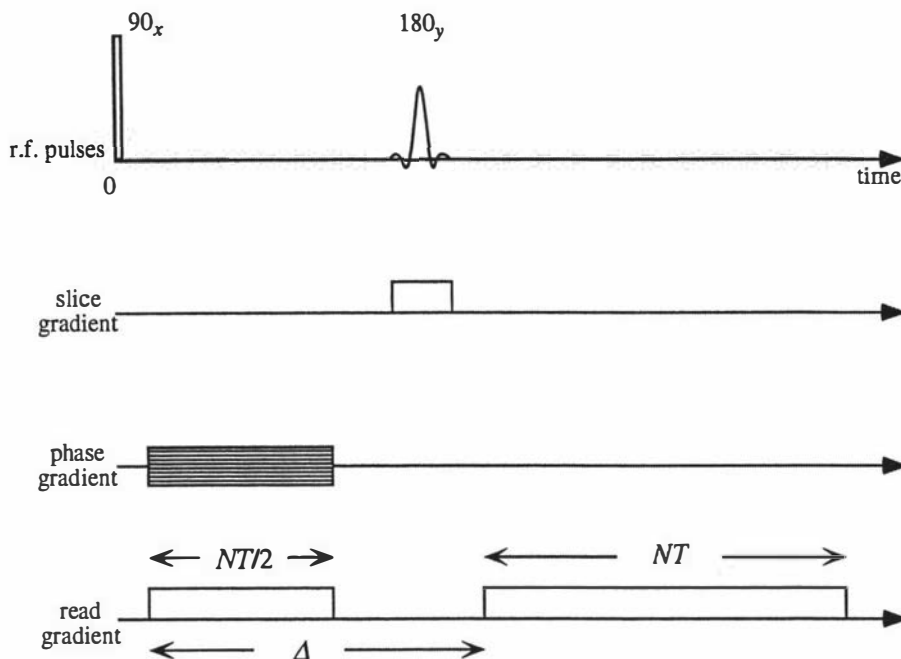
Figure 6.9: The spin-warp sequence used to acquire the image shown in Figure 6.6 and Figure 6.11. The sampling dwell time is T which leads to an acquisition bandwidth of $1/T$. The diffusion time between the two pulses is indicated by Δ.

or

$$E(G) = \exp(-\frac{1}{3}\pi^2 N^3 T D/\text{FOV}^2) \tag{6.40}$$

where the field of view, FOV, is $N\Delta x$. Eqn (6.39) shows that diffusive attenuation effects will be significant when the mean-squared displacement over the observation time, $NT/2$, is on the order of the pixel size Δx. Both equations (6.39) and (6.40) indicate the sensitivity of the diffusive echo attenuation to N. In addition it should be noted that the exponent is four times smaller in the case of phase gradient attenuation and can therefore be neglected by comparison with the read gradient.

Diffusive relaxation effects will be significant when the exponent in eqn (6.39) exceeds unity, giving the inequality,

$$D \geq \frac{3\gamma G d^3}{2\pi^2 N^3} \tag{6.41}$$

By contrast spectral enhancement at a minimum exchange parameter, $\omega\tau$, requires

$$D \geq \frac{\gamma G d^3}{2\omega\tau} \tag{6.42}$$

Even with slow exchange effects, such that the exchange parameter is on the order of 10^4, it is clear that diffusive relaxation will dominate provided $N \geq 10$.

As part of this thesis I have calculated the spatial dependence of the echo attenuation function. The profile of the edge effect for a rectangular box of width a can be calculated two ways. The mean square displacement of a molecule can be calculated as a function of position in the sample, z, by substituting the propagator for molecules confined to a box, eqn (4.20), into

$$\overline{\langle Z^2(z)\rangle} = \int_0^a P_s(z|z', \Delta)(z' - z)^2 \, \mathrm{d}z' \tag{6.43}$$

which gives

$$\langle \overline{Z^2(z)} \rangle = \frac{a^2 - 3az + 3z^2}{3}$$
$$+ \sum_{n=1}^{\infty} \frac{4a}{n^2\pi^2} \cos(\frac{n\pi z}{a}) \exp(\frac{-n^2\pi^2 D\Delta}{a^2})(z + (-1)^n(a - z)) \qquad (6.44)$$

The echo attenuation as function of position can be calculated using eqn (3.43) where δ, Δ and g are determined by the duration and strength of the read gradient pulses.

Alternatively if narrow read gradient pulses are assumed then eqn (3.36) can modified to reveal a position dependant echo attenuation function. Although a narrow gradient pulse approximation is strictly not applicable to most imaging sequences, it will give, at least, a good initial approximation of the image profile.

$$E(q, z) = \int_0^a P_s(z|z', \Delta) \exp(-i2\pi q(z' - z)) \, \mathrm{d}z' \qquad (6.45)$$

which gives a result for $E(q, z)$ with both phase and magnitude. This is simple to understand as a phase shift is the result of any velocity-like net motion of the spins. For molecules an the left of the box there is a higher probability of moving to the right of the box over a time interval than to the left. Hence the position dependent echo attenuation will have both real and imaginary parts, except at the center of the sample. The result from eqn (6.45) for the rectangular box is

$$E(q, z) = \exp[i\pi q(a - 2z)]$$
$$\times \left[\frac{sin(\pi q a)}{\pi q a} + (8\pi q a) \sum_{n_{even}} \exp\left(\frac{-n^2\pi^2 D\Delta}{a^2}\right) \cos\left(\frac{n\pi z}{a}\right) \frac{sin(\pi q a)}{(2\pi q a)^2 - (n\pi)^2} \right.$$
$$\left. + i(8\pi q a) \sum_{n_{odd}} \exp\left(\frac{-n^2\pi^2 D\Delta}{a^2}\right) \cos\left(\frac{n\pi z}{a}\right) \frac{cos(\pi q a)}{(2\pi q a)^2 - (n\pi)^2} \right] \qquad (6.46)$$

Figure 6.10 shows imaging profiles for a rectangular box sample calculated using eqn (6.44) and eqn (6.46). The profiles shown in Figure 6.10b and 6.10c are similar for small attenuations but differ considerably for larger diffusion times.

The diffusive relaxation effect is not restricted to Fourier imaging. If spin or gradient echoes are used with projection reconstruction imaging, a very similar expression results. Such attenuation can only be avoided entirely by using a three dimensional projection reconstruction in which the origin of signal acquisition coincides with the application of read gradients following a non-selective excitation pulse.

6.5.2 Experiments

Figure 6.6 shows an image I obtained using the spin warp sequence of Figure 6.9 for a phantom of pentane contained in rectangular glass capillary tubes of interior cross-section 100 mm × 3000 mm. For this image, obtained at a bandwidth of 20 kHz, the value of N is 128, the pixel dimension is $(32 \ \mu m)^2$ and very little diffusive relaxation occurs. By contrast Figures 6.11a and 6.11b show the phantom imaged at identical bandwidth and FOV but with $N = 256$ and a pixel dimension of $(16 \ \mu m)^2$. According to eqn (6.38) the freely diffusing water will suffer an attenuation factor of $\exp(-3.7)$. In these experiments the read gradient is respectively parallel
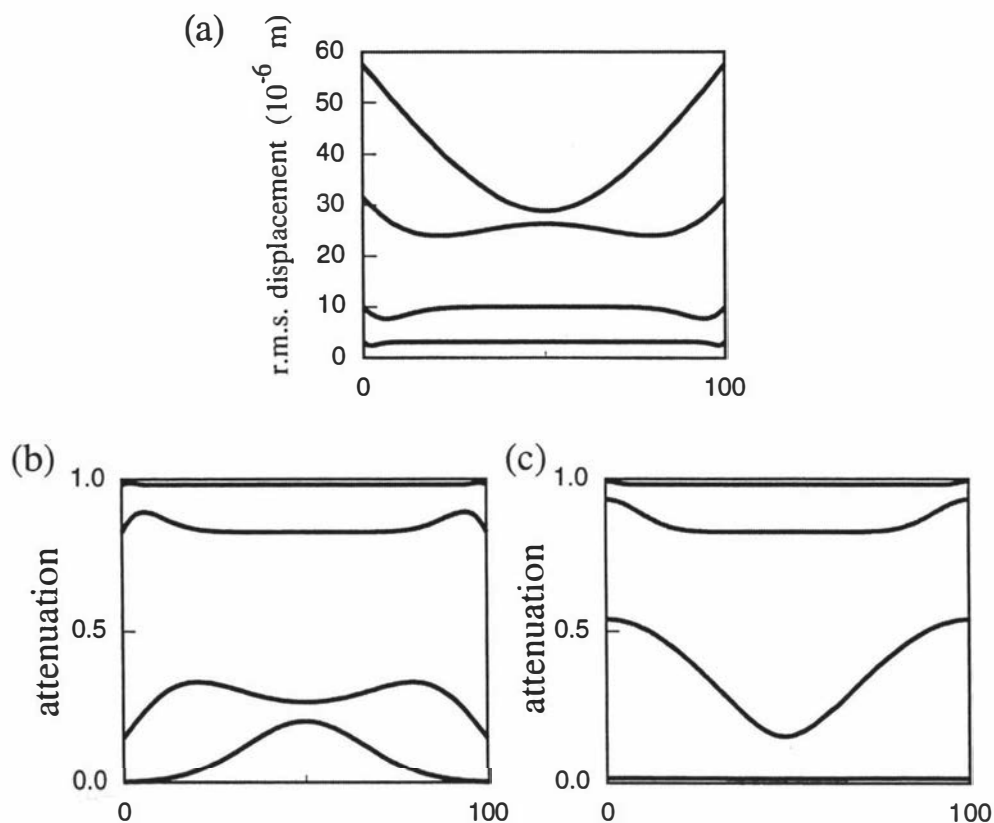
Figure 6.10: (a) The r.m.s. displacement calculated from eqn (6.44) for a box of width 100 μm and $D = 5.0 \times 10^{-9}$ m^2 s^{-1}. The lines show the r.m.s. displacement as a function of the molecules starting position inside the box for diffusion times of 0.001 s, 0.01 s, 0.1 s and 1 s for increasing displacements respectively. (b) The corresponding attenuation as a function of molecule starting position for the case shown in (a), for typical imaging gradient strengths using eqn (3.43) to calculate the attenuation. (c) The attenuation as a function of starting position for identical parameters as in (a) and (b) but using the magnitude of eqn (6.46) to calculate the attenuation.
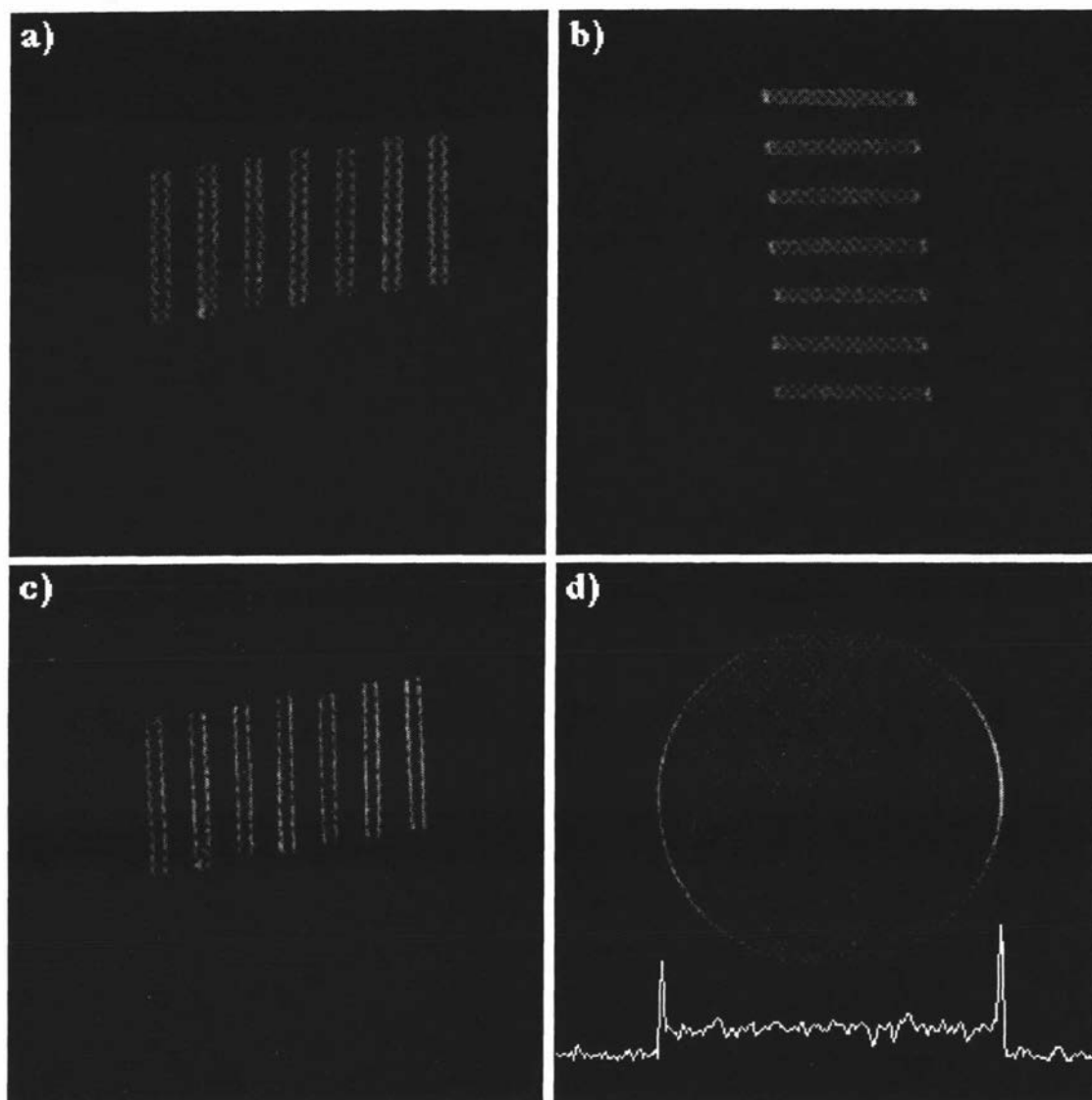
Figure 6.11: (a) to (c) ^{1}H NMR images of the microcapillary stack shown in Figure 6.6. (a) Acquisition bandwidth of 20 kHz using $N = 256$ and with the read gradient perpendicular to the walls. Significant diffusive attenuation results in the brighter edge enhancement at the walls where self-diffusion is restricted. (b) As for (a) but with the read gradient parallel to the walls. (c) As for a but with an acquisition bandwidth of 40 kHz. The diffusion time $NT/2$ is one-half the duration of the 20 kHz case. The bright band at the walls are narrower because of the shorter time over which diffusion occurs. (d) An image acquired by L. C. Forde[63, 62]. ^{1}H NMR image of a water-filled capillary, obtained with acquisition bandwidth 10 kHz using $N = 256$ with a 3 mm field of view. A crescent of edge enhancement is apparent due to the (horizontal) read gradient.

and perpendicular to the transverse dimension of the capillary. Near the walls, where diffusion is restricted, the effect of local reduction in D causes dramatic edge enhancement effects as the attenuation exponent reduces.

Figure 6.11c shows the result of increasing the bandwidth and thereby decreasing the time, $NT/2$, over which diffusion occurs. The bright bands, corresponding to molecules whose diffusion is restricted, are noticeably narrower. Pentane was chosen for these experiments because of the large self-diffusion coefficient and the resulting significance of diffusive attenuation at relatively coarse spatial resolution. However similar edge enhancement effects can also be observed in water, as apparent in Figure 6.11d, an image acquired by L. C. Forde[63, 62], provided that the pixel dimension is reduced. In this latter experiment, using a 1.5 mm I.D. capillary tube, restricted diffusion along the read gradient direction leads to bright crescent features at the edge of the capillary tube. Other bright features in the image also suggest reduced diffusive-attenuation, possibly due to local susceptibility inhomogeneity arising from suspended dust particles[62]. Hills and Snaar[64] have also noted this effect in a one-dimensional profile experiment on a film of water.

6.6 Summary

The experiments on the parallel barrier microslides show convincingly that the fundamental idea of a q-space, diffraction approach to PGSE is both possible and useful in obtaining real structural parameters on samples of interest. The PGSE data acquired contains qualitative "diffractive" features directly related to the size and structure of the enclosing boundaries. As well, an analytic theory can be numerically fitted to the data to give quantitative information about the structure. To date, analytic theories exist for rectangular, cylindrical and spherical geometries which incorporate relaxation effects at the boundaries. Non-linear least squares fitting of the parallel plane analytic theory to the microslide PGSE data gives the parameter a, the width of the microslides, to within 10% of the expected value of 100 μm. The parameters a and D were larger at small Δ times, and approached the expected values at longer values of Δ. The model incorporating a Gaussian variation in the barrier width gave move consistent values than the relaxing wall model. However the Gaussian variation in barrier width model is only strictly correct in long time limit, which suggests a good reason for the deviation of fitted parameters for shorter times.

This approach to PGSE, in contrast to traditional techniques previously used in this field, opens the possibility of a form of micro-imaging, where structural information is revealed, at resolutions far below those attainable by NMR microscopy. The signal-to-noise ratio is only limited by that available from the whole sample and, although a relatively large sample was used for these experiments, distances down to 0.1 μm can easily be measured with an appropriate slow-diffusing liquid given the current gradient strengths available. It is worth noting that to date, these are the only published[37] PGSE experiments showing the diffractive minimum predicted for fully restricted diffusion in any geometry.

The NMR imaging experiments on the microslides suggest that restricted diffusion leads to significant contrasts in NMR microscopy. In fact the local propagator can be directly imaged, revealing detail not available in PGSE experiments. This form of imaging is limited to large samples, above 10 μm, given the current reso-

lution constraints on NMR microscopy. However, as the resolution limits of NMR microscopy are pushed to smaller distances, the restricted diffusion effects reported here[62] will become increasingly significant.

In the Chapter 7 the effect of interconnections between enclosed "pores" will be investigated and the diffractive, q-space approach is used to reveal important structural information about the sample under investigation.

Chapter 7

Porous Media

7.1 Introduction

Fluid transport in porous media is important to a wide range of problems in science, in particular to research concerning oil recovery, catalysts, fluid penetration of plastics and ceramics and biological perfusion. PGSE provides a unique method to observe the diffusion process *in vivo* in porous systems. The ability to differentiate between chemical species in the diffusing liquid also provides further possibilities.

The single slit diffraction-like ideas used as an analogy in restricted diffusion can be extended to porous systems through an analogy to multiple slit interference. In fact an analytic expression can be written for the narrow pulse echo attenuation function based on a pore hoping formalism for the diffusion process. A solution for the case of molecules diffusing between pores separated by thin permeable membranes was found by Tanner[65] in 1978. His solution represents the limiting case where the pore size is equivalent to pore spacing. However, it is interesting to note that in this paper, Tanner observed some "unusual effects" in the echo attenuation function when plotted as a function of gradient strength.

7.2 Porous theory

The following theory[31, 38, 66, 67] concerning porous system diffusion is based on two fundamental assumptions. The first is that the experiment is carried out in such a way that the narrow gradient pulse approximation is valid. This premise enables the use of the Fourier type formalism presented in eqn (4.2) and the diffractive consequences[66]. For pores of size a and a fluid with self-diffusion coefficient D the premise mathematically indicates that the gradient pulse duration should satisfy the condition $\delta \ll a^2/D$.

The second assumption is a pore equilibration approximation[66]. The premise here is that the fluid molecules move quickly inside a pore but more slowly between pores, in other words the porous structure is relatively enclosed and not too open. For pore spacings of b with and effective diffusion *between* pores of D_{eff} this implies that $a^2/D \ll b^2/D_{\text{eff}}$. This assumption says that when a molecule "jumps" to a new pore it quickly equilibrates itself within that pore enabling the use of the long time limit expression for the echo attenuation due to the pore and separating inter-pore effects from intra-pore ones.

It is helpful to initially consider a perfectly periodic set of N identical connected

pores arranged along the z axis of pore spacing b and pore dimensions a. The total pore density can be represented by a superposition of identical local pores with density $\rho_0(z - z_i)$ where z_i is the center of the ith pore and ρ_0 is 0 everywhere outside that pore. Therefore for N pores the normalised total density is

$$\rho(z) = \frac{1}{N} \sum_{i=1}^{N} \rho_0(z - z_i) \tag{7.1}$$

If a spin starts at a point z in pore i then the conditional probability function $P_s(\mathbf{r}|\mathbf{r}', \Delta)$ can be written

$$P_s(z|z', \Delta) = \sum_{j=1}^{N} p(i|j, \Delta)\rho_0(z - z_j) \tag{7.2}$$

where $p(i|j, \Delta)$ gives the probability that a particle starting in pore i will diffuse to pore j in a time Δ. This separation of local pore effects from intra-pore effects is a consequence of the pore equilibration assumption. Substituting eqn (7.1) and eqn (7.2) into eqn (3.36) one gets

$$
\begin{aligned}
E(q) &= |S_0(q)|^2 N^{-1} \sum_i \sum_j p(i|j, \Delta) \exp[\mathrm{i}2\pi q(z_i - z_j)] \\
&= |S_0(q)|^2 F(q, \Delta)
\end{aligned}
\tag{7.3}
$$

where

$$S_{0j}(q) = \int_j \rho_0(z - z_j) \exp[\mathrm{i}2\pi q(z' - z_j)] \mathrm{d}z' \tag{7.4}$$

and the product $S_{0i}^*(q)S_{0j}(q)$ is $|S_0(q)|^2$ for identical pores. For a structure with variable pore geometry an "average pore structure factor" can be defined as $\overline{S_{0i}^*(q)S_{0j}(q)}$ yielding $\overline{|S_0(q)|^2}$.

Making the substitution $n = i - j$ eqn (7.2) can be rewritten in the limit of large N as

$$F(q, \Delta) = \sum_n p(n, \Delta) \exp[\mathrm{i}2\pi q n b] \tag{7.5}$$

where

$$p(n, \Delta) = \frac{1}{N} \sum_i p(i|i + n, \Delta) \tag{7.6}$$

It can be seen that the function $F(q, \Delta)$ can be separated into a pore position (or lattice) function weighted by a inter-pore diffusion function. This can be made clear through the use of the Gaussian envelope (GE) approximation.

7.2.1   Gaussian envelope model

An initial assumption for $p(n, \Delta)$ can be a Gaussian probability function[66, 31, 67] with a long-range diffusion coefficient D_{eff} giving

$$p(n, \Delta) = b(4\pi D_{\mathrm{eff}}\Delta)^{-1/2} \exp\left(\frac{-n^2 b^2}{4D_{\mathrm{eff}}\Delta}\right) \tag{7.7}$$

which upon substitution into eqn (7.5) gives

$$F(q, \Delta) = \int b \sum_n \delta(Z - nb) C(Z, \Delta) \exp[i2\pi q Z] \tag{7.8}$$

where $C(Z, \Delta)$ is a Gaussian distribution of displacements given by

$$C(Z, \Delta) = (4\pi D_{\text{eff}} \Delta)^{-1/2} \exp\left(\frac{-Z^2}{4D_{\text{eff}} \Delta}\right) \tag{7.9}$$

From eqn (7.9) it is apparent that $F(q, \Delta)$ is the Fourier transform of the product of two functions, $C(Z, \Delta)$ and $L(Z)$ where

$$L(Z) = b \sum_n \delta(Z - nb) \tag{7.10}$$

This function $L(Z)$ can be thought of as a one-dimensional lattice-correlation function describing the relative displacement of pores along the z axis. Using the convolution theorem eqn (7.3) can be rewritten

$$E(q) = |S_0(q)|^2 [\mathcal{F}[L(Z)] \otimes \mathcal{F}[C(Z, \Delta)]] \tag{7.11}$$

where $\mathcal{F}$ represents Fourier transformation. The optical diffraction analogy can be made clear by treating $|S_0(q)|^2$ as the individual slit diffraction pattern. $L(Z)$ then represents the position of each slit and $C(Z, \Delta)$ a function which increases the number of slits included in the diffraction pattern as a function of time. The origin of $C(Z, \Delta)$ is the increase in the number of "scattering centers" which increases with Δ as the molecules diffuse to more distant pores. So while $|S_0(q)|^2$ will lead to a diffractive *minimum* around $qa \simeq 1$, $F(q, \Delta)$ will give interference *peaks* at $qb \simeq 1$ which, for the regular lattice presented above, will sharpen as Δ increases.

The Gaussian envelope diffraction model outlined here was originally suggested by Callaghan[66]. However this model has major deficiencies. In particular its description for $C(Z, \Delta)$ is inaccurate especially for short times and small n. It will generally be most accurate for values of qb close to integers, or near the diffractive peaks.

7.2.2 Pore hopping model

It has been shown by Halpin and MacGowan[67] that the flaws in the Gaussian envelope model for $C(Z, \Delta)$ can easily be corrected by using a hopping model based on a short time τ such that a molecule has only a finite probability of "jumping" to a nearest neighbour pore and no further. One can then define a $C(Z, \tau)$ function that incorporates both the hopping envelope and the lattice function $L(Z)$ where

$$F(q, \tau) = \mathcal{F}[C(Z, \tau)]. \tag{7.12}$$

The final outcome of M independent, successive, identically distributed, random hops is represented by a M convolutions of $C(Z, \tau)$. By utilising the fact that the Fourier transform of a convolution of functions is a multiplication of the individually transformed functions one finds

$$F(q, M\tau) = \mathcal{F}[(C(Z, \tau) \otimes C(Z, \tau) \otimes \cdots)_{M\text{times}}] = (\mathcal{F}[C(Z, \tau)])^M \tag{7.13}$$

which implies

$$F(q, M\tau) = [F(q, \tau)]^M \tag{7.14}$$

Expressions can therefore be obtained by evaluating the function only for the simple case of $M = 1$. The long range diffusion coefficient can be incorporated by noting that in the low q limit $E(q, \Delta)$ gives $\exp[-2\pi^2 q^2 \langle Z^2(\Delta) \rangle]$. Hence

$$\langle Z^2(\Delta) \rangle = -\frac{1}{4\pi^2} F''(q = 0, M\tau) = 2D_{\text{eff}} \Delta \tag{7.15}$$

where the double prime denotes the second derivative with respect to q. The echo attenuation function, from eqn (7.3) is therefore

$$E(q) = |S_0(q)|^2 F(q, \Delta) \tag{7.16}$$

assuming identical pores.

7.2.3 Regular lattice

For the regular lattice, a molecule can hop left or right by the pore spacing distance, b. If τ is small enough that the molecule has only a small finite chance, w, of hopping only to a nearest neighbour pore and no further, one can write

$$C(Z, \tau) = (1 - w)\delta(Z) + \frac{1}{2}w[\delta(Z - b) + \delta(Z + b)] \tag{7.17}$$

as shown in Figure 7.1a. Using eqn (7.13) and eqn (7.17) yields

$$\begin{aligned} F(q, M\tau) &= [1 - 2w \sin^2(\pi q b)]^M \tag{7.18} \\ &= \exp[-2Mw \sin^2(\pi q b)]. \tag{7.19} \end{aligned}$$

Using the technique outlined in eqn (7.15) one finds

$$Mwb^2 = 2D_{\text{eff}} \Delta \tag{7.20}$$

and substituting into eqn (7.19) gives

$$F(q, \Delta) = \exp\left[-\frac{4D_{\text{eff}} \Delta}{b^2} \sin^2(\pi q b)\right] \tag{7.21}$$

Figure 7.2a shows the echo attenuation function for the regular lattice for various values of Δ.

Irregular lattice

Whilst considering structure associated with the displacement of probe molecules, we must take into account "correlation regularity". Suppose there is an average pore spacing b, but that there is some irregularity in that spacing ξ. As a molecule successively moves to neighbouring pores, and then next neighbouring pores, the fluctuations in spacings successively add in the the total displacement of the molecule. It is apparent then that the greatest coherence will be observed when Δ is at a time such that the molecules diffuse on average only one lattice spacing.

For an irregularly spaced lattice a suitable lattice function can be formed by convolving a Gaussian with the neighbouring lattice sites. Although this is an
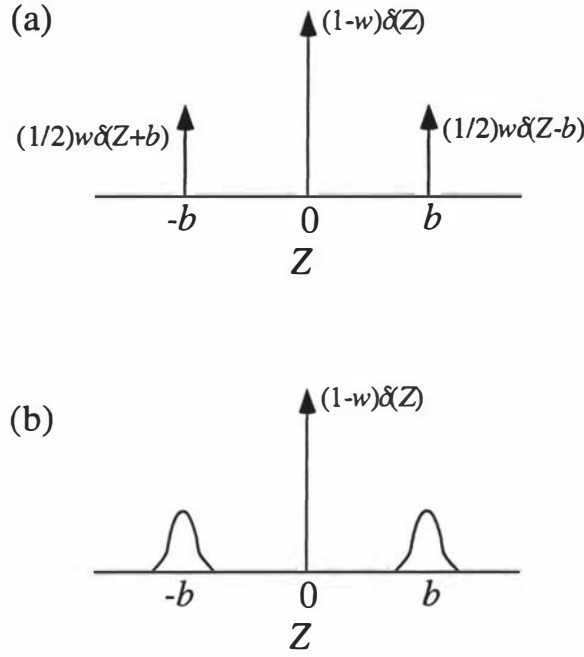
Figure 7.1: (a) The function $C(Z, \tau)$ for a regular lattice as given in eqn (7.17). (b) $C(Z, \tau)$ for an irregular one-dimensional lattice as given by eqn (7.22)

excellent first approximation of any randomness in the pore array one must consider the possibility that the probability of hopping w may vary with b in which case this function may need adjusting. An initial approximation for such an adjustment may be a b^{-1} weighting for w, however such refinements are not necessary in the experimental analysis and hence are not expanded on here.

One can therefore write

$$C(Z,\tau) = (1-w)\delta(Z) + (2\pi\xi^2)^{-1/2}\exp[-\frac{Z^2}{2\xi^2}] \otimes \frac{1}{2}w[\delta(Z-b)+\delta(Z+b)] \quad (7.22)$$

as shown in Figure 7.1b. Upon Fourier transformation this expression one gets

$$
\begin{aligned}
F(q, M\tau) &= [1 - w[1 - \exp(-2\pi^2 q^2 \xi^2)\cos(2\pi q b)]]^M & (7.23)\\
&= \exp[-Mw[1 - \exp(-2\pi^2 q^2 \xi^2)\cos(2\pi q b)]]. & (7.24)
\end{aligned}
$$

Using eqn (7.15) yields

$$Mw(b^2 + 3\xi^2) = 2D_{\text{eff}}\Delta \quad (7.25)$$

and hence

$$F(q, \Delta) = \exp\left[-\frac{2D_{\text{eff}}\Delta}{b^2 + 3\xi^2}\left(1 - \exp(2\pi^2 q^2 \xi^2)\cos(2\pi q b)\right)\right] \quad (7.26)$$

Figure 7.2b shows the echo attenuation function for an irregular lattice for various values of Δ. Notice the diffraction peak at $qb = 1$ which is most pronounced for the time $\Delta \simeq b^2/2D_{\text{eff}}$, the time taken to diffuse to the nearest neighbour pore. As Δ increases further the diffraction peak becomes more attenuated due to the irregularity in the lattice function which increases as more distant pores are probed by the diffusing molecules.

Figure 7.2: (a)The echo attenuation function for a regular lattice given by eqn (7.21) with the spherical pore expression of eqn (4.17) used for $|S_0(q)|^2$. The pore size a is fixed at $b/3$. The lines represent increasing times Δ, for increasing attenuation, with values as a fraction of $b^2/2D_{\mathrm{eff}}$ of 0.2, 0.5, 1.0 and 2.0 respectively. Notice the large coherence peak at $qb = 1$. (b) The echo attenuation function for an irregular lattice given by eqn (7.26). The parameters are as for (a) but with a pore spacing irregularity $\xi = b/3$. Notice the damping of the coherence peak and the shift of the peak to lower q values.
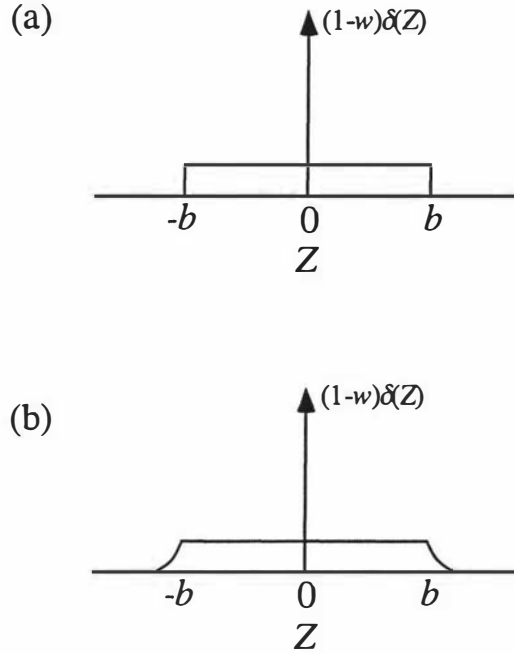
Figure 7.3: (a) The function $C(Z, \tau)$ for a pore glass lattice as given in eqn (7.27). (b) $C(Z, \tau)$ for an irregular pore glass as given by eqn (7.32).

7.2.4 Pore glass

In a pore glass the neighbouring pores are uniformly distributed in solid angle around the starting pore with some spacing b. In consequence the projection onto the z axis gives a Hat function $H(Z, b)$ which has a value $(2b)^{-1}$ for $-b < Z < b$ and zero elsewhere.

Therefore

$$C(Z, \tau) = (1 - w)\delta(Z) + wH(Z, b) \tag{7.27}$$

as shown in Figure 7.3a, which upon Fourier transformation yields

$$F(q, M\tau) = [1 - w(1 - \text{sinc}(2\pi qb))]^M \tag{7.28}$$
$$= \exp[-Mw(1 - \text{sinc}(2\pi qb))] \tag{7.29}$$

Using eqn (7.15) one gets

$$Mwb^2 = 6D_{\text{eff}}\Delta \tag{7.30}$$

and substituting into eqn (7.29) gives

$$F(q, \Delta) = \exp\left[-\frac{6D_{\text{eff}}\Delta}{b^2}\left(1 - \frac{\sin(2\pi qb)}{(2\pi qb)}\right)\right] \tag{7.31}$$

Figure 7.4a shows the echo attenuation function for a pore glass lattice for various values of Δ. The diffraction peak at $qb = 1$ which is most pronounced for the time $\Delta \simeq b^2 D_{\text{eff}}$, the time taken to diffuse to the nearest neighbour pore, although it is less pronounced than the peak for a regular lattice. As Δ increases the diffraction peak becomes more attenuated, but more pronounced, due to the glassy nature of the lattice function. The coherence peak for the pore glass is significantly more attenuated than the peak for a regular lattice.
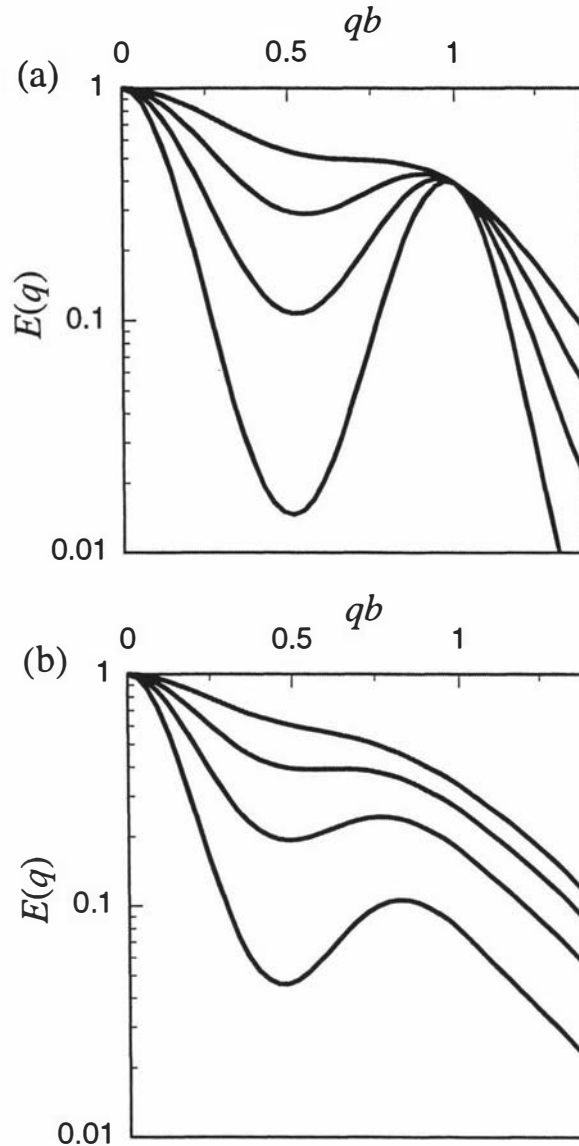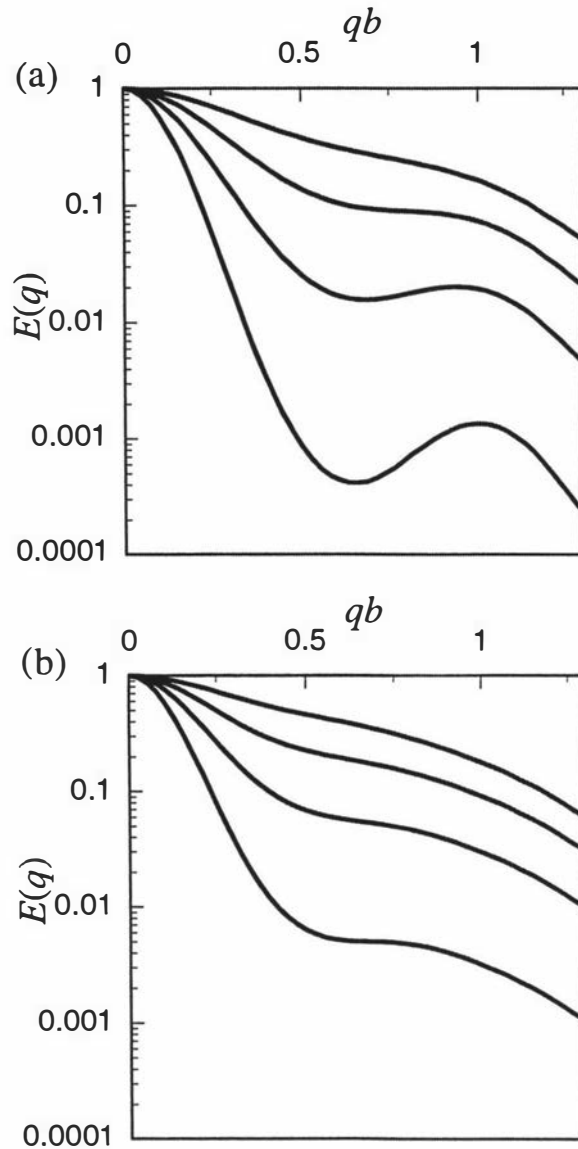
Figure 7.4: (a)The echo attenuation function for a pore glass lattice given by eqn (7.31) with the spherical pore expression of eqn (4.17) used for $|S_0(q)|^2$. The pore size a is fixed at $b/3$. The lines represent increasing times Δ, for increasing attenuation, with values as a fraction of $b^2/2D_{\text{eff}}$ of 0.2, 0.5, 1.0 and 2.0 respectively. Notice the coherence peak at $qb = 1$. (b) The echo attenuation function for an irregular pore glass lattice given by eqn (7.33). The parameters are as for a but with (a) pore spacing irregularity $\xi = b/3$. Notice the damping of the coherence peak and the shift of the peak to lower q values. Note that in both graphs the echo attenuation axis covers a greater range than for the regular lattice plots shown in Figure 7.2.

Irregularity in pore glass

Any irregularity in a pore glass will cause a spread in Z, greatest at the edges where $Z = \pm b$ and least at $Z = 0$ since any variation in b is projected along the Z-axis. However, the flatness of $H(Z, b)$ means that the effect of convolution with a Gaussian will be most apparent at the edges provided $\xi < b$. Again any pore spacing dependance of w may need to be considered in extending this theory.

For the irregular pore glass the convolution gives

$$C(Z, \tau) = (1 - w)\delta(Z) + w[(2\pi\xi^2)^{-1/2}\exp[-\frac{Z^2}{2\xi^2}] \otimes (H(Z, b)] \tag{7.32}$$

as shown in Figure 7.3b, which yields

$$F(q, \Delta) = \exp\left[-\frac{6D_{\text{eff}}\Delta}{b^2 + 3\xi^2}\left(1 - \exp(-2\pi^2q^2\xi^2)\frac{\sin(2\pi qb)}{2\pi qb}\right)\right] \tag{7.33}$$

with the appropriate factors included.

Figure 7.4b shows the echo attenuation function for an irregular pore glass lattice for various values of Δ. The diffraction peak at $qb = 1$ which is most pronounced for the time $\Delta \simeq b^2 D_{\text{eff}}$, although considerably less pronounced than for either the regular lattice or pore glass. As Δ increases the diffraction peak becomes more attenuated and shifted to lower q due to the glassy nature of the lattice function and the irregularity in pore spacing.

7.3 Computer simulations

Computer simulations of diffusion in porous media were performed by MacGowan as part of our collaboration with B.P. Research, Sunbury-on-Thames, UK[68, 67]. These simulations were useful in revealing the strengths and weakness of the pore hopping model.

7.3.1 Method

The method is detailed in our joint paper[67] and followed the usual random-walk simulation techniques. Similar problems were encountered for a finite hopping lattice method, as the ones already outlined in Section 6.3. The solution used, in this case, involved a two-dimensional model where the particle steps were of a fixed length but allowed to be in a random, continuously distributed direction. Within a few step intervals the simulated particle displacement approached the proper Gaussian form and reduced problems due to discretization of the displacement.

7.3.2 Results for regular lattice

These simulations revealed that for the regular lattice the analytic theory fitted the computer data well. They also showed that D_{eff} approached its asymptotic value in a very short time lending good support to the pore equilibration assumption. However, some error was noted for model pore systems with small pores and long interconnecting channels. This error resulted from the finite number of molecules residing in the interconnecting channels between pores and is not accounted for by the pore hopping model. In fact the analytic theory assumes the molecules hop to

a neighbouring pore instantaneously and spend no time in pore connections. The error is small and only obvious for half integer values of qb where the pore-to-channel volume ratio is above 0.5.

Lattice with disorder

For the pore models with disorder the results suggested that the analytic theory of eqn (7.26)was at least qualitatively correct. Unfortunately the model was restricted to 10 different pore spacings and so could not accurately represent a Gaussian distribution of pore spacings well.

7.4   Experiments on polystyrene spheres

In order to perform PGSE experiments on porous systems, a suitable sample had to be found. A one dimensional porous system would be ideal due to the large diffraction peaks predicted by the theory. However, in practice, we could find few samples that would fit the relevant criteria. Plane laminar surfactant bi-layers were considered, as water diffusion though the sheets would be greatly reduced compared to diffusion between the sheets. However, the spacing between sheets cannot be made stable above 50 nm, too small to observe diffraction effects with current gradient strengths. Fortunately a suitable pore glass system was found in the form of monodisperse polystyrene spheres. By packing the spheres into a close packed array the intersphere spaces would appear as a three dimensional porous lattice to interpenetrating water in the sample. These micron sized spheres, manufactured by Duke Scientific, are available as a dilute solution in water and have a surfactant coating to reduce surface effects. The spheres are characterised on the data sheets using microscope and light scattering techniques, yielding average sphere size and distribution of sphere sizes to a high precision.

7.4.1   Theoretical considerations

For an orientationally disordered pore glass with pore spacing b, the echo attenuation function from pore hopping theory in given by eqn (7.33). A coherence peak in the echo attenuation data is predicted by eqn (7.33) when qb is integer. The coherence peak is also most pronounced if $\Delta \approx b^2/2D_{\text{eff}}$ such that molecular diffusion of one pore spacing is favoured. Over longer times more molecules will diffuse to second and third neighbouring pore shells for which no integer pore spacing relation exists, leading to an increased damping of the coherence peak. Of course the variation ξ in the pore spacing also leads to further damping of the coherence maxima and in extreme cases of polydispersity no coherence peak would be visible. However even in such extreme cases there would still be anomalies in the q-space dependence of the echo attenuation data.

It should be noted that eqn (7.33) involves two approximations. Firstly, the Gaussian distribution convolution in the pore spacing is applied directly along the Z axis and not by projecting all possible orientations along the Z axis. The second assumption is that the probability of hopping is independent of the exact pore spacing, such that slightly closer pores have no greater hop probability than that of slightly more distant pores.

It is useful to consider the porous medium formed by close packing of spheres. L.C. Graton and H.J. Fraser[69] have given a detailed analysis of possible geometries. They show that there are six different symmetrical structures possible based on cubic and rhombohedral packing labelled Case I to Case VI. Of the six structures, two pairs are rotationally degenerate, leaving four intrinsically different packings with different porosities. These porosities are 47.6 % (Case I), 39.5 % (Case II and Case IV), 30.2 % (Case V) and 26.0 % (Case III and Case VI). The unit cell for each case is a six faced parallelepiped with a total occupied volume of one sphere and a sphere center at each corner. The distance between the pore centers is b, the sphere diameter.

Fitting the data

To fit the data to the pore hopping theory some function must be assigned for $|S_0(q)|^2$, the pore structure function. The real pore shapes for the voids in close packed sphere arrays are highly complicated and unlikely to be amenable to an analytic representation. However it is possible to numerically simulate the pores and with the orientation averaging necessary in such a glassy structure it is likely that the pore sizes will be comparable in each of the four different cases described by Graton and Frazer[69]. We chose to investigate the structure functions for the two limiting cases of porosity and compare them to the spherical pore structure function[70].

Non-spherical pores

Using a simple computer program a three dimensional regular array of points was reduced to the required unit void by removing all points that lay inside the spheres bounding the void. By knowing the position of the center of each sphere the program checks to see if the distance from each point to each sphere center is less than the radius of the sphere and then removes the point from the array if this condition is true. A second program then takes the three dimensional data and calculates the one dimensional radial density distribution function of the points starting from the center of the unit void. The radial density function for Case I is shown in Figure 7.5.

This radial function is then spherically averaged and projected onto an axis to represent the arbitrary gradient direction. This is again made trivial by realising that the projection of a spherical shell onto an axis is simply a hat function with width equal to twice the radius of the shell. The distributions are shown for both Case I and VI in the upper graphs of Figure 7.6.

This spherically averaged density function is Fourier transformed and squared to reveal the single pore structure function of the unit void. Theoretical fits based on a uniform spherical pore were then done and the equivalent spherical pore radii noted.

The squared modulus Fourier transforms are shown in the bottom graphs of Figure 7.6. The lines represent non-linear least squares fits of the long time limit spherical pore structure function,

$$E_\infty(q) = |S(q)|^2 = \frac{9[(2\pi qa)\cos(2\pi qa) - \sin(2\pi qa)]^2}{(2\pi qa)^6} \tag{7.34}$$

from eqn (4.17).
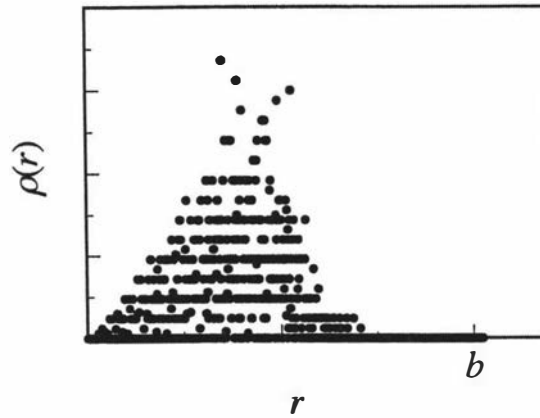
Figure 7.5: The radial density function of the unit void for the most porous cubic sphere packing (Case I). The digitization is caused by the discrete nature of the three dimensional array of points used to generate this data. The sphere diameter b is shown for reference.
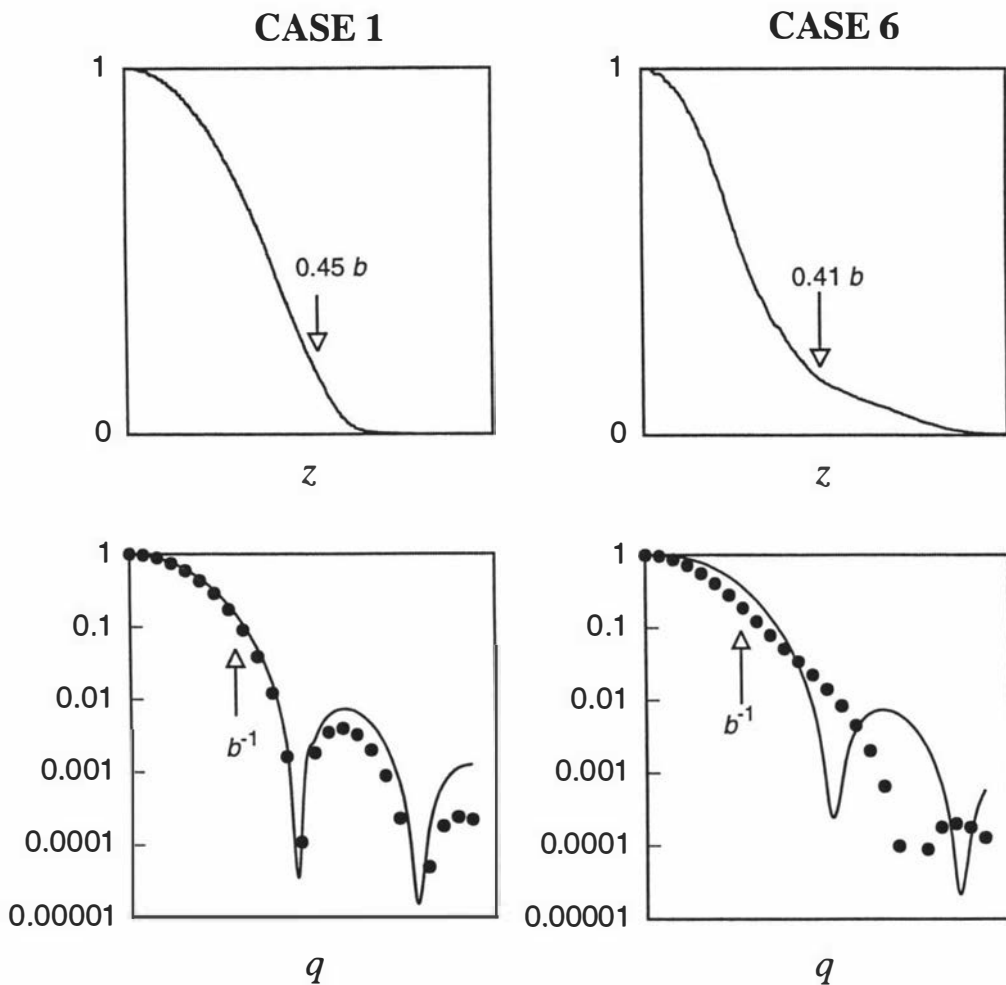
Figure 7.6: The upper two graphs show spherically averaged radial distribution functions for CASE I (cubic) and CASE VI (rhombohedral) packing. The CASE I data radial distribution function used is shown in Figure 7.5. In the lower two graphs the corresponding squared modulus Fourier spectra are shown (filled circles). The lines represent theoretical fits based on a uniform spherical pore. In each case the sphere diameter, b (or its inverse, b^{-1}), is shown for reference.

Catalog Number	Sphere diameter	Size distribution
7516A	15.8 μm	2.8 μm
241	14.6 μm	0.4 μm
4210A	9.870 μm	0.057 μm

Table 7.1: The monodisperse polystyrene spheres used in this work and their manufacturer's specifications.

For Case I a spherical pore of width 0.44b is a good representation of the pore. For the Case VI the spherical pore works moderately well for $q \leq a^{-1}$, the regime used in the PGSE experiments here. The equivalent spherical pore radii for Case VI is 0.41 b. The spherical pore structure function of eqn (7.34), is used for $|S(q)|^2$ with eqn (7.33), for all the fitting of theory to experimental data that follows.

7.4.2 Samples

All the experiments were performed on the FX-60 system using the high gradient PGSE system. The sphere solution was transferred to the 4mm O.D. sample tubes using the following technique. The sample tube was filled with some of the sphere solution and then centrifuged at 300 g for 5 minutes until the spheres formed a thin layer at the bottom of the tube. The excess water above the spheres was removed and the process repeated until the layer of closely packed spheres was around 5–10 mm in height. In this way the porous sample would completely fill the space contained by the probe r.f. coil. By comparing the NMR signal strength from a sample of only water, and the water from within the porous sphere system, the porosity was estimated at 44%.

Three samples were investigated each with a different sphere diameter. The details for each sample are shown in Table 7.1. The pore size distributions for the samples expressed as percentages are 18 %, 2.7 % and 0.0058 % for the 15.8 μm , 14.6 μm and 9.870 μm sphere systems respectively. In this way the effects of both changes in pore spacing and disorder in pore spacing could be investigated.

The T_1 and T_2 relaxation times of the water in the sample were of the order of 1 s. This implies that there was no significant relaxation effects occurring on the surface of the spheres. The samples were maintained at an ambient temperature of 28 °C. Extensive signal averaging was required as data down to attenuations of 0.001 were acquired. By using 2^N averaging acquisitions the normalisation of the signal was simplified. N was chosen so that the signal-to-noise ratio of each data point was kept reasonably constant. For high q data points up to 8192 averages were made in contrast to around 64 for the low q data. Such considerations of sensitivity were found essential if the weak coherence effects are to be observed.

The equilibration time $a^2/2D_0$ is around 3 ms for the pores formed by the spheres. The interpore diffusion time $b^2/2D_{\text{eff}}$ around 50 ms. The gradient used was 1.21 Tm^{-1} and the gradient pulse duration, δ was increased in steps of 0.1 ms. The maximum duration for δ was 1.8 ms implying that the narrow pulse approximation is valid for the interpore diffusion, However it is borderline for the intrapore diffusion.

Figure 7.7: Echo attenuation function $E(q)$ as a function of q for the 9.870 μm polystyrene sphere system. The times Δ are 10 ms (open circles), 20 ms (filled circles), 30 ms (open squares), and 40 ms (filled squares). The solid lines represent fits using eqn (7.33), the parameters for which are given in Table 7.2.

7.4.3   Results

In each PGSE experiment presented here the observation time Δ is held constant whilst the gradient duration δ is varied. As the optimal time to observe the coherence peak in a pore glass is given by $b^2/2D_{eff}$ values of Δ were chosen accordingly.

9.870 μm data

For the 9.870 μm polystyrene spheres the values of Δ were 10 ms, 20 ms, 30 ms and 40 ms. From the low q data we find $D_{eff} \approx 2.0 \times 10^{-9}$ m^{2}s^{-1} so that the time $b^2/2D_{eff}$ is 24 ms. As a fraction of this time, the observation times are then 0.4, 0.8, 1.3 and 1.7 respectively. Figure 7.7 shows the results of the PGSE experiments carried out on this system. A clearly visible coherence peak is apparent when $q \sim b^{-1}$ (100000 m^1 or 10 μm^{-1} and the observation time Δ is large enough that enough molecules have diffused from their starting pore to the nearest neighbour pore shell.

Note that even for this highly monodisperse system the coherence peak is only visible at echo attenuations of 0.01 and greater. Signal averaging of up to 4096 (2^{12}) individual FIDs was required for the high q data.

14.6 μm data

For the 14.6 μm polystyrene spheres the values of Δ were 20 ms, 40 ms, 60 ms and 80 ms. From the low q data we find $D_{eff} \approx 2.0 \times 10^{-9}$ m^2 s^{-1} so that the time $b^2/2D_{eff}$ is 53 ms. As a fraction of this time, the observation times are then 0.4, 0.8, 1.1 and 1.5 respectively. Figure 7.8 shows the results of the PGSE experiments carried out on this system. A clearly visible coherence peak is apparent when $q \sim b^{-1}$ (67000 m^{-1} or 15 μm^{-1}) and the observation time Δ is large enough that enough molecules have diffused from their starting pore to the nearest neighbour pore shell.

The fitting of eqn (7.33) to the PGSE data shown above was done using a non-linear least squares fitting routine in the program PGSEPLOT. The fitting function
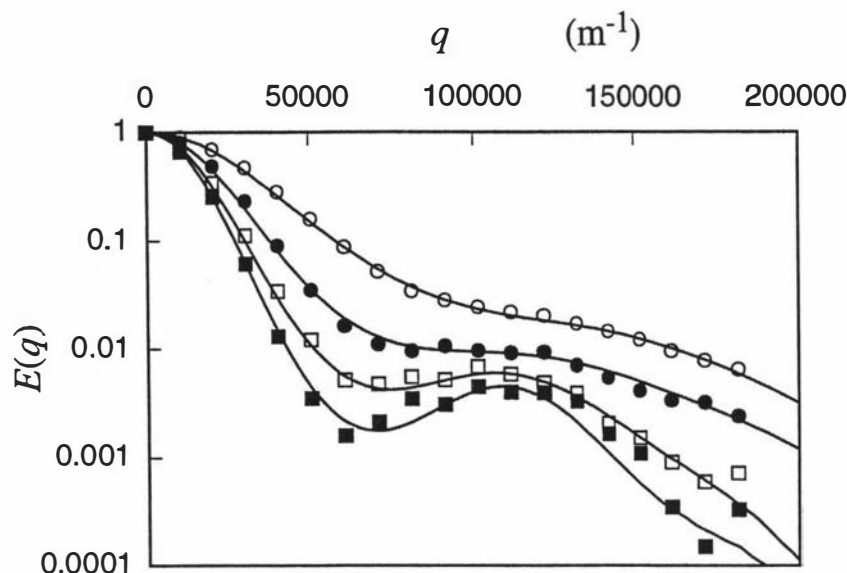
Figure 7.8: Echo attenuation function $E(q)$ as a function of q for the 14.6 μm polystyrene sphere system. The times Δ are 20 ms (open circles), 40 ms (filled circles), 60 ms (open squares), and 80 ms (filled squares). The solid lines represent fits using eqn (7.33), the parameters for which are given in Table 7.3.

Observation time Δ	Parameter				
	a	b	ξ	D_{eff}	D_{eff} low q
10 ms	2.7 μm	6.2 μm	1.9 μm	2.4×10^{-9} m^{2}s^{-1}	2.0×10^{-9} m^{2}s^{-1}
20 ms	2.7 μm	7.9 μm	2.5 μm	2.6×10^{-9} m^{2}s^{-1}	2.0×10^{-9} m^{2}s^{-1}
30 ms	3.2 μm	10.0 μm	1.5 μm	2.5×10^{-9} m^{2}s^{-1}	2.0×10^{-9} m^{2}s^{-1}
40 ms	3.3 μm	10.6 μm	0.1 μm	2.3×10^{-9} m^{2}s^{-1}	2.0×10^{-9} m^{2}s^{-1}

Table 7.2: Parameters obtained by fitting eqn (7.33) to the 9.870 μm data shown in Figure 7.7. D_{eff} low q is obtained by fitting a straight line to the low q data in a Stejskal-Tanner plot. The pore radius, a, is obtained from the spherical boundary function eqn (7.34) used for $|S_0(q)|^2$ with eqn (7.33).

used eqn (7.34) for $|S_0(q)|^2$. This fitting process yields the parameters a, b, ξ and D_{eff} which are shown in Table 7.2 for the 9.870 μm system and Table 7.3 for the 14.6 μm system.

Inspection of the fit parameters reveals some discrepancy as the observation time is increased. The most significant trend is the increase in pore spacing, b, as Δ is increased. A possible explanation for this is the assumption, in pore hopping theory, that the hop probability is independent of the pore separation. In the event of pore spacing distribution it is more likely that closer pores will be accessed at shorter observation times. As Δ is increased, more of the longer distance pores will be "hopped" to and the apparent b will increase. However, in spite of this weak dependence of b on Δ it is clear that the fits of the theory to the data give good estimates of the pore spacing close to the known diameters of the spheres. It is also apparent from inspection of Figure 7.7 that the fitted lines agree well with the shape of the data in q-space. In fact the position of the clearly distinguished coherence

Observation time	Parameter				
Δ	a	b	ξ	D_{eff}	D_{eff} low q
20 ms	5.0 μm	10.7 μm	0.0 μm	2.4×10^{-9} m^{2}s^{-1}	2.0×10^{-9} m^{2}s^{-1}
40 ms	5.7 μm	13.7 μm	0.0 μm	2.6×10^{-9} m^{2}s^{-1}	2.1×10^{-9} m^{2}s^{-1}
60 ms	5.0 μm	14.9 μm	1.5 μm	2.7×10^{-9} m^{2}s^{-1}	2.0×10^{-9} m^{2}s^{-1}
80 ms	4.7 μm	16.1 μm	1.3 μm	2.7×10^{-9} m^{2}s^{-1}	2.1×10^{-9} m^{2}s^{-1}

Table 7.3: Parameters obtained by fitting eqn (7.33) to the 14.6 μm data shown in Figure 7.8. D_{eff} low q is obtained by fitting a straight line to the low q data in a Stejskal-Tanner plot. The pore radius, a, is obtained from the spherical boundary function eqn (7.34) used for $|S_0(q)|^2$ with eqn (7.33).

peak in q-space defines b^{-1}, whatever the assumptions underlying the theoretical model used. For this reason any adjustment of fitting parameters to account for discrepancies between theory and data, must be made in the remaining parameters.

The fitted parameter D_{eff} was found to be significantly higher than the expected value for all the data. By taking the low q data and plotting it on a Stejskal-Tanner plot it was found to give a D_{eff} of 2.0×10^{-9} m^2 s^{-1}. These anomalies in D_{eff} have been observed in fitting pore hopping theory to the computer simulations[67]. A likely source of error is the assumption in the pore hopping theory that probability of occupancy changes discretely from pore to pore. It is more likely that pore occupancy changes discontinuously within pore connections. However it seems that this discrepancy, which depends upon the degree of porosity, does not appear to influence the fit of b, the pore separation.

A further discrepancy between the fitted lines and the raw data is apparent at high q values where the echo attenuation data is slightly higher than the theoretical fits. This is due to the sharp null at $q = a^{-1}$ in the spherical pore structure function used in the fitting equation. The more realistic pore structure functions shown in Figure 7.6 do not have a strong minimum and are more consistent with the data in the high q region. From the fitted parameters we find the fitted structure function yields an equivalent spherical pore radius of approximately $0.33b$. This is smaller than the equivalent pore radii of $0.44b$ and $0.41b$ determined for Case I and Case VI respectively. This discrepancy could be attributed to the non-linear nature of the averaging process involved in determining a mean structure factor for the very non-spherical pores. Another consideration is the openness of the porous structure given the pore equilibration assumptions underlying pore hopping theory. It is also possible that the same defects that caused D_{eff} to be overestimated may lead to a distortion in the apparent pore size. Despite these reservations, the values of a obtained in the fits are broadly consistent with the known pore dimensions.

15.8 μm data

For the 15.8 μm polystyrene spheres the values of Δ were 20 ms, 40 ms, 70 ms and 110 ms. From the low q data we find $D_{\text{eff}} \approx 2 \times 10^{-9}$ m^2 s^{-1} so that the time $b^2/2D_{\text{eff}}$ is 62 ms. As a fraction of this time, the observation times are then 0.32, 0.65, 1.12
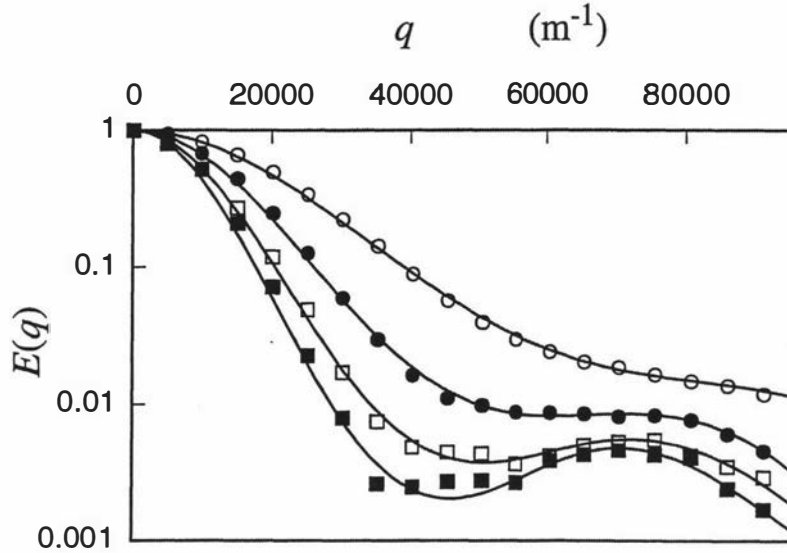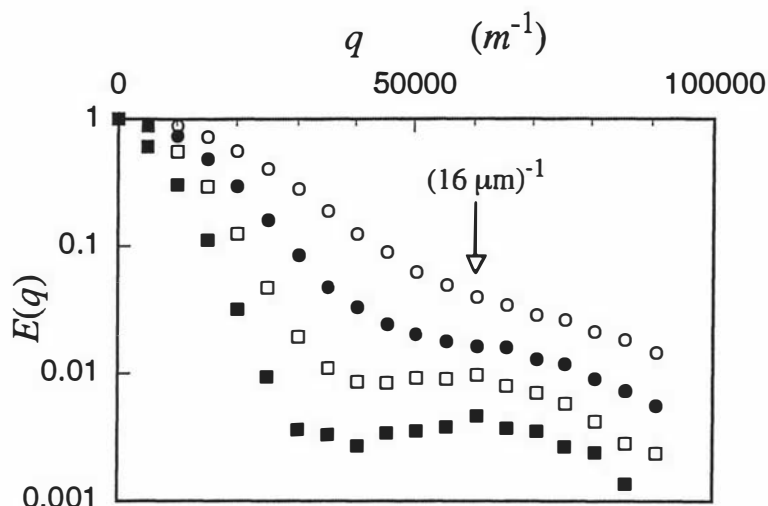
Figure 7.9: Echo attenuation function $E(q)$ as a function of q for the 15.8 μm polystyrene sphere system. The times Δ are 20 ms (open circles), 40 ms (filled circles), 70 ms (open squares), and 110 ms (filled squares). The reciprocal lattice spacing, b^{-1}, is indicated on the graph.

and 1.77 respectively. The data are shown in Figure 7.9.

Inverse Fourier transformation of echo attenuation data will give the averaged propagator. Assuming the system is isotropic, a three-dimensional projection reconstruction can be used to produce an 'image'. For the polystyrene sphere array this 'image' will be the spherically averaged autocorrelation function for the pores convolved with the diffusion-weighted three-dimensional lattice correlation function (as opposed to the projection, $L(Z)$, of this function along a single axis. Figure 7.10 shows a slice through the center of this 'image' along with a reference distance for the 110 ms data of the 15.8 μm sphere system.

Figure 7.11 shows fits to the data for each of the three samples under conditions
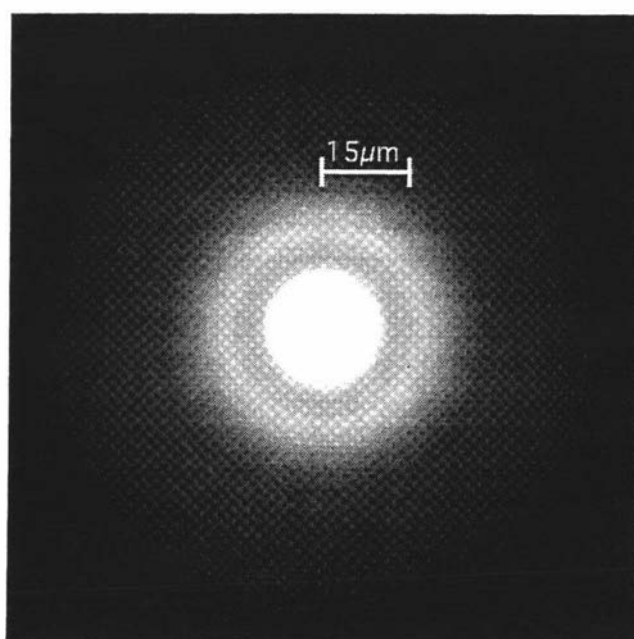
Figure 7.10: 'Image' of the pore autocorrelation function convoluted with the diffusion-weighted three-dimensional lattice correlation function. The 'image' was obtained by Fourier transformation of the 15.8 μm, 100 ms data.
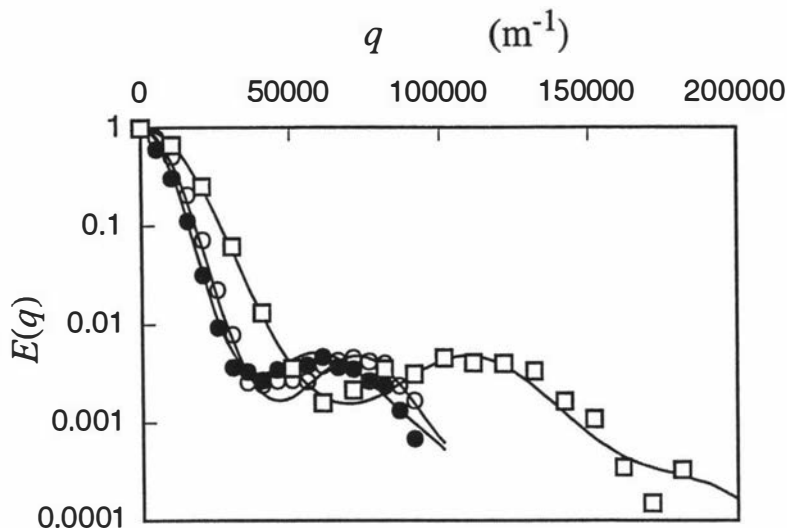
Figure 7.11: Echo attenuation function $E(q)$ as a function of q for water diffusing in the 15.8 μm (filled circles), 14.6 (open circles) and 9.870 μm (open squares) polystyrene sphere systems. The solid lines represent fits using eqn (7.33), with the parameters shown in Table 7.4.

Sphere			Parameter		
Diameter	Δ	a	b	ξ	D_{eff}
15.8 μm	110 ms	5.3 μm	18.5 μm	2.8 μm	2.6×10^{-9} m^{2}s^{-1}
14.6 μm	80 ms	4.7 μm	16.1 μm	1.3 μm	2.6×10^{-9} m^{2}s^{-1}
9.870 μm	40 ms	3.0 μm	10.7 μm	0.1 μm	2.4×10^{-9} m^{2}s^{-1}

Table 7.4: Parameters for fits to data from the three different polystyrene sphere systems shown in Figure 7.11 using eqn (7.33) and eqn (7.34). The parameters may be compared with the manufacturers' values given in Table 7.1.

where Δ was such that most molecules had diffused to a neighbouring pore and the coherence peak was most pronounced. The fitted b and ξ parameters from Table 7.4 agree well with manufacturers specifications. The graph shows clearly that the coherence peak for each data set occurs at a different value of q consistent with the reciprocal lattice distance of the differing pore spacings. The consistency of the pore distance variation parameter ξ with monodispersity can also be investigated. Comparing the fitted values with the manufacturer's specifications in Table 7.1 reveals surprisingly good consistency. This is also evident in the echo attenuation data where the coherence peak for the more monodisperse 9.870 μm system is far more pronounced than the weak peak barely visible in the less uniform 15.8 μm system. In fact the peak for the 9.870 μm spheres is the most pronounced coherence peak we have observed to date, corresponding to a difference between the peak maximum and dip minimum by a factor of over 2.5.

7.5 ESR experiments

A good example of the use of the PGSE theory presented in this thesis is from experiments performed to measure the restricted diffusion of electrons along fluoranthene channels in the quasi-one-dimensional organic conductor $(FA)_2PF_6$[71, 72]. While the PGSE ESR experiments described here were carried out by Callaghan and Kaplan, I carried out the data fitting, using the various restricted diffusion models, as part of this thesis. The key features of this sample are the relatively long relaxation times of the electrons, $T_2^* \approx 6\mu s$, and extreme anisotropy of the electron motion. Steady gradient studies[73] have shown the diffusion parallel to the conducting channels is about 1.8×10^{-4} m^2 s^{-1} whereas diffusion perpendicular to the channels is at least three orders of magnitude smaller.

7.5.1 Apparatus and experiments

The fringe field outside a 7.0 T NMR cryomagnet was used to provide a static field of 10.5 mT necessary to carry out ESR experiments at 300 MHz. The details of the apparatus used is described elsewhere[71].

The key features of our system was a home-built pulsed current driver based on the "clipped L-C resonance" idea of Conradi *et al.*[74] which provided gradient pulses of sufficiently short duration. Peak field gradients of up to 1.0 T m^{-1} could easily be realised with pulse durations down to 2 μs.

Experiments

PGSE experiments were performed on the samples at four fixed values for Δ, namely 10 μs, 14 μs, 16.5 μs and 19.5 μs. These values represent the time range available, limited by spectrometer recovery time and signal-to-noise considerations. For most times the experiments were performed with δ values of 2.0 μs and 4.0 μs. The gradient was aligned parallel to the conducting channels and hence measured the motion of the electrons in the fast diffusing direction.

7.5.2 PGSE theory

The electrons in this sample are assumed to be trapped in wells formed by the random inclusion of defects in the crystal structure. The distribution of well sizes is given by the density distribution $P(l) = \bar{l}^{-1}\exp(-l/\bar{l})$. The electron contribution to the echo is given by the weight function $p(l) = l\bar{l}^{-2}\exp(-l/\bar{l})$. The nature of the well defects will determine the type of model necessary to correctly represent the data. If the walls are completely reflecting the simple diffraction ideas presented in Chapter 4 can be used. The extension to PGSE, for relaxing boundaries, presented in Chapter 6 can also be incorporated. Finally the hopping ideas presented in this Chapter can be incorporated if the walls are assumed to be partially permeable.

Well size distribution

For simple reflecting barriers separated by a distance l the electron diffusion will appear to be unrestricted for $\Delta \ll l^2/2D$, but for $\Delta \gg l^2/2D$ the mean-squared

displacement will appear to be time-independent and of the order of l^2. The echo attenuation for this single pore in the long time limit is given by eqn (4.4), namely

$$E(q) = \frac{2[1 - \cos(2\pi q l)]}{(2\pi q l)^2} \tag{7.35}$$

Integrating this equation over the assumed weighted distribution function, $p(l)$, I found

$$E(q) = \frac{\log(1 + 4\pi^2 q^2 l^2)}{4\pi^2 q^2 l^2} \tag{7.36}$$

This equation is clearly an approximation since the pore equilibration condition $\Delta > l^2/2D$ must break down for the largest values of l. However, provided $\bar{l}$ is not too large, this fraction of electrons will be small and the average structure function will be useful. The low-q expression provides further insight as the mean-square displacement, $\overline{l^2}$, can be obtained from

$$E(q) = \exp(-4\pi^2 q^2 \frac{1}{12}\overline{l^2}) \tag{7.37}$$

Relaxation effects

Many of the assumptions presented above can be removed by using a more exact theory for the echo attenuation. In fact the expression in eqn (6.27) can be used which allows for finite Δ and any relaxation effects at the boundaries. The well size distribution can be incorporated by using eqn (6.27) in the integration,

$$E(q) = \int_0^\infty p(l) E_l(q) \, dl \tag{7.38}$$

where $E_l(q)$ is eqn (6.27) with a replaced by l. This complicated expression can be evaluated numerically on a computer and has also been incorporated into a non-linear least squares fitting algorithm in which the parameters $\bar{l}$ and M are varied, to best fit this theory to the PGSE data.

Well hopping

The facility to move between wells suggests that instead of being restricted to dimensions of the local well, each electron, over a sufficiently long timescale, will experience a long range mobility characterised by an effective diffusion coefficient D_{eff}. If the pore equilibration condition is to hold the the permeability of the walls must be weak so that the electrons will experience sufficient numbers of collisions so that interpore effects can be separated from the effects of motion within the well. Given two wells of length l_1 and l_2, the separation of the well centers is $X = (l_1 + l_2)/2$. The distribution of separations $h(X)$ is therefore

$$\begin{aligned}
h(X) &= 2\int_0^{2X} p(l_1) p(2X - l_1) \, dl_1 \\
&= \frac{8}{3} \frac{X^3}{\bar{l}^4} \exp(-2X/\bar{l}).
\end{aligned} \tag{7.39}$$

Using eqn (7.39) as the distribution of neighbouring well center displacements in the pore hopping formalism it can be shown that

$$E(q) = \frac{\log(1 + 4\pi^2 q^2 l^2)}{4\pi^2 q^2 l^2} \exp\left[-\frac{2D_{\text{eff}}\Delta}{5\bar{l}^2}\left(1 - \frac{1 - 6(\pi q \bar{l})^2 - (\pi q \bar{l})^4}{(1 + (\pi q \bar{l})^2)^4}\right)\right] \tag{7.40}$$
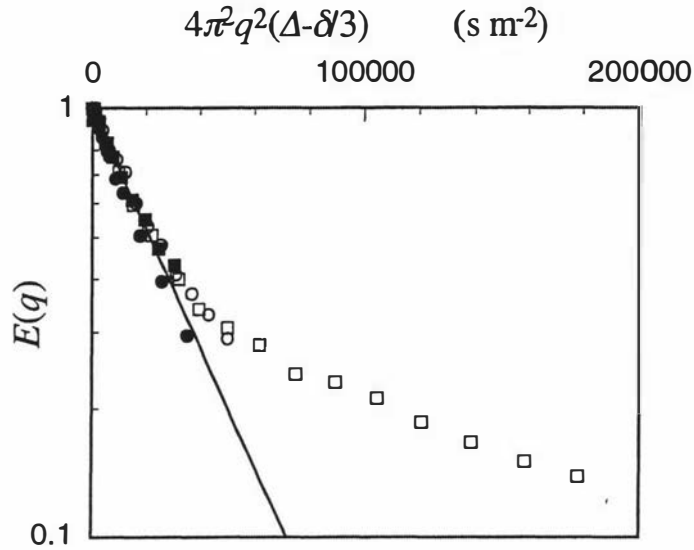
Figure 7.12: Log-linear plot of normalised echo amplitude vs $4\pi^2 q^2 \Delta_r$ (Stejskal-Tanner plot) for electron spin echoes obtained from $(FA)_2 PF_6$. The data shown are for a range of reduced diffusion times ($\Delta_r = \Delta - \delta/3$) and in each case correspond to the shortest gradient pulse duration, $\delta = 2\mu s$ for $\Delta = 10$ μs (filled circles), 14 μs (open circles) and 16.5 μs (filled squares) and to $\delta = 2.6$ μs for $\Delta = 19.5$ μs (open squares). The data deviate from the simple Gaussian expected for free diffusion with unique diffusion coefficient, D, and do not lie precisely on a common curve as Δ is varied. This latter feature is characteristic of restricted diffusion.

for the echo attenuation function using eqn (7.36) for the average structure function. This expression assumes equal well hopping probability, that is the probability of hopping is independent of the size of the wells the electron is hopping between. A reduction in hopping probability for large wells can be incorporated by altering the X^3 weighting in eqn (7.39). By changing to a quadratic variation and integrating I obtained

$$E(q) = \frac{\log(1 + 4\pi^2 q^2 l^2)}{4\pi^2 q^2 l^2} \exp\left[-\frac{D_{\text{eff}}\Delta}{\bar{l}^2}\left(1 - \frac{1 - (\pi q \bar{l})^2}{(1 + (\pi q \bar{l})^2)^2}\right)\right]. \tag{7.41}$$

Both this hopping model and the relaxing wall model presented above provide significant deviations from the simple long-time well structure function in the high-q region.

7.5.3 Results

In Figure 7.12 some of the data collected is shown on a conventional Stejskal-Tanner plot. The shortest δ data for each of the four Δ values used is shown. The low-q data can be analysed using eqn (7.37) which yields a value for $(\overline{l^2})^{1/2}$ of $80 \pm 5\mu$m. From $p(l)$ it can be shown that $(\overline{l^2})^{1/2} = \sqrt{6}\,\bar{l}$ and hence, $\bar{l} \approx 33\mu$m.

Impenetrable relaxing wall model

In fitting the data to equations (7.38) and (6.27) a least squares algorithm was used with M and $\bar{l}$ as free parameters. The parameter D was fixed at 1.8×10^{-4} m^2 s^{-1}, the value used in the previous steady gradient work[73], noting that the fits to $\bar{l}$ depend only weakly on D. Table 7.5 summarises the parameters for the fits which show an increasing trend for $\bar{l}$ settling at a value of around 50μm for the $\Delta = 16.5$ and 19.5 μs. The best overall fit was found to be with $M = 0.01$.

Figure 7.13: Echo attenuation function $E(q)$ as a function of q for electron spin echoes from $(FA)_2PF_6$ and for observation times Δ of a) 10 μs ($\delta = 2.0\ \mu s$), b) 14 μs (filled circles are $\delta = 2.0\mu s$ and open circles are $\delta = 4.0\ \mu s$), c) 16.5 μs (filled circles are $\delta = 2.0\ \mu s$, open circles are $\delta = 2.6\ \mu s$ and open squares are $\delta = 4.0\ \mu s$) and d) 19.5 μs (filled circles are $\delta = 2.6\ \mu s$ and open circles are $\delta = 4.0\ \mu s$). Also shown are the best fits using the impenetrable relaxing wall model of eqn (7.38) optimised by varying M and $\bar{l}$. The parameters for the fits are summarised in Table 7.5.

Figures 7.13a to 7.13d show the data for the four different observation times along with fitted lines from eqn (7.38). Figure 7.14 shows a set of curves for three values of Δ for which the adjustable parameters were chosen to give the best compromise fit.

Permeable wall model

The discrepancy in fitting the relaxing walls model to the data naturally leads to consideration of the permeable wall model. A least squares analysis of the data using the pore hopping model was performed, allowing the parameters $\bar{l}$ and D_{eff} to be varied. For the uniform hopping model of eqn (7.40), no good fit is obtained for which $D_{\text{eff}} > 0$. By contrast, the inverse quadratic dependence of well hopping on well separation given by eqn (7.41) does yield a consistent family of fitted curves, as shown in Figures 7.15a to 7.15d. The parameters for these fits are summarised in Table 7.6. A combined least squares fit to all the data was also performed, the result of which is shown in Figure 7.16. The value for $\bar{l}$ of 25 μm found using this model is more consistent with the 33 μm obtained using the low-q data.
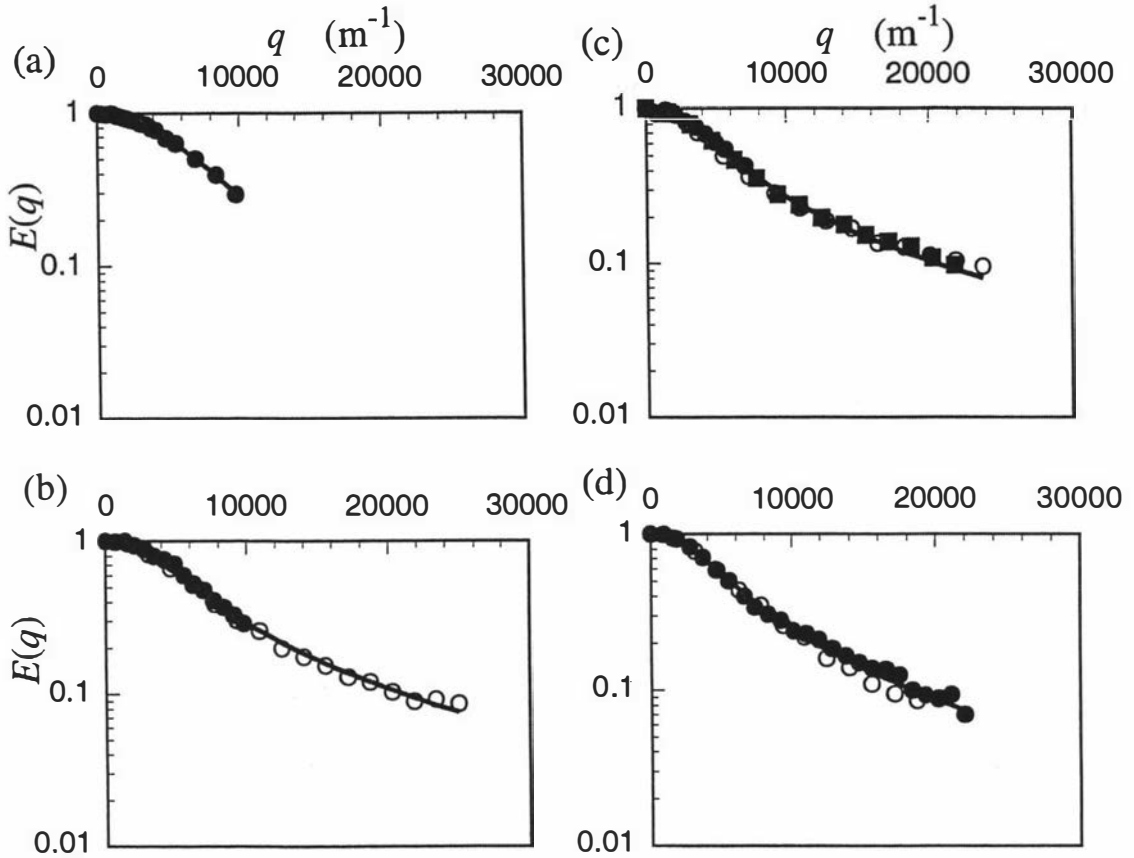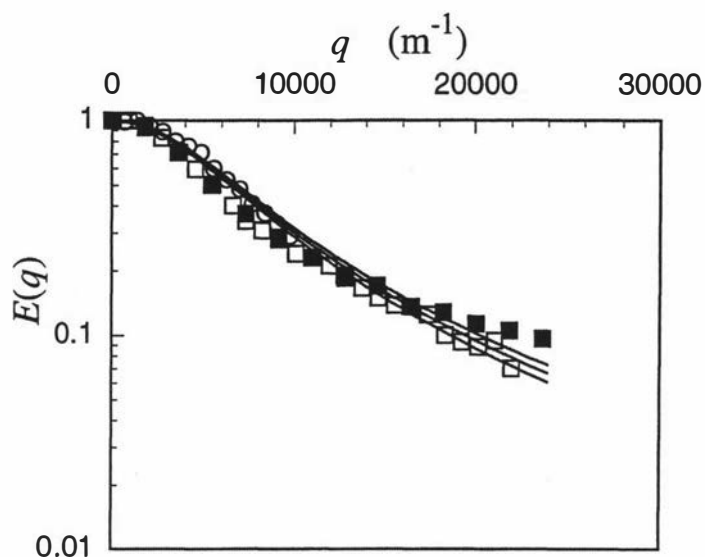
Figure 7.14: Echo attenuation function $E(q)$ as a function of q for electron spin echoes from $(FA)_2 PF_6$ and for observation times (Δ, δ) values of open circles (14.0 μs, 2.0 μs), filled squares (16.5 μs, 2.6 μs) and open squares (19.5 μs, 2.6 μs) along with a set of three curves corresponding to the compromise best fit parameter set ($D = 1.8 \times 10^{-4}$ m^2 s^{-1}, $\bar{l} = 47$ μm and $M = 0.01$) using eqn (7.38) where descending amplitude corresponds to ascending Δ.

Observation time Δ	Parameter		
	$\bar{l}$	M	D
10.0 μs	21 μm	4 m s^{-1}	1.8×10^{-4} m^2 s^{-1}
14.0 μs	20 μm	4 m s^{-1}	1.8×10^{-4} m^2 s^{-1}
16.5 μs	47 μm	0 m s^{-1}	1.8×10^{-4} m^2 s^{-1}
19.5 μs	46 μm	0.11 m s^{-1}	1.8×10^{-4} m^2 s^{-1}
compromise fit	47 μm	0.01 m s^{-1}	1.8×10^{-4} m^2 s^{-1}

Table 7.5: Parameters used in fits to the data shown in Figures 7.13 and 7.14 using the impenetrable relaxing wall model of eqn (7.38).
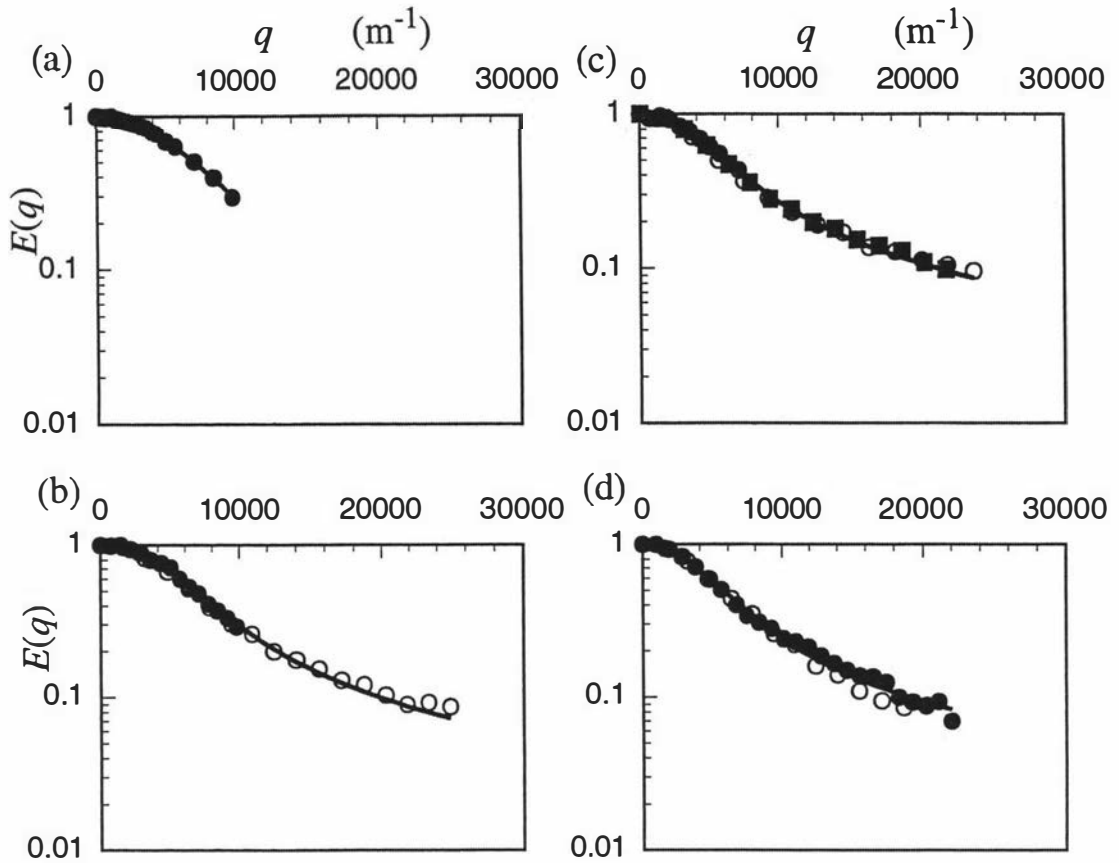
Figure 7.15: Data as for Figure 7.13 but with fits carried out using the permeable wall hopping model optimised by varying D_{eff} and $\bar{l}$. The fitted parameters are shown in Table 7.6. No good fit can be obtained using the uniform hopping rate of eqn (7.40) and the theoretical curves shown here correspond to an assumption of inverse quadratic dependence of well hopping on well separation given by eqn (7.41).
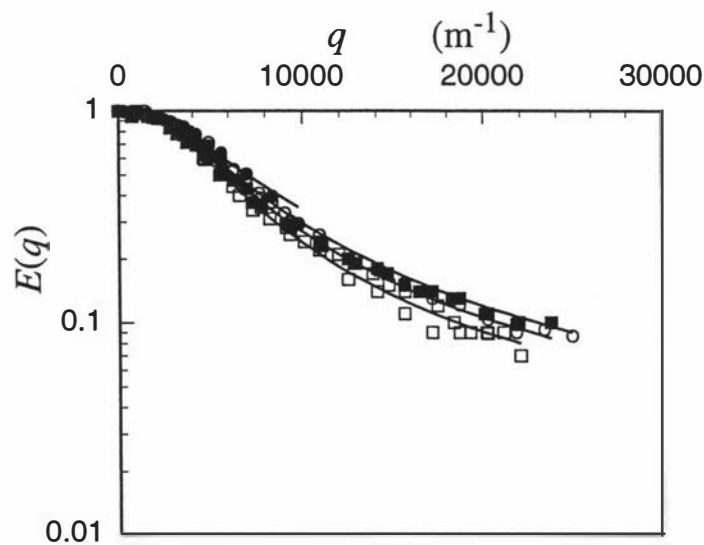
Figure 7.16: Echo attenuation function $E(q)$ as a function of q for electron spin echoes from $(FA)_2PF_6$ and for observation times (Δ, δ) values of filled circles 10 μs, 2.0 μs), open circles (14.0 μs, 2.0 μs), filled squares (16.5 μs, 2.6 μs) and open squares (19.5 μs, 2.6 μs) along with a set of four curves using eqn 7.41 corresponding to a least squares best fit to the entire data set ($D_{\text{eff}} = 2.1 \times 10^{-5}$ m^2 s^{-1}, $\bar{l} = 25$ μm) where descending amplitude corresponds to ascending Δ.

Observation time	Parameter	
Δ	$\bar{l}$	D_{eff}
10.0 μs	13 μm	3.2×10^{-5} m^2 s^{-1}
14.0 μs	20 μm	2.2×10^{-5} m^2 s^{-1}
16.5 μs	26 μm	2.1×10^{-5} m^2 s^{-1}
19.5 μs	26 μm	2.1×10^{-5} m^2 s^{-1}
best fit	25 μm	2.1×10^{-5} m^2 s^{-1}

Table 7.6: Parameters used in fits to the data shown in Figures 7.15 and 7.16 using the permeable wall model of eqn (7.41).

Inverting the data

All the models presented thus far depend specifically on the assumed exponential distribution of well sizes. In principle it is possible to transform the echo attenuation function to reveal the appropriate weight distribution function, $p(l)$, given a knowledge of the specific nature of the electron-barrier interaction. The simplest model to use is the time independent diffraction model where the averaged propagator is given by a sum of one-dimensional well autocorrelation functions. The inverse Fourier transform of the $\Delta = 19\mu$s data is shown in Figure 7.17a. This longest time was used as the model inherently assumes the long time limit approximation applies to all wells. The data is analysed to reveal a corresponding distribution function $p_{\text{eff}}(l)$, shown in Figure 7.17b, using both a non-negative least squares (NNLS) and a least distance (LDP) algorithm in which the kernel is taken to be the expected triangular autocorrelation function. The exponential weight function, $p(l)$ is also using the value $\bar{l} = 25\mu$m.

The difference in the results of the NNLS and LDP algorithms serves to emphasise the difficulties inherent in an inversion of the averaged propagator in order to find the distribution of autocorrelation functions. The direct inversion also assumes perfectly reflecting walls, no boundary relaxation and the long time limit for the trapped electrons and therefore more weight is placed on the echo attenuation data results shown above. However the analysis shown here shows the possibility of such an approach in other more well defined systems.

Two population model

Finally we have attempted to fit the data presented here with a model comprising two populations of electrons, one of weight x which is free to diffuse without restrictions with self diffusion coefficient D and one of weight $1 - x$ which is completely confined. The best fit to D and x is shown in Figure 7.18 and clearly gives a poor representation of the data.
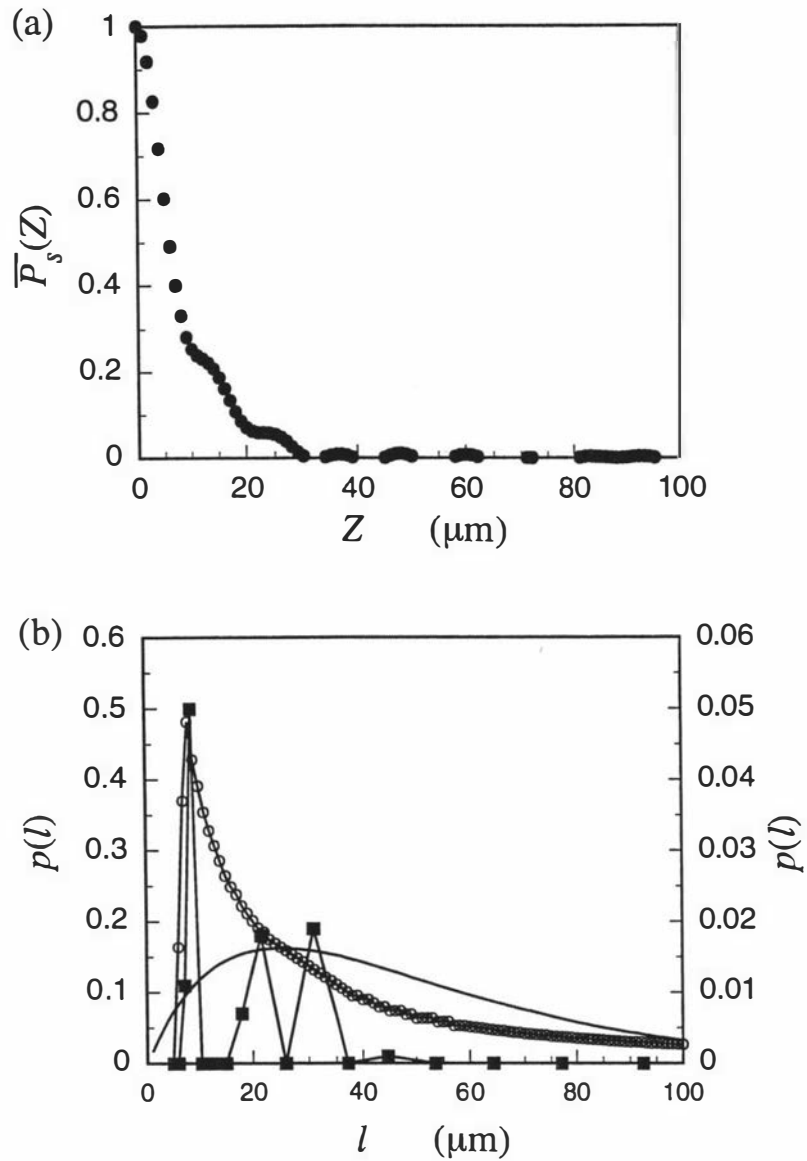
Figure 7.17: (a) The spatial Fourier transform of the $E(q)$ data for $\Delta = 19.5$ μs and $\delta = 2.6$ μs along with (b), the corresponding distribution function $p(l)$ obtained using the NNLS (filled squares), left hand scale) and LDP (open circles, right hand scale) algorithms of Lawson and Hanson in which the kernel is taken to be the expected triangular autocorrelation function. The solid curve (right hand scale) shows the exponential weight function $p(l)$, calculated using the value $\bar{l} = 25$ μm.
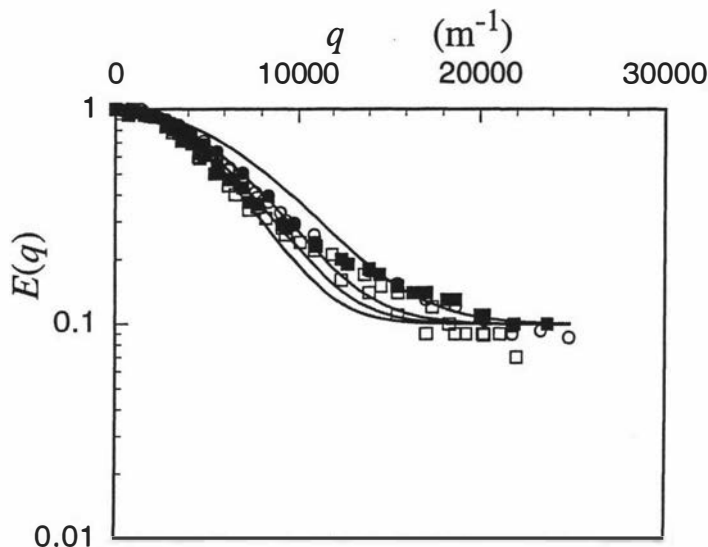
Figure 7.18: Fit to the $E(q)$ data of Figure 7.16 ($\Delta = 10, 14, 16.5$ and 19.5 μs as filled circles, open circles, filled squares and open squares respectively) using a simple two site model in which one fraction of electrons is able to diffuse freely ($D = 3 \times 10^{-5}$ m^2 s^{-1}, $x = 0.9$) while the remaining electrons are confined. Descending amplitude corresponds to ascending Δ. The data are poorly represented by such a model.

7.6   Summary

The experiments on the polystyrene sphere array clearly demonstrate the versatility and usefulness of taking a diffractive approach to PGSE NMR. Experiments performed on the polystyrene sphere array showed the coherence peak predicted at $q = b^{-1}$. These results were the first published[38] PGSE data showing an increase in echo signal strength with an *increase* in gradient strength. A similar interference effect has recently been reported in an oil-water emulsion system by Balinov *et. al*[75]. The shape of the attenuation curve was consistent with predictions of the pore glass, pore hopping model. Structural parameters pertaining to the sample were revealed[67]. Through non-linear least square fitting, the analytic theory was fitted to echo attenuation data for each time Δ. The parameters were consistent with expected results but with short times Δ giving smaller fitted values for b.

The shape of the pore voids formed by the polystyrene spheres were also analysed to test the use of the long time limit spherical pore structure function to model $|S_0(q)|^2$. The results showed a best-fit average spherical pore size of $a \sim 0.43b$, broadly consistent with the PGSE data results which found $a \sim 0.33b$[70].

I also demonstrated the usefulness of the pore hopping model outlined in this chapter, and the parallel barrier model outlined in Chapter 6, by applying them to the analysis of PGSE ESR data obtained from the conduction electrons in a $(FA)_2PF_6$ sample where the electron diffusion data clearly involved restricted diffusion. I fitted the data to two models, one based on the parallel relaxing wall model and the second on pore hopping. The pore hopping approach proved useful in finding simple, analytic expressions for $E(q)$. I wrote computer programs to fit these models to the ESR data in order to test both the consistency of the mechanism of each model in simulating the observed data, and to obtain structural parameters relevant to the system under investigation. The pore hopping model proved better at modelling the data although neither method was conclusive. The ESR data was also inverted to reveal the average propagator. The corresponding distribution func-

tion $p_{\text{eff}}(l)$ was found using two different algorithms in which the kernel was taken to be the expected triangular autocorrelation function.

In Chapter 8 the restricted diffusion exhibited by entangled polymer chains will be investigated.

Chapter 8

Dynamics of Semi-Dilute Polymer solutions

8.1 Introduction

A further example of constrained or restricted diffusion can be found when considering the motion of polymers in solution. In the semi-dilute or concentrated regimes the polymers in a solution are sufficiently packed, such that they overlap and entanglements occur. A theory of the self-motion of such entangled polymers, originally proposed by de Gennes[76], and extended by Doi and Edwards[77], has been quite successful in describing the motion of entangled polymer systems. While experiments on concentrated polymer melts, using forced Rayleigh scattering[78, 79], neutron scattering[80, 81, 82] and computer simulations[83, 84, 85, 86, 87, 88], have definitively shown that reptation is the mechanism for diffusion, the situation with semi-dilute solutions is not so convincing[89, 90].

A question that is central to understanding the dynamics of entangled polymer molecules concerns whether linear chains in semi-dilute solution reptate[89]. PGSE, along with neutron scattering, is one of the few techniques able to adequately probe the internal motions of polymers in this state, due to the ability to measure the self-motion of molecules as opposed to relative motion. The dynamic distances appropriate for polymer diffusion measurements are of the order of 50 to 5000 Å. Unfortunately neutron scattering is confined to measuring displacements of less than 50 Å while, until recently, PGSE NMR has been confined to measurements above 1000 Å displacement. Recent improvements[25, 54] to the PGSE NMR method have reduced this lower limit by an order of magnitude. One such method, the PGSE-MASSEY technique[54], is used to obtain some of the results presented here. The time window available is determined by the available gradient amplitude and by spin relaxation. In the present instance it is from 10 ms to 1 s.

This chapter introduces the theory of polymer reptation and describes some experiments performed which provide evidence for reptational motion and the entanglement tube in semi-dilute polymer solutions.

8.2 Polymers

Linear polymer chains are long, flexible snakelike molecules formed chemically by the repetition of some simple subunit known as a monomer. For example, in this

$\overline{M_p}$	$\overline{M_w}/\overline{M_n}$
3.30×10^5	1.04
5.01×10^5	1.06
7.70×10^5	1.04
1.13×10^6	1.04
1.57×10^6	1.06
1.75×10^6	1.06
3.04×10^6	1.04
1.50×10^7	1.25

Table 8.1: The high molecular weight, monodisperse polystyrene standards obtained from Polymer Laboratories (Church Stretton, Shropshire, England) used in this work.

work, polystyrene is extensively used and consists typically of between 10 and 10^5 units of the styrene monomer linked end to end.

Scaling properties

Many polymer properties depend critically on the number of monomers in the chain. In fact this leads directly to a number of scaling laws where some characteristic of the polymer, such as the self-diffusion coefficient, will scale with the number of monomers in present in the chain. However these scaling relationships depend critically on the number of monomers in the polymer, so the variation in the number of monomers in different polymer chains in a particular sample of polymer is important.

Monodispersity

The molecular mass M of a polymer, measured in daltons, is typically between 1000 and 10^7, with each monomer being around 100 daltons in mass. In reality, there is often a distribution of polymer sizes in any sample, and M is not well defined. The distribution can be characterised by the number-averaged molar mass $\overline{M_n}$ where

$$\overline{M_n} = \frac{\sum_{i=1}^{\infty} N_i M_i}{\sum_{i=1}^{\infty} N_i} \tag{8.1}$$

and the weight-averaged molar mass $\overline{M_w}$ where

$$\overline{M_w} = \frac{\sum_{i=1}^{\infty} N_i M_i^2}{\sum_{i=1}^{\infty} N_i M_i} \tag{8.2}$$

The monodispersity or width of the distribution is given by $\overline{M_w}/\overline{M_n}$ called the polydispersity index. For a perfectly monodisperse polymer $\overline{M_w}/\overline{M_n} = 1.0$. An index below 1.2 indicates good monodispersity for a sample which can then be well characterised by appropriate parameters. As the polydispersity increases above this value the averaged behaviour becomes increasingly hard to interpret[91]. The polystyrenes used here had been polymerised by anionic polymerisation, which has typical polydispersity indices between 1.04 and 1.1. Another parameter often used to describe the molecular weight is $\overline{M_p}$, the peak average molecular weight. A list of $\overline{M_p}$ and $\overline{M_w}/\overline{M_n}$ for the polystyrene samples used in this work can be found in Table 8.1.
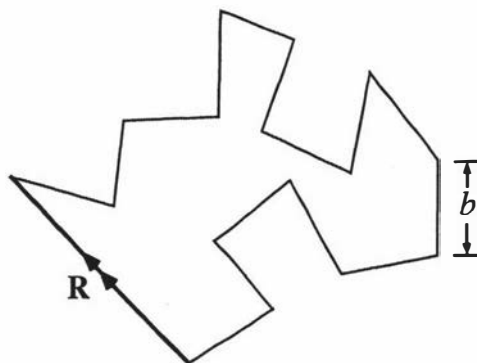
Figure 8.1: Freely jointed model of of a polymer. The end-to-end vector **R** has an r.m.s. end-to-end length of $\sqrt{N}b$ for N links of length b as in eqn (8.3).

Ideal polymer chain

One of the most physically appealing aspects of polymers is that the chemical diversity of the monomers play little part in determining the dynamics of polymer molecules. With the exception of numerical prefactors all polymer molecules scale in the same way. For instance, a freely jointed model of a polymer with N joints of length b with have an r.m.s. end-to-end length of

$$\overline{R} = \langle R^2 \rangle^{1/2} = \sqrt{N}b \tag{8.3}$$

as shown in Figure 8.1.

A polymer can easily be fitted to this model by including enough monomer units in the segment length b such that each segment is conformationally independent of neighbouring segments. In fact this $N^{1/2}$ scaling of the r.m.s. length changes when excluded volume and hydrodynamic effects are introduced, however, for entangled polymers, Flory's theorem states that the chains are ideal and $\overline{R} \sim N^{1/2}$.

8.3 Polymer reptative diffusion theory

The concept of polymer reptation was first proposed by de Gennes[76] and was developed further by Doi and Edwards[77, 92]. An outline of the theory is presented here.

8.3.1 The primitive chain

Reptation is characterized by 1-dimensional Rouse-like[77, 93] curvilinear diffusion in an entanglement tube[92] formed by the topological constraints of surrounding chains. The tube formed by the surrounding polymer chains constrains the enclosed polymer to diffuse only along its own path as shown in Figure 8.2.

For a given polymer configuration, a primitive path can be drawn connecting the two ends of the polymer chain by the shortest path, with the same topology as the chain, relative to the obstacles. A primitive chain can then be used to describe the simplified motion of the polymer moving along the primitive path by disregarding the small scale fluctuations about the path.

The primitive chain has a constant contour length L and a step length a. For any given network a will be of the order of the mesh size, or tube diameter. The
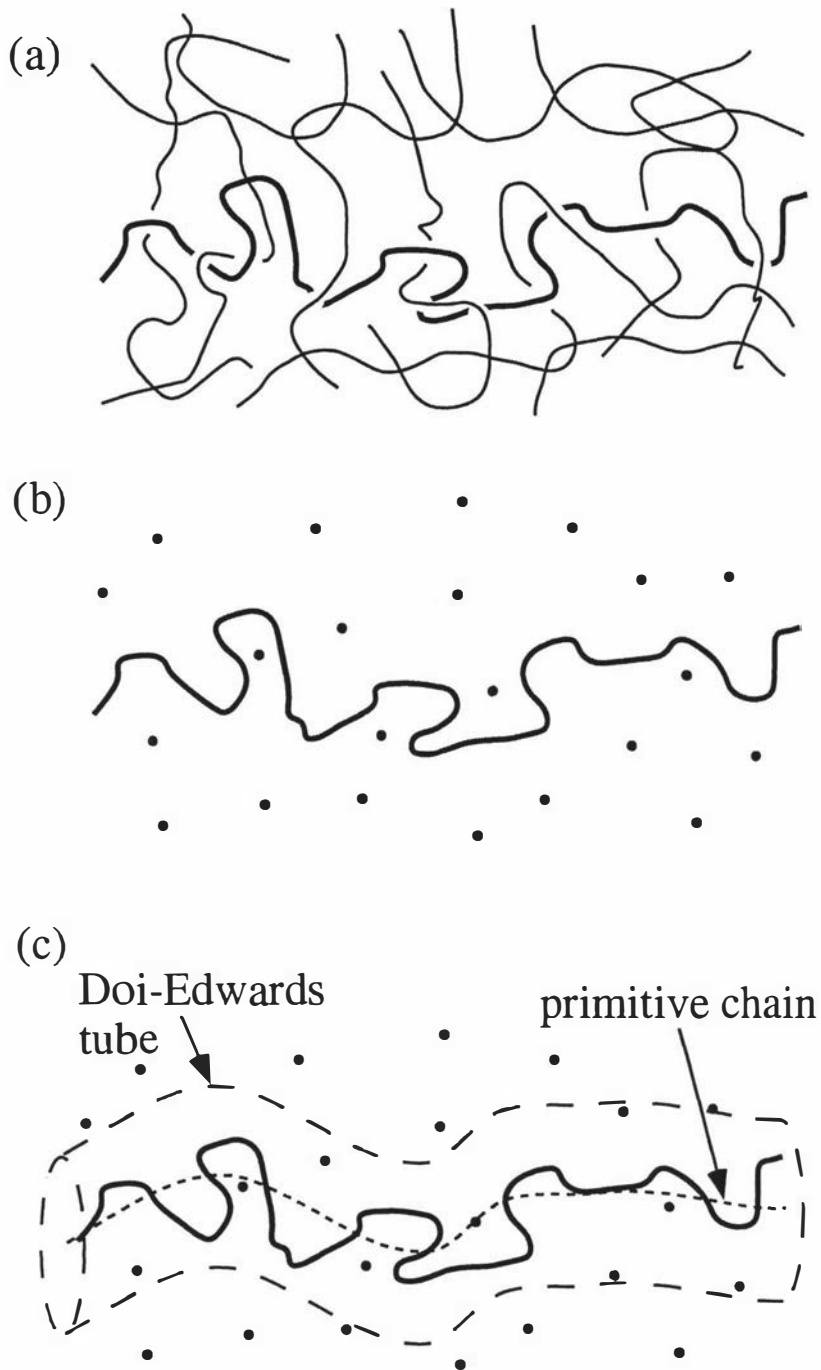
Figure 8.2: (a) Entangled polymer chains with one polymer highlighted. (b) Schematic picture of (a) with the highlighted polymer placed on a plane and dots placed where other polymer strands intersect the plane. (c) The tube model showing the primitive chain and the Doi-Edwards tube. (adapted from ref [77])

number of steps in the chain, Z will be given by

$$Z = \frac{L}{a} \tag{8.4}$$

And for Z steps each of length a we get the mean square length of the primitive chain

$$\overline{R}^2 = Za^2 = La \tag{8.5}$$

which must be equal to the polymer end-to-end length from eqn (8.3) giving

$$Za^2 = Nb^2 \tag{8.6}$$

which implies

$$Z = N\frac{b^2}{a^2} = \frac{\overline{R}^2}{a^2} \tag{8.7}$$

and

$$L = \frac{Nb^2}{a} \tag{8.8}$$

The diffusion coefficient D_c describes the rate at which the primitive chain moves back and forth along itself and is given by

$$D_c = \frac{k_B T}{N\zeta} \tag{8.9}$$

where $k_B T$ is the usual Boltzmann factor and ζ is the viscosity. The diffusion coefficient also scales as $D_c \sim N^{-1}$. This one dimensional curvilinear path has no branching points and can only be changed at the polymer ends, which can find new paths and therefore redefine the tube.

Curvilinear path and the lab frame

When dealing with the primitive path it is important to distinguish between distances along the curvilinear path and distances in three dimensions. If one takes n steps of length a along the primitive chain from point s' to s then the distance travelled along the path is

$$|s - s'| = na \tag{8.10}$$

However in the lab frame the primitive path is a random walk and the mean squared distance travelled in the lab frame is

$$\langle (\mathbf{R}(s) - \mathbf{R}(s'))^2 \rangle = a|s - s'| = na^2 \tag{8.11}$$

which can be compared to eqn (8.5). In other words motion along the tube by a curvilinear distance s results in motion of a distance $(as)^{1/2}$ in three dimensions.

Diffusion of primitive chain along a curvilinear path

By introducing the curvilinear diffusion coefficient D_c, which diffuses a curvilinear mean squared distance of $2D_c t$ in a time t

$$2D_c t = |s - s'|^2 = n^2 a^2 \tag{8.12}$$

which in three dimensions gives[77]

$$\langle (\mathbf{R}(s) - \mathbf{R}(s'))^2 \rangle = \frac{2D_c t}{n} = a(2D_c t)^{1/2} \tag{8.13}$$

Eqn (8.13) implies that the mean squared displacement of the polymer trapped in a tube will vary as $t^{1/2}$ and not t as for normal Brownian diffusion. This effect can be easily measured with PGSE which always measures the mean squared displacement on the initial slope of a Stejskal-Tanner plot. The diffusion coefficient measured on such a plot will vary as $D \sim \Delta^{-1/2}$

Tube disengagement

To calculate the motion of the primitive chain Doi and Edwards[77] found the mean square displacement of a primitive chain segment. Mathematically it is convenient to calculate the following time correlation function

$$\phi(s, s'; t) = \langle (\mathbf{R}(s, t) - \mathbf{R}(s', 0))^2 \rangle \tag{8.14}$$

which due to the one-dimensional nature of the chain gives the same result. The diffusion equation to solve is

$$\frac{\partial}{\partial t} \phi(s, s'; t) = D_c \frac{\partial^2}{\partial s^2} \phi(s, s'; t) \tag{8.15}$$

where D_c is the curvilinear diffusion coefficient along the primitive path. Eqn (8.15) has solution[77]

$$\phi(s, s'; t) = \frac{2D_c t}{Z} + \sum_{p=1}^{\infty} \frac{4La}{p^2 \pi^2} \cos^2 \left(\frac{p\pi s}{L} \right) [1 - \exp(-p^2 \, t/\tau_d)] \tag{8.16}$$

where the time constant τ_d, called the reptation or disengagement time, is a relaxation time describing the time it takes the primitive chain to disengage from the tube it was confined to initially, and is given by

$$\tau_d = \frac{L^2}{D_c \pi^2} \tag{8.17}$$

Long time limit

In the long time limit where $t \gg \tau_d$ eqn (8.16) reduces to

$$\phi(s, s'; t) = \frac{2D_c t}{Z} \tag{8.18}$$

The polymer motion is completely Brownian, as expected, and the mean squared displacement scales directly with t. The timescale is long enough such that the polymer completely loses any memory of its initial tube and can effectively diffuse
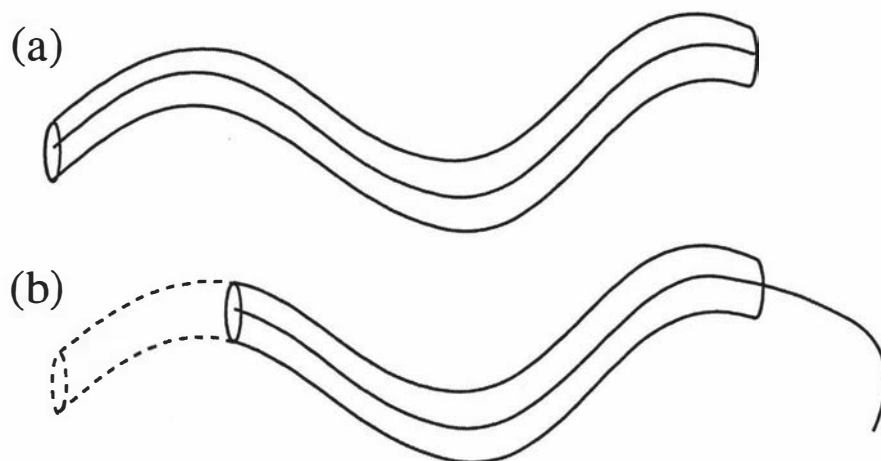
Figure 8.3: The process of tube disengagement. The polymer is described by the primitive chain confined to a tube as shown in (a). As the primitive chain diffuses along the tube, memory of a section of the tube is forgotten, as shown in (b). A completely new tube will be formed over a time interval τ_d. (adapted from ref [77])

randomly in any direction. A three dimensional center of mass diffusion constant D_s can be defined as

$$D_s = \lim_{t \to \infty} \frac{\phi(s, s'; t)}{6t} = \frac{D_c}{3Z} = \frac{k_B T a^2}{3 N^2 \zeta b^2} \tag{8.19}$$

using eqn (8.9) and eqn (8.18). Notice that $D_s \sim N^{-2}$, which gives the M^{-2} dependance of self-diffusion coefficient, often used as an indication of entanglement. Eqn (8.18) can be rewritten in terms of $\overline{R}^2$, the mean square end-to-end length of the polymer, as

$$\phi(t) = 6D_s t = \frac{2\overline{R}^2}{\pi^2} \left(\frac{t}{\tau_d}\right) \tag{8.20}$$

and therefore[77]

$$\tau_d = \frac{\overline{R}^2}{3\pi^2 D_s} = \frac{N^3 b^4 \zeta}{\pi^2 k_B T a^2} \tag{8.21}$$

Short time limit

For the case where $t \ll \tau_d$ eqn (8.18) reduces to

$$\phi(t) = 2a \left(\frac{D_c t}{\pi}\right)^{1/2} = 2\overline{R}^2 \left(\frac{t}{\pi^3 \tau_d}\right)^{1/2} \tag{8.22}$$

as suggested by eqn (8.13) above. The $t^{1/2}$ dependance of $\phi(t)$ results directly from observing free diffusion confined to a curvilinear path. The crossover from one limit to the other occurs when the mean square diffusion is of the order of $\overline{R}^2$ and at a time of approximately $\pi \tau_d$.

Structure functions for primitive chain

The PGSE echo attenuation structure function can be calculated from[31]

$$E(\mathbf{q}) = \langle \exp[i2\pi\mathbf{q} \cdot (\mathbf{R}_n(t) - \mathbf{R}_n(0))] \rangle. \tag{8.23}$$

A solution for eqn (8.23) for a segment at position s was found by Doi and Edwards. We integrated their solution[92] over the polymer length L to get

$$E(q) = \sum_{p=1}^{\infty} \left\{ \frac{2\mu}{\mu^2 + \alpha_p^2 + \mu} \cos^2\left[1 + \frac{\sin(2\alpha_p)}{(2\alpha_p)}\right] \exp\left(\frac{-4Dt\alpha_p^2}{L^2}\right) \right. $$
$$\left. + \frac{2\mu}{\mu^2 + \beta_p^2 + \mu} \sin^2\left[1 - \frac{\sin(2\alpha_p)}{(2\alpha_p)}\right] \exp\left(\frac{-4Dt\beta_p^2}{L^2}\right) \right\} \tag{8.24}$$

where $\mu = \pi^2 q^2 aL/3$ and α_p and β_p are the solutions of the equation

$$\begin{aligned} \alpha_p \tan\alpha_p &= \mu \\ \beta_p \cot\beta_p &= \mu. \end{aligned} \tag{8.25}$$

The limiting case for eqn (8.24) in the low-q limit where $q\overline{R} \ll 1$ is

$$E(q) = \exp(-4\pi^2 q^2 D_s t) \tag{8.26}$$

as expected.

8.3.2   Internal dynamics: Rouse motion and the primitive chain

Superposed on the primitive chain dynamics of an entangled polymer is the internal motion of the polymer about the primitive path. These small-scale fluctuations can be represented by the Rouse model[93]. This model, which ignores hydrodynamic and excluded volume effects, is too simplistic for dilute polymer solutions, but lends itself nicely to entangled polymer systems, where these extra interactions are not significant. The Rouse model is based upon a bead and spring model for the polymer.

Rouse model in a tube

The dynamics of a Rouse polymer can be described by the mean square laboratory frame displacement of a Rouse segment.

$$\phi_n(t) = \langle [\mathbf{R}_n(t) - \mathbf{R}_n(0)]^2 \rangle. \tag{8.27}$$

where $\mathbf{R}_n$ is the position of the nth Rouse segment. At the shortest timescales, the segments in an entangled polymer would be unaware of the restrictions imposed by the constraining network and $\phi_n(t)$ is given by the expression for the Rouse model in free space[77].

$$\phi_n(t) = 6D_c t + \frac{4Nb^2}{\pi^2} \sum_{p=1}^{\infty} \frac{1}{p^2} \cos^2\left(\frac{p\pi n}{N}\right) [1 - \exp(-p^2 t/\tau_R)] \tag{8.28}$$

where D_c is given by eqn (8.9). The parameter τ_R, the time constant of the longest dominant internal mode, is called the Rouse time and is given by

$$\tau_R = \frac{\overline{R}}{3\pi^2 D_c}. \tag{8.29}$$

Comparison with eqn (8.17) shows

$$\tau_R = \tau_d/3Z. \tag{8.30}$$

Since $t \ll \tau_R$ for short timescales, eqn (8.28) can be approximated by

$$\phi_n(t) = 2\overline{R}^2 \left(\frac{t}{\pi^3 \tau_R}\right)^{1/2} \simeq \left(\frac{k_B T b^2 t}{\zeta}\right)^{1/2} \tag{8.31}$$

The mean square dependance on $t^{1/2}$ motion is accurate until the segmental displacement becomes comparable with a, the tube diameter. The dynamic timescale for the onset of tube constraint effects on segmental motion is given by τ_e, the equilibration time, where

$$\tau_e \simeq \frac{a^4 \zeta}{k_B T b^2} = \frac{a^4}{D_c \overline{R}^2}. \tag{8.32}$$

Rouse model along primitive path

For times $t > \tau_e$ the motion of the Rouse segment along the primitive path is free, but motion transverse to the path is restricted. The mean square displacement is calculated using normal Rouse motion, but directing it along the one-dimensional primitive path. The mean square displacement of a Rouse segment along the tube is given by[77]

$$\langle (s_n(t) - s_n(0))^2 \rangle = 2D_c t + \frac{4Nb^2}{3\pi^2} \sum_{p=1}^{\infty} \frac{1}{p^2} \cos^2\left(\frac{p\pi n}{N}\right)[1 - \exp(-p^2 t/\tau_R)] \tag{8.33}$$

where s_n is the displacement of the nth Rouse segment along the tube. The two limits of eqn (8.33) are

$$\langle (s_n(t) - s_n(0))^2 \rangle = 2\overline{R}^2 \left(\frac{t}{\pi^3 \tau_R}\right)^{1/2} \simeq (k_B T b^2 t/\zeta)^{1/2} \tag{8.34}$$

for $t < \tau_R$ and

$$\langle (s_n(t) - s_n(0))^2 \rangle = 2D_c t \tag{8.35}$$

for $t > \tau_R$. To calculate the displacement $\phi_n(t)$ in the laboratory frame, eqn (8.11) can be used to show

$$\phi_n(t) = a|s_n(t) - s_n(0)| \simeq a\langle (s_n(t) - s_n(0))^2 \rangle^{1/2} \tag{8.36}$$

which gives for $\tau_e < t < \tau_R$

$$\phi_n(t) = 2a\overline{R}^2 \left(\frac{t}{\pi^3 \tau_R}\right)^{1/4} \simeq a(k_B T b^2 t/\zeta)^{1/4} \tag{8.37}$$

and for $\tau_R < t < \tau_d$,

$$\phi_n(t) = a(2D_c t)^{1/2} \simeq a(k_B T t/N\zeta)^{1/2}. \tag{8.38}$$

A most intriguing aspect of $\phi_n(t)$ is that it is proportional to $t^{1/4}$ in the time regime $\tau_e < t < \tau_R$. This specific diffusion behaviour has been considered a "signature" for reptation and was first predicted by de Gennes[76]. The transition from $t^{1/4}$ behavior to $t^{1/2}$ occurs at approximately $3\pi^2 \tau_R$. The behaviour for $\tau_R < t < \tau_d$ agrees well with the behaviour predicted by the primitive chain.

Region	Dynamic timescale	Lab-frame displacement	Displacement scaling
I	$t < \tau_e$	$\phi_n(t) < a^2$	$\phi_n(t) \sim t^{1/2}$
II	$\tau_e < t < \tau_R$	$a^2 < \phi_n(t) < \overline{R}a$	$\phi_n(t) \sim t^{1/4}$
III	$\tau_R < t < \tau_d$	$\overline{R}a < \phi_n(t) < \overline{R}^2$	$\phi_n(t) \sim t^{1/2}$
IV	$\tau_d < t$	$\overline{R}^2 < \phi_n(t)$	$\phi_n(t) \sim t$

Table 8.2: The characteristics of the four different timescale regions of polymer reptation as shown in Figure 8.4

8.3.3   Time scale regimes

The different dynamic timescale regimes are summarised in Table 8.2 and Figure 8.4. The regimes can be described as follows:

I Free Rouse motion:

For short time intervals up to τ_e, the polymer segments are unaware of the influence of the tube and therefore exhibit free Rouse motion with $t^{1/2}$ scaling of $\phi_n(t)$.

II Rouse motion constrained to the tube:

For times $t > \tau_e$ the motions of segments perpendicular to the tube are restricted, but motion along the path formed by the tube is unrestricted. The Rouse motion is directed along a one-dimensional path in a three-dimensional laboratory frame of reference resulting in a $t^{1/4}$ scaling law for $\phi_n(t)$.

III Curvilinear diffusion in the tube:

For times $t > \tau_R$ the polymer motion along the tube is no longer dominated by internal Rouse motion, but by curvilinear diffusion directed along the primitive path. $\phi_n(t)$ therefore scales as $t^{1/2}$ due to the one-dimensional nature of the tube.

IV Long range centre-of-mass motion:

Finally the polymer is able to move into a completely new tube for times $t > \tau_d$ and losses all memory of its initial starting position. The diffusion is now random and Brownian with a normal t scaling for $\phi_n(t)$.

8.4   Experiments

Samples were made by dissolving high molecular weight, monodisperse polystyrene in CCl_4 at concentrations of 2.2%, 9% and 13% volume fraction. Three types of PGSE experiment were performed[94]. In the first, the self-diffusion coefficient D_s of each sample was obtained from a standard Stejskal-Tanner plot of PGSE data. The large gradients available from our gradient coil (12.1 T m^{-1} at 10 A) enabled D_s values down to 6×10^{-15} m^2 s^{-1} to be measured. In these experiments the M^{-2} scaling law of D_s was investigated.
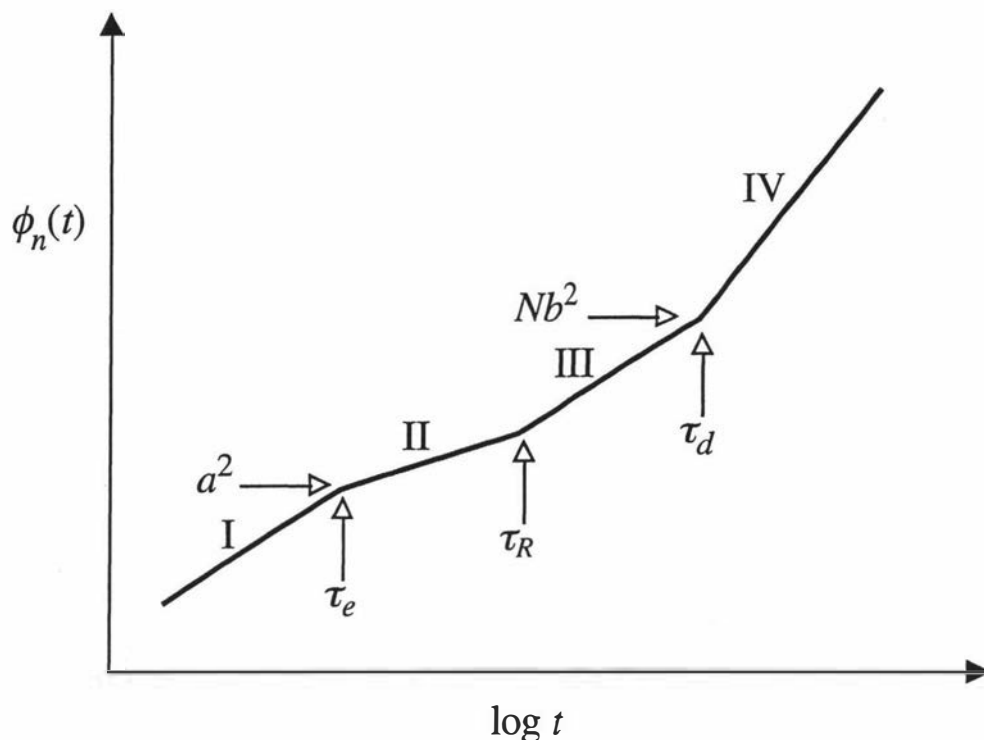
Figure 8.4: Mean squared displacement, $\phi_n(t)$, of a chain segment plotted against time on a log graph. The characteristics of the four regions are described in Table 8.2. The slopes from each regime reveals the scaling dependence of $\phi_n(t)$ on t and are 1/2 (I), 1/4 (II), 1/2 (III) and 1 (IV) respectively. (adapted from ref [77])

In the second set of experiments, PGSE data was collected for a subset of samples with a range of diffusion times Δ. The mean-squared displacement was found from the initial slope of the PGSE data on a Stejskal-Tanner plot. By using both spin and stimulated echoes, Δ values from 7 to 950 ms were available. The time dependence of the the mean squared displacement, $\langle z(t)^2 \rangle$, was investigated.

Finally, a set of PGSE-MASSEY experiments were performed in which very large gradients (up to 15 T m^{-1}) were used to acquire structure function curves for the entangled polymers.

8.4.1 Self-diffusion dependence on M

Figure 8.5 shows D_s vs M for polystyrene in carbon tetrachloride (CCl$_4$) at a concentration of 9% (volume fraction). Note that in obtaining the data shown in Figure 8.5 it was ensured that the diffusion time was sufficiently long for centre-of-mass motion, where $\phi(t) \sim t$, by utilizing a stimulated echo sequence where necessary. The data are consistent with the $D_s \sim M^{-2}$ prediction but due to the limited region of scaling we do not regard such behaviour as convincing evidence of reptation. In fact there are non-reptative models[95, 96, 97, 98] for semi-dilute polymer diffusion which also predict a M^{-2} scaling dependence for D_s.

8.4.2 Mean squared displacement dependence on time

For the $\phi(t)$ vs t experiments we have chosen a high molar mass subset of the prepared samples using M values well in excess of 1×10^6 daltons and varied the

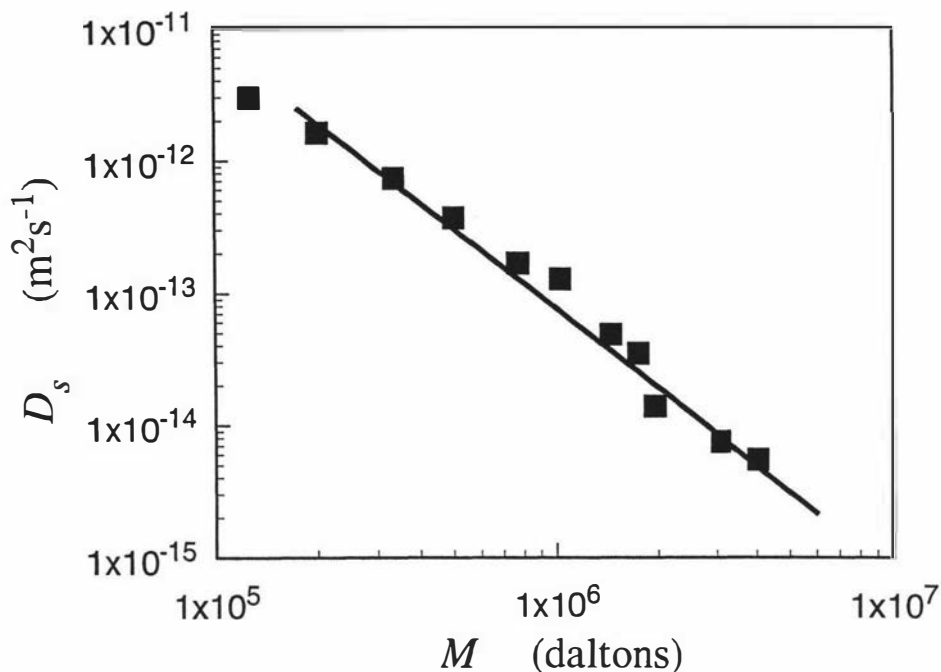**Figure 8.5**: Dependence of self-diffusion coefficient, D_s, on molecular mass M for polystyrene in CCl$_4$ as 9% volume fraction. The straight line has a slope of -2 and indicates the $D_s \sim M^{-2}$ scaling law. The value of D_s for the 15×10^6 dalton sample in Table 8.3 is obtained from this graph by extrapolation.

observation times over the widest possible range. Using literature values of $\overline{R}$ and the D_s data of Figure 8.5, equations (8.7), (8.17) and (8.29) can be used to generate the parameters shown in Table 8.3. Note that in the case of the 9%, 15×10^6 dalton polystyrene sample, where $\tau_d \simeq 10$ s, the self-diffusion coefficient in region IV cannot be measured directly and we use Figure 8.5 to obtain D_s by extrapolation assuming $D_s \sim M^{-2}$. The value for D_s for the 13% 15×10^6 dalton sample is then calculated assuming the concentration, c scales as c^{-3}[77]. The minimum numbers of entanglements are calculated by assuming $a \leq 320$ Å for the 9% solutions, a choice which shall subsequently justified. Using this upper limit we may calculate the number of primitive path steps, Z, using eqn (8.7). The values of $Z \geq 10$ represent sufficient entanglements for the tube model to apply[88] for these polymer solutions. It should also be noted that three of the calculated tube disengagement times cause $\pi\tau_d$ to lie within the experimental time window of PGSE-NMR.

Figure 8.6 shows $\phi(t)$ vs t obtained from the low q dependence of $E(q, t)$ for four of the polymer solutions of Table 8.3. While Figure 8.6a compares the data with scaling lines for $t^{1/4}$, $t^{1/2}$ and t^1 behaviour, in Figure 8.6b the data are compared with the numerical predictions of the Doi-Edwards theory given by eqns (8.16), (8.33) and (8.36). A transition region from $\phi(t) \sim t$ to $\phi(t) \sim t^{1/2}$ is clearly visible for three of the four polymer systems as the observation time is reduced below 1 s. In each case the position of this transition closely agrees with the theoretical reptation prediction. For the 15×10^6 dalton polystyrene at 9% concentration no such transition is apparent, consistent with our calculated value of τ_d. It is important to note that, in the region $t \geq \tau_R$, the theoretical curves of Figure 8.6b contain no adjustable parameters and use only the empirical D_s and $\overline{R}$ values shown in Table 8.3. The chosen value of a is significant only in the region $t < \tau_R$.

The transition from $\phi(t) \sim t^{1/2}$ to $\phi(t) \sim t^{1/4}$ would be expected in the vicinity
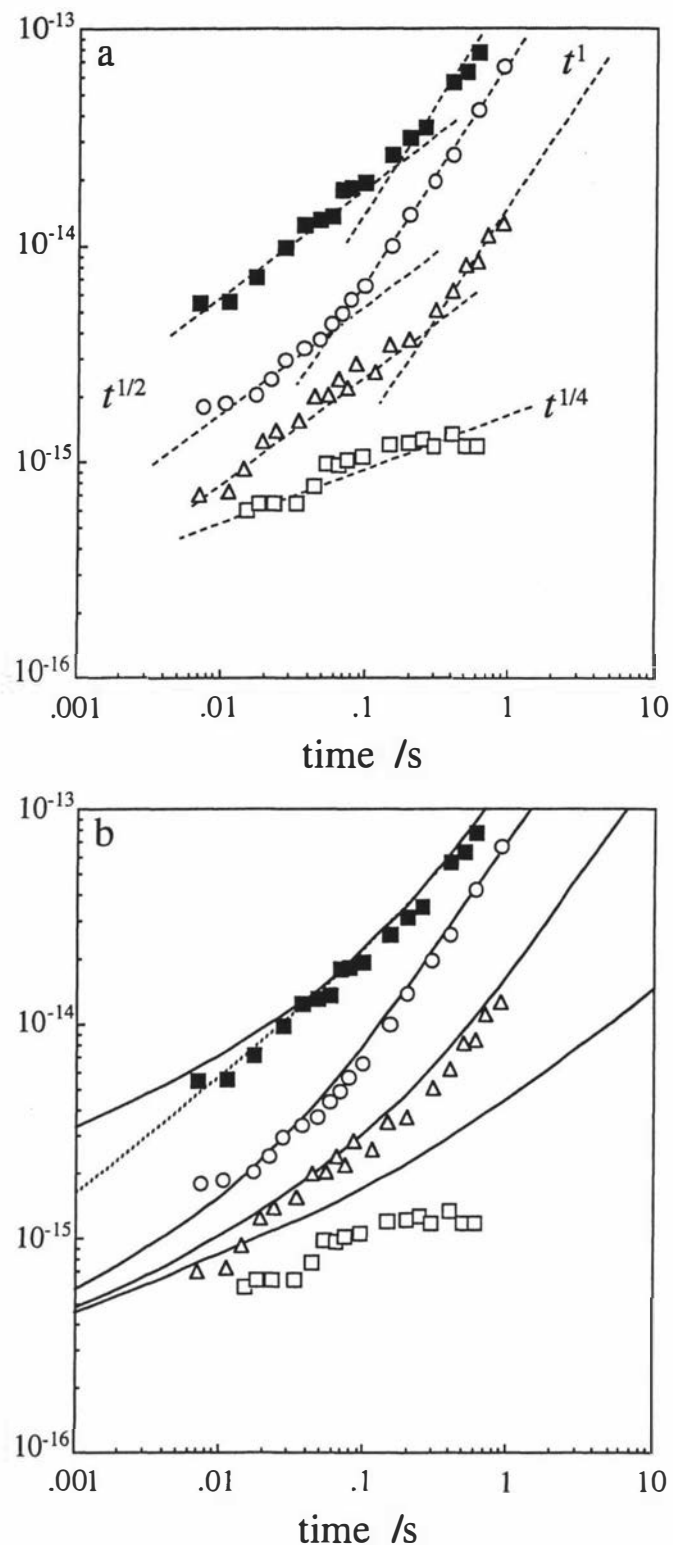
Figure 8.6: $\langle z(t)^2 \rangle$ vs t data for polystyrene in CCl_4 (filled squares 2.4% 15×10^6 daltons, open circles 10% 1.8×10^6 daltons, open triangles 10% 3.0×10^6 daltons, open squares 10% 15×10^6 daltons). Note that $\phi(t) = 3\langle z(t)^2 \rangle$, z being the component of displacement along q. (a) The data are compared with asymptotic lines for $t^{1/4}$, $t^{1/2}$, and t scaling. (b) The solid curves correspond to Doi-Edwards theory for regions II, III and IV, calculated using the parameters of Table 8.3. For the 2.2% 15×10^6 dalton system the effect of the transition from II to III is shown in the upper solid curve whereas the lower dashed line corresponds to the Doi-Edwards prediction incorporating only regions III and IV.

M_p (daltons)	Volume fraction (%)	$\overline{R}$ (Å)	D_s (m^2s^{-1})	a (Å)	Z	τ_d (s)	τ_R (ms)
15×10^6	9	2900	3.5×10^{-16}	320	82	8.1	33
3.0×10^6	9	1300	7.5×10^{-15}	320	17	0.076	1.5
1.8×10^6	9	990	3.5×10^{-14}	320	10	0.010	0.33
15×10^6	2.2	3100	6.5×10^{-14}	930	11	0.050	1.5
15×10^6	13	2700	1.5×10^{-16}	280	93	16	58

Table 8.3: Parameters for the polymer systems used in this work. The values for $\overline{R}$ were obtained from concentration-dependent radii for polystyrene in CS_2[99] for which the dilute solution coil expansion factor is approximately 1.7, the same as in CCl_4[99, 100].

$t \sim 3\pi^2 \tau_R$, and at a length scale $\overline{R}a$. Reference to Table 8.3 indicates that, given the chosen upper limit values of a , we would expect to just see this transition within the PGSE-NMR timescale only for the 10% solution of 3.0×10^6 dalton polystyrene and the 2.4% solution of 15×10^6 dalton polystyrene in CCl_4. Our data does not clearly indicate such a transition for these polymer systems, suggesting possibly that a is somewhat smaller than the chosen maximum. However we do see a clear $t^{1/4}$ region in the case of the 10% solution of 15×10^6 dalton polystyrene, although the absolute values of the mean square displacements are somewhat below the predictions of Doi-Edwards theory based on the value of D_s extrapolated for this polymer. It should be noted that the theory represents the data well if a value of D_s is chosen which is a factor of 5 lower. This casts some doubt on the use of M^{-2} scaling to obtain D_s by extrapolation.

One other prediction of Doi-Edwards theory is that the $\phi(t)$ vs t data for a common tube diameter should converge at $\phi(\tau_e) \simeq a^2$. For the three sets of data corresponding to different molar masses with a common solution concentration, and hence tube diameter, a high degree of convergence is apparent at short observation times. We note that the convergence value of $\langle z(t)^2 \rangle$ is $\leq 3 \times 10^{-16}$ m^2, consistent with the maximum value of a assumed before.

8.4.3   Structure factor

So far we have considered only the motion of the primitive chain measured using the low-q limit of eqn (8.23). Superposed on this is the rapid Rouse motion about the primitive chain which occurs at distance scales shorter than a. To examine this "local" motion it is necessary to measure the high-q dependence of $E(\mathbf{q})$. The incoherent dynamic structure factor of eqn (8.23) represents the Fourier transform of the average propagator of the motion as explained in Section 3.3.2. We shall find it convenient to treat the local motion and the longer-range primitive chain motion as stochastically independent so that the total average propagator is a convolution of local and primitive chain propagators. In consequence the overall dynamic structure factor will be a product of factors for the local and primitive chain motions.

Because the PGSE NMR observation time greatly exceeds τ_e, the average prop-
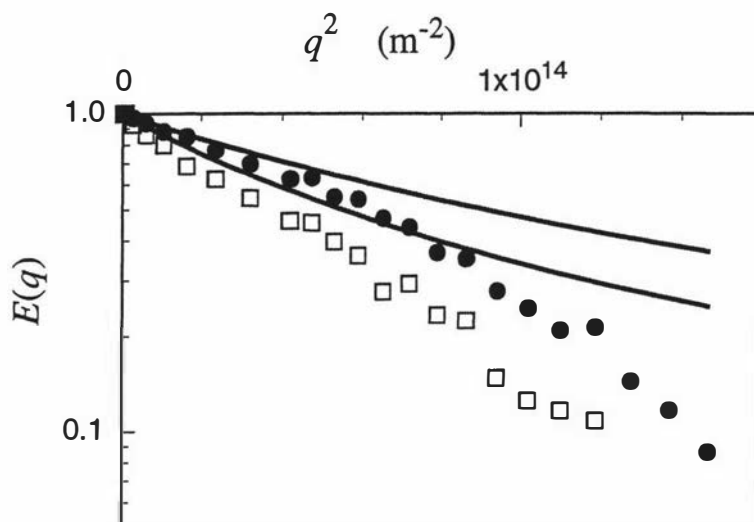
Figure 8.7: $E(q)$ vs q^2 for 15×10^6 daltons polystyrene at 9% (filled circles) and 13% (open squares) in CCl_4. The observation time is 48.5 ms, sufficiently long for the PGSE narrow pulse approximation to hold. The theoretical lines correspond to Doi-Edwards incoherent structure factors of eqn (8.24) and the downwards deviation of the data at high q is believed to arise from time-averaged local Rouse motion restricted within the entanglement tube.

agator for this local motion is an autocorrelation function of the polymer segments density distribution, $\rho_1(\mathbf{r})$, in their motion transverse to the tube. This leads to a structure factor $|S_1(\mathbf{q})|^2$ where $S_1(\mathbf{q})$ is the Fourier transform of $\rho_1(\mathbf{r})$. Consequently

$$E(\mathbf{q}) = |S_1(\mathbf{q})|^2 E_{pc}(\mathbf{q}) \tag{8.39}$$

where $E_{pc}(\mathbf{q})$ is the primitive chain dynamic structure factor. A suitable choice for $\rho_1(\mathbf{r})$ is the Gaussian distribution, $(2\pi\sigma)^{-1/2} \exp(-\mathbf{r}^2/2\sigma^2)$ where 2σ may be regarded as the tube diameter. This would lead to $|S_1(\mathbf{q})|^2$ of $\exp(-4\pi^2 q^2 \sigma^2)$. $E_{pc}(\mathbf{q})$ is given by eqn (8.24) for regions III and IV but we are unaware of any analytic expression for the region II incoherent structure factor. For the purpose of interpreting $|S_1(\mathbf{q})|^2$ we therefore use the extrapolated region III $E_{pc}(\mathbf{q})$ dynamic structure factor as an approximation.

Figure 8.7 shows $E(q)$ vs q^2, for 15×10^6 polystyrene/CCl_4 solutions at 9% and 13% concentrations. These data were obtained at a fixed measurement time of 48.5 ms. Also shown are the corresponding $E_{pc}(q)$ curves calculated using values of $\overline{R}$ and D_s values given in Table 8.3. It is clear that the concave nature of $E_{pc}(q)$ vs q^2 permits the observation of $|S_1(q)|^2$ attenuation provided $qa \sim 1$. From the e^{-1} points of this additional attenuation we estimate tube diameter values of 320 Å and 280 Å for the 9% and 13% solutions. At best these values are rough estimates. We note that their ratio is not consistent with the expected $c^{-0.75}$ dependence, a fact which may reflect hydrodynamic influences[101]. A more detailed analysis would require an accurate description of $E_{pc}(q)$ over the entire range of q employed here. However, it is clear that the present data enable us to set upper limits on the value of a. Both the $E(q)$ vs q^2 data and the $\phi(t)$ vs t data are consistent with a tube diameter smaller than 320 Å for the 9% solutions.

8.5 Summary

It should be emphasised that the q values used here are unusually large for PGSE-NMR ($2\pi q \sim (130\ \text{Å})^{-1}$) and that the data reliability depends on the echo-stabilising effect of the PGSE-MASSEY technique described in Chapter 5. In the event that the additional attenuation evident at high q contains an instrumental artifact, we may take the values of a determined here as upper limits. While our conclusions regarding magnitude of the tube diameters in semi-dilute solution are somewhat tentative, the establishment of these maximum values lends credence to the tube depiction for the very high molar mass polymer solutions used in this work.

By contrast we attach a high degree of significance to the $\phi(t)$ vs t observations shown in Figure 8.6. While such transitional behaviour has been found in computer simulations[84, 85, 86], to our knowledge, this data represents the first direct measurement of the motional regimes long considered a signature for reptation.

PGSE has been extensively used to measure polymer diffusion coefficients[100, 102, 103], but has been limited to distance scales too large to measure the internal motions of entangled polymers. However, with the introduction of both the stray field gradient technique[25], and the PGSE-MASSEY technique[54] used here, there will be significant advances in this field.

Chapter 9

Conclusion

9.1 Summary

The use of the reciprocal q-space analysis in this thesis has been central to extending the scientific use of Pulsed Gradient Spin Echo experiments. The fundamental ideas of the technique can been seen in the parallel barrier ideas discussed in Chapter 6. The use of the 100 μm microslides was a key factor in being able to obtain the excellent diffraction peaks observed. The extension to the original Stejskal-Tanner equation to incorporate the Brownstein-Tarr effects of edge relaxation allows the technique to be used on more realistic samples. A fundamental idea is that the PGSE experiment is not limited by typical imaging signal to noise considerations. By using larger magnetic field gradients, be they ordinary pulsed gradients with the PGSE-MASSEY technique or superconductor magnet static field gradients, one can theoretically probe smaller displacements.

The extension of this theory to incorporate porous systems is shown in Chapter 7. Both the Gaussian envelope and pore hopping theories are discussed. Analysis of experiments on the packed array of monodisperse polystyrene spheres has proved excellent in being able to extract important structural information about the system. By using the PGSEPLOT program we have been able to fit the pore hopping theory to the data and get parameters consistent with the known dimensions of the sphere array. Computer simulations have also proved useful in finding the limitations of the theory with real samples.

The question of polymer dynamics in semi-dilute solution has been studied in Chapter 8, and provided an opportunity to measure small displacements in highly viscous samples. By utilising our high gradient system and the MASSEY technique we have been able to probe the internal dynamics of such polymers. The experiments show a transition from center-of-mass diffusion to diffusion restricted along the one dimensional path of the polymer tube. Again by using the reciprocal space analysis we have been able to "measure" the size of the tube. These measurements are some of the highest q measurements made to date in the literature.

9.2 Future work

The possibility for future work exists in all three aspects of this thesis. The restricted diffusion experiments from Chapter 6 have seen several recent extensions to the theory. Echo attenuation functions using the narrow pulse approximation for

all three geometries now exist incorporating the effects of relaxation at the walls. A theory also exist for the harmonic potential well, which may prove useful in experiments on entangled polymers. However there have been few PGSE experiments performed on real systems to test the usefulness of these models in extracting real structural information from model systems. If further work in this field, especially testing spherical systems, proves that these techniques are useful, then the possibility to extend the experiments to real samples of interest would exist. As the available gradient strengths increase, using techniques like PGSE-MASSEY, then q-space imaging, in principle, can be applied to smaller systems (< 0.1 μm) where a slowly diffusing probe molecule could enable 'imaging' of the structure at unrealised resolutions involving NMR.

The porous experiments of Chapter 7 seem to have attracted considerable interest from workers in this field. Many industries, in particular the oil industry, have shown considerable interest in the possibility of PGSE NMR being used to understand and measure porous diffusion. Although the pore hopping theory is simple, and for real systems, unrealistic, it has been successful in fitting PGSE data from model porous systems. Several other groups have now also observed the diffractive coherence peak in PGSE experiments on porous samples. Further work will be needed to understand how much these diffractive effects will still be observable in real systems of interest. However with the help of computer simulations and some extensions to the theory it should be possible to use this technique successfully in real samples of interest.

The understanding of polymer diffusion has attracted a large amount of interest since the 1960's. The repatative models of de Geenes and Doi and Edwards have been central to the understanding of entangled polymer dynamics. There are many groups working in this field, several of which use PGSE to measure molecular dynamics. With the increase in available q made possible by the PGSE-MASSEY technique and the superconducting magnet stray-field method, it should be possible to measure the small displacements needed to accurately clarify the mechanisms involved in semi-dilute polymer diffusion.

Bibliography

[1] A. Abragam. *Principles of nuclear magnetism*. Clarendon Press, Oxford, (1961).

[2] C. P. Slichter. *Principles of magnetic resonance*. Harper and Row, New York, (1963).

[3] T. C. Farrar and E. D. Becker. *Pulse and Fourier Transform NMR*. Academic Press, New York, (1971).

[4] L. I. Schiff. *Quantum Mechanics*. McGraw-Hill, New York, (1968).

[5] H. Nyquist. *Phys. Rev.*, **32**, 110 (1928).

[6] J. D. Kraus and K. R. Carver. *Electromagnetism*. McGraw-Hill, New York, (1973).

[7] D. I. Hoult and R. E. Richards. *J. Magn. Reson.*, **24**, 71 (1976).

[8] D. I. Hoult and R. E. Richards. *Proc. Roy. Soc. (London)*, **A344**, 311 (1975).

[9] E. L. Hahn. *Phys. Rev.*, **80**, 580 (1950).

[10] P. C. Lauterbur. *Nature*, **242**, 190 (1973).

[11] P. Mansfield and P. K. Grannell. *J. Phys. C : Solid State Phys.*, **6**, 422 (1973).

[12] H. Y. Carr and E. M. Purcell. *Phys. Rev.*, **94**, 630 (1954).

[13] P. Mansfield and P. G. Morris. *NMR imaging in biomedecine*. Academic Press, New York, (1982).

[14] F. Reif. *Fundamentals of statistical and thermal physics*. McGraw-Hill, New York, (1965).

[15] D. E. Woessner. *J. Chem. Phys.*, **34**, 2057 (1961).

[16] D. W. McCall, D. C. Douglass, and E. W. Anderson. *Ber. Bunseges. Phys. Chem.*, **67**, 336 (1963).

[17] E. O. Stejskal and J. E. Tanner. *J. Chem. Phys.*, **42**, 288 (1965).

[18] E. O. Stejskal. *J. Chem. Phys.*, **43**, 3597 (1965).

[19] T. L. James and G. G. McDonald. *J. Magn. Reson.*, **11**, 58 (1973).

[20] J. Karger, H. Pfeifer, and W. Heink. Principles and application of self-diffusion measurements by nuclear magnetic resonance. In J. S. Waugh, editor, *Advances in Magnetic Resonance, 12.* Academic Press, San Diego, (1988).

[21] P. T. Callaghan. *Austr. J. Phys.*, **37**, 359 (1984).

[22] P. Stilbs. *Progress in NMR Spectroscopy*, **19**, 1 (1987).

[23] J. Stepisnik. *Physica B*, **104**, 350 (1981).

[24] J. E. Tanner. *J. Chem. Phys.*, **52**, 2523 (1970).

[25] R. Kimmich, W. Unrath, G. Schnur, and E. Rommel. *J. Magn. Reson.*, **91**, 136 (1991).

[26] R. Kimmich and E. Fischer. *J. Magn. Reson. A*, **106**, 229 (1994).

[27] L. Van Hove. *Phys. Rev.*, **95**, 249 (1954).

[28] P. A. Egelstaff. *An introduction to the liquid state.* Academic Press, New York, (1967).

[29] J. Crank. *The mathematics of diffusion.* Oxford University Press, (1975).

[30] J. Karger and W. Heink. *J. Magn. Reson.*, **51**, 1–7 (1983).

[31] P. T. Callaghan. *Principles of nuclear magnetic resonance microscopy.* Clarendon Press, Oxford, (1991).

[32] D. G. Cory and A. L. Garroway. *Magn. Reson. Med.*, **14**, 435 (1990).

[33] C. D. Eccles. *Microscopic NMR imaging.* PhD thesis, Massey University, (1987).

[34] Y. Xia. Static and dynamic imaging using magnetic field gradients. Master's thesis, Massey University, (1988).

[35] Y. Xia. *Dynamic NMR microscopy.* PhD thesis, Massey University, (1992).

[36] D. C. Champeney. *Fourier transformations and their physical applications.* Academic Press, New York, (1973).

[37] A. Coy and P. T. Callaghan. *J. Chem. Phys.*, **101**, 4599 (1994).

[38] P. T. Callaghan, A. Coy, D. MacGowan, K. J. Packer, and F. O. Zelaya. *Nature*, **351**, 467 (1991).

[39] J. E. Tanner and E. O. Stejskal. *J. Chem. Phys.*, **49**, 1768 (1968).

[40] P. P. Mitra and P. N. Sen. *Phys. Rev. B*, **45**, 143 (1992).

[41] P. P. Mitra, P. N. Sen, and L. Schwartz. *Phys. Rev. B*, **47**, 8565 (1993).

[42] P. T. Callaghan and A. Coy. PGSE NMR and molecular translational motion in porous media. In R. Tycko, editor, *Nuclear magnetic resonance probes of molecular dynamics*, chapter 11, pages 489–523. Kluwer Academic Publishers, New York, (1994).

[43] L. L. Latour, P. P. Mitra, R. L. Kleinberg, and C. H. Sotak. *J. Magn. Reson. A*, **101**, 342 (1993).

[44] O. Söderman. private communication, (1992).

[45] O. Söderman and B. Jönsson. *J. Magn. Reson.* (1995). submitted.

[46] P. T. Callaghan. *J. Magn. Reson. A* (1994). submitted.

[47] B. Balinov, B. Jönsson, P. Linse, and O. Söderman. *J. Magn. Reson. A*, **104**, 17 (1993).

[48] C. H. Neuman. *J. Chem. Phys.*, **60**, 4508 (1974).

[49] J. S. Murday and R. M. Cotts. *J. Chem. Phys.*, **48**, 4938 (1968).

[50] M. H. Blees. *J. Magn. Reson. A*, **109**, 203 (1994).

[51] G. P. Zientara and J. H. Freed. *J. Chem. Phys.*, **72**, 1285 (1980).

[52] P. P. Mitra and B. I. Halperin. *J. Magn. Reson. A* (1994). in press.

[53] E. M. Terentjev, P. T. Callaghan, and M. Warner. *J. Chem. Phys.* (1994). submitted.

[54] P. T. Callaghan. *J. Magn. Reson.*, **88**, 493 (1990).

[55] J. E. M. Snaar and H. Van As. *J. Magn. Reson. A*, **102**, 318 (1993).

[56] K. R. Brownstein and C. E. Tarr. *Phys. Rev. A*, **19**, 2446 (1979).

[57] K. R. Brownstein and C. E. Tarr. *J. Magn. Reson.*, **26**, 17 (1977).

[58] S. Frey, J. Karger, H. Pfeifer, and P. Walther. *J. Magn. Reson.*, **79**, 336 (1988).

[59] W. H. Press, B. P. Flannery, S. A. Teukolsky, and W. T. Vetterling. *Numerical Recipies in C*. Cambridge University Press, Cambridge, (1988).

[60] B. Pütz, D. Barsky, and K. Schulten. *J. Magn. Reson.*, **97**, 27 (1992).

[61] W. B. Hyslop and P. C. Lauterbur. *J. Magn. Reson.*, **94**, 501 (1991).

[62] P. T. Callaghan, A. Coy, L. C. Forde, and C. J. Rofe. *J. Magn. Reson. A*, **101**, 347 (1993).

[63] L. C. Forde. Susceptibility, diffusion and relaxation contrast in NMR microscopy at high resolution. Master's thesis, Massey University, (1994).

[64] B. P. Hills and J. E. M. Snaar. *Mol. Phys.*, **76**, 979 (1992).

[65] J. E. Tanner. *J. Chem. Phys.*, **69**, 1748 (1978).

[66] P. T. Callaghan, D. MacGowan, K. J. Packer, and F. O. Zelaya. *J. Magn. Reson.*, **90**, 177 (1990).

[67] P. T. Callaghan, A. Coy, T. P. J. Halpin, D. MacGowan, K. J. Packer, and F. O. Zelaya. *J. Chem. Phys.*, **97**, 651 (1992).

[68] P. T. Callaghan, D. MacGowan, K. J. Packer, and F. O. Zelaya. *Magn. Reson. Imag.*, **9**, 663 (1991).

[69] L. C. Graton and H. J. Fraser. *J. Geol.*, **XLIII**, 785 (1935).

[70] A. Coy and P. T. Callaghan. *J. Coll. Interf. Sci.*, **168**, 373 (1994).

[71] P. T. Callaghan, A. Coy, E. Dormann, R. Ruf, and N. Kaplan. *J. Magn. Reson. A*, **111**, 127 (1994).

[72] N. Kaplan, E. Dormann, R. Ruf, A. Coy, and P. T. Callaghan. *Phys. Rev. B* (1995). submitted.

[73] R. Ruf, N. Kaplan, and E. Dormann. *Phys. Rev. Lett.* (1995). in press.

[74] M. Conradi, A. N. Garroway, D. G. Cory, and J. Miller. *J. Magn. Reson.*, **94**, 370 (1991).

[75] B. Balinov, O. Söderman, and J. C. Ravey. *J. Phys. Chem.*, **98**, 393 (1994).

[76] P. G. de Gennes. *J. Chem. Phys.*, **55**, 572 (1971).

[77] M. Doi and S. F. Edwards. *The Theory of Polymer Dynamics*. Oxford University Press, Oxford, (1986).

[78] P. F. Green and E. J. Kramer. *Macromolecules*, **19**, 1108 (1986).

[79] L. Léger, H. Hervet, and F. Rondelez. *Macromolecules*, **14**, 1732 (1981).

[80] D. Richter, B. Ewen, B. Farago, and T. Wagner. *Phys. Rev. Lett.*, **62**, 2140 (1989).

[81] G. Reiter and U. Steiner. *J. Phys. II*, **1**, 659 (1991).

[82] D. Richter, B. Farago, L. J. Fetters, J. S. Huang, B. Ewen, and C. Lartigue. *Phys. Rev. Lett.*, **64**, 1389 (1990).

[83] K. Kremer and K. Binder. *J. Chem. Phys.*, **81**, 6381 (1984).

[84] J. M. Deutsch. *Phys. Rev. Lett.*, **49**, 926 (1982).

[85] A. Baumgärtner. *Annual Review of Physical Chemistry*, **35**, 419 (1984).

[86] K. Kremer, G. S. Grest, and I. Carmesin. *Phys. Rev. Lett.*, **61**, 566 (1988).

[87] N. P. T. O'Connor and R. C. Ball. *Macromolecules*, **25**, 5677 (1992).

[88] K. Kremer and G. S. Grest. *J. Phys. Condens. Matter (U.K.)*, **2 suppl A**, 295 (1990).

[89] T. P. Lodge, N. A. Rotstein, and S. Prager. *Adv. Chem. Phys.*, **74**, 1 (1990).

[90] J. Skolnick, A. Kolinski, and R. Yaris. *Acc. Chem. Res.*, **20**, 350 (1987).

[91] P. T. Callaghan and D. N. Pinder. *Macromolecules*, **18**, 373 (1985).

[92] M. Doi and S. F. Edwards. *J. Chem. Soc. Faraday Trans. 2*, **74**, 1789 (1978).

[93] R. E. Rouse. *J. Chem. Phys.*, **21**, 1272 (1953).

[94] P. T. Callaghan and A. Coy. *Phys. Rev. Lett.*, **68**, 3176 (1992).

[95] J. Skolnick, R. Yaris, and A. Kolinski. *J. Chem. Phys.*, **88**, 1407 (1988).

[96] J. Skolnick and R. Yaris. *J. Chem. Phys.*, **88**, 1418 (1988).

[97] A. T. Yates, J. Skolnick, and R. Yaris. *J. Poly. Sci. B*, **27**, 151 (1989).

[98] K. S. Schweizer. *J. Chem. Phys.*, **91**, 5802 (1989).

[99] J. des Cloizeaux and G. Jannink. *Polymers in Solution. Their Modelling and Structure.* Oxford University Press, Oxford, (1987).

[100] P. T. Callaghan and D. N. Pinder. *Macromolecules*, **14**, 1334 (1981).

[101] W. Paul, K. Binder, D. W. Heerman, and K. Kremer. *J. Phys. (France) II*, **1**, 37 (1991).

[102] E. D. von Meerwall. *Adv. Poly. Sci.*, **54**, 1 (1983).

[103] V. D. Skirda, V. I. Sundukov, A. I. Maklakov, O. E. Zgadzai, I. R. Gafurov, and G. I. Vasiljev. *Polymer*, **29**, 1294 (1988).

Appendix A

Publications

P. J. Back, A. Coy, Y. Xia, P. T. Callaghan, L. M. Diamante, and S. L. Umbach, "Some biophysical applications of motional contrast in n.m.r microscopy." *International Journal of Biological Macromolecules*, **13**, 181–189 (1991).

P. T. Callaghan, A. Coy, D. MacGowan, K. J. Packer, and F. O. Zelaya, "Diffraction-like effects in NMR diffusion studies of fluids in porous solids." *Nature (London)*, **351**, 467–469 (1991).

P. T. Callaghan, A. Coy, T. P. J. Halpin, D. MacGowan, K. J. Packer, and F. O. Zelaya, "Diffusion in porous systems and the influence of pore morphology in pulsed gradient spin echo nuclear magnetic resonance studies." *Journal of Chemical Physics*, **97**, 651–662 (1992).

P. T. Callaghan, A. Coy, D. MacGowan, and K. J. Packer, "Diffusion of Fluids in Porous Solids Probed by Pulsed Field Gradient Spin Echo NMR." *Journal of Molecular Liquids*, **54**, 239–251 (1992).

P. T. Callaghan, and A. Coy, "Evidence for Reptational Motion and the Entanglement Tube in Semidilute Polymer Solutions." *Physical Review Letters*, **68**, 3176–3179 (1992).

P. T. Callaghan, A. Coy, L. C. Forde, and C. J. Rofe, "Diffusive Relaxation and Edge Enhancement in NMR Microscopy." *Journal of Magnetic Resonance A*, **101**, 347–350 (1993).

R. Kimmich, S. Stapf, P. T. Callaghan, and A. Coy, "Microstructure of porous media probed by NMR techniques in sub μm length scales." *Magnetic Resonance Imaging*, **12**, 339–344 (1994).

P. T. Callaghan and A. Coy. "PGSE NMR and molecular translational motion in porous media." In R. Tycko, editor, *Nuclear magnetic resonance probes of molecular dynamics*, chapter 11, pages 489–523. Kluwer Academic Publishers, New York, (1994).

A. Coy, and P. T. Callaghan, "Pulsed Gradient Spin Echo NMR 'Diffusive Diffraction' Experiments on Water Surrounding Close-Packed Polymer Spheres." *Journal of Colloid and Interface Science*, **168**, 373–379 (1994).

A. Coy, and P. T. Callaghan, "Pulsed Gradient Spin Echo NMR for molecules diffusing between partially reflecting rectangular barriers." *Journal of Chemical Physics*, **101**, 4599–4609 (1994).

P. T. Callaghan, A. Coy, E. Dormann, R. Ruf and N. Kaplan, "Pulsed-Gradient Spin-Echo ESR." *Journal of Magnetic Resonance A*, **111**, 127–131 (1994).

N. Kaplan, E. Dormann, R. Ruf, A. Coy, and P. T. Callaghan, "Restricted electron motion in a one dimensional organic conductor: Pulsed gradient spin echo ESR in $(FA)_2PF_6$." *Journal of Chemical Physics*, submitted.

Appendix B

Software

A description of the programs written by the author and used in these studies is given here. The source code for all programs can be obtained by contacting the author by e-mail at "A.Coy@massey.ac.nz". The majority of the software written was compiled and executed on Apple Macintosh computers but the descriptions indicate if a different machine was used.

B.1 PGSEPLOT

A program written to display and analyse PGSE data. This program runs on a Macintosh computer and has been the backbone of data analysis for this thesis. It can fit a range of theoretical echo attenuation functions to PGSE data using a non-linear least squares fitting algorithm. The resultant fit parameters are displayed and a graph is shown on-screen which can be printed for a permanent record. An example of the program running is shown in Figure B.1.

The program has around 6000 lines of code in 11 modules which generates about 70K of compiled code. The first version of the program was written in July 1990 and has since been updated many times. The current version number is 3.4 and I still have further modifications I wish to make.

B.2 PGSE-JEOL

A program used to receive FID data from the GX-270 spectrometer. The program used the RS-232c serial communications port to receive the data, and then analyses the data to produce a final PGSE file suitable for use with the PGSEPLOT program. Two versions were written. One to do standard PGSE analysis, the second for PGSE-MASSEY experiments where the individual FID's are co-added after Fourier transformation and taking the modulus.

The programs have around 2000 lines of code which generate about 25K of compiled code.

B.3 PGSE-FX60

A program written to automate PGSE data acquisition from the FX-60 spectrometer. Originally this job was performed by a program running on the Hitachi PC, but
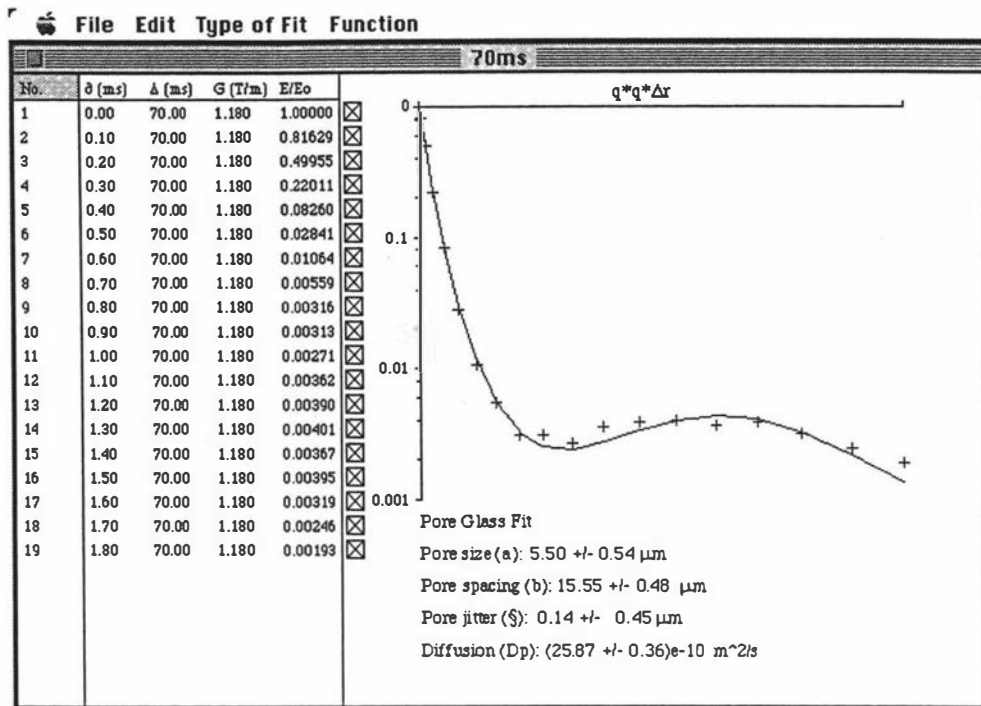
Figure B.1: Sample output from the PGSEPLOT program. The PGSE data is displayed on the left. The data is plotted as crosses on a Stejskal-Tanner plot on the right. The line represents a fit to the pore glass hopping model with a Gaussian distribution of pore spacings. The paramters a, b, D_{eff} and ξ, obtained from the fit, are shown below the graph (note the program has no suitable symbol for ξ yet).

a replacement was required as the Hitachi keyboards failed. This Macintosh program had the advantage of being able to save the acquired data in a file suitable for analysis by the PGSEPLOT program. A small program was also written, and left running on the Hitachi, to provide a simple parallel to serial interface to the Macintosh. An example of the PGSE-FX60 program running is shown in Figure B.2. This system has since been replaced in our lab by the Tecmag LEO/J computer interface.

The program has around 3000 lines of code which generates about 35K of compiled code.

B.4   Simulations

A range of simulation programs were written. The programming language C was used as this enabled programs developed on the Macintosh to be run on the faster Unix machine available in our lab. The simulations were written to emulate a PGSE experiment and saved files containing the density function and average propagator as well as the echo attenuation function. The main simulations run were to test the relaxing wall parallel plane barrier model, but additional simulations tested the effects of finite gradient pulses as well.

These programs were generally small, about 1000 lines of code, generating around 20K of compiled code.
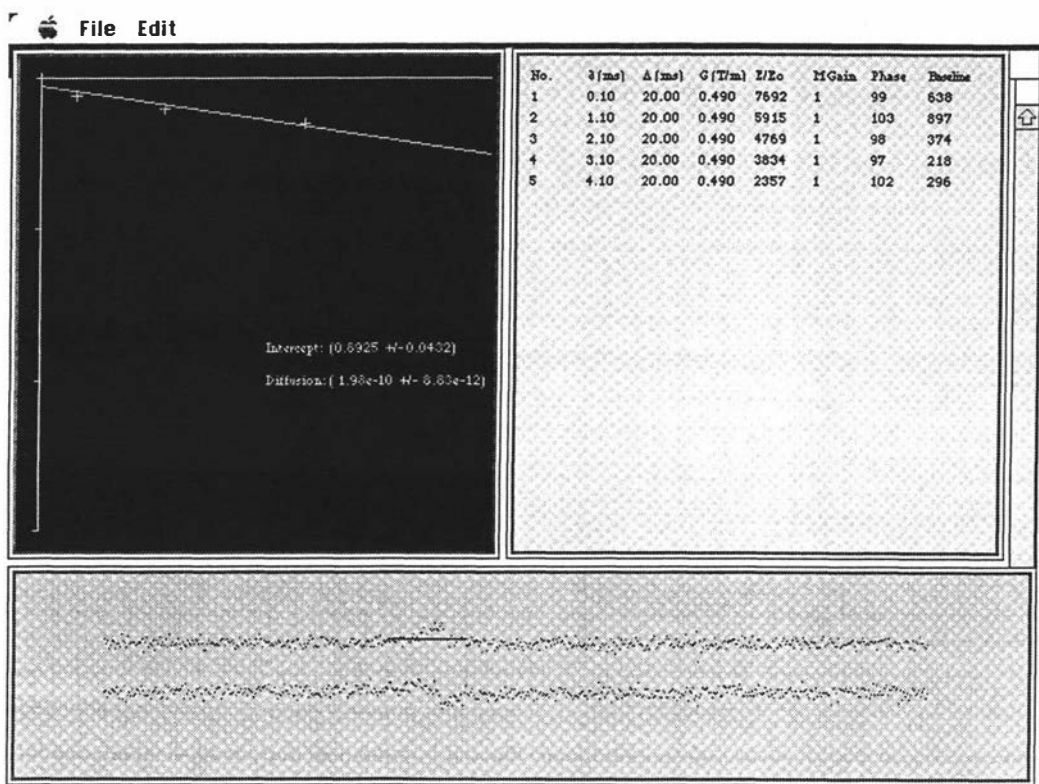
No.	δ (ms)	Δ (ms)	G (T/m)	I/Io	HGain	Phase	Baseline
1	0.10	20.00	0.490	7692	1	99	638
2	1.10	20.00	0.490	5915	1	103	897
3	2.10	20.00	0.490	4769	1	98	374
4	3.10	20.00	0.490	3834	1	97	218
5	4.10	20.00	0.490	2357	1	102	296

Intercept: (0.6925 +/- 0.0432)

Diffusion: (1.98e-10 +/- 6.63e-12)

Figure B.2: Sample output from the PGSE-FX60 program. The bottom window shows the most recently acquired spectrum, which is autophased. The peak area is integrated and the result is added to the file in the upper right window. As each q-space point is acquired, the data set is plotted on a graph in the upper left window allowing the operator to check that the experiment is running correctly. A linear least squares fit shows the slope of the graph, and in cases where the self-diffusion coefficient is known, the slope can be used to check that the experimental parameters are correctly set. The data is then saved in a format suitable for use with the PGSEPLOT data analysis program.

B.5 Theory

An early program I wrote to generate theoretical curves for the Stejskal-Tanner parallel plane barrier equation was rewritten several times to emulate many other equations. The program allowed the user to enter parameters to the equation and see the curves before saving the echo attenuation data into files as required. Versions of this program for parallel barrier restricted diffusion, eqns (4.20) and (4.21); parallel barrier restricted diffusion with relaxation at the boundaries, which involved finding roots of transendental equations, eqns (6.27), (6.26) and (6.20); pore hopping theory, eqns (7.26), (7.31) and (7.33); the modified pore hopping theory for the electron diffusion experiments, eqns (7.40), and (7.41); polymer diffusion mean squared displacement, eqns (8.16), and (8.28); polymer structure functions, eqns (8.24); were written.

An example of this program, called RECTSIM, to generate $E(q)$ curves for the parallel plane barrier equation, eqn (4.21), is shown in Figure B.3. This was often refered to as the rectangular box equation, hence the program name.

The RECTSIM version of the program has under 1000 lines of code which generates about 15K of compiled code. By contrast the MRECT version of the program, which includes relaxation effects and therefore needs to find the roots of the transendental equations has around 1500 lines of code generating 25K of code.

B.6 BrukerTranslate

A program written to convert AMX300 files into Macintosh files suitable for use with the Imageshow program. This program has around 2000 lines of code producing about 25K of code.
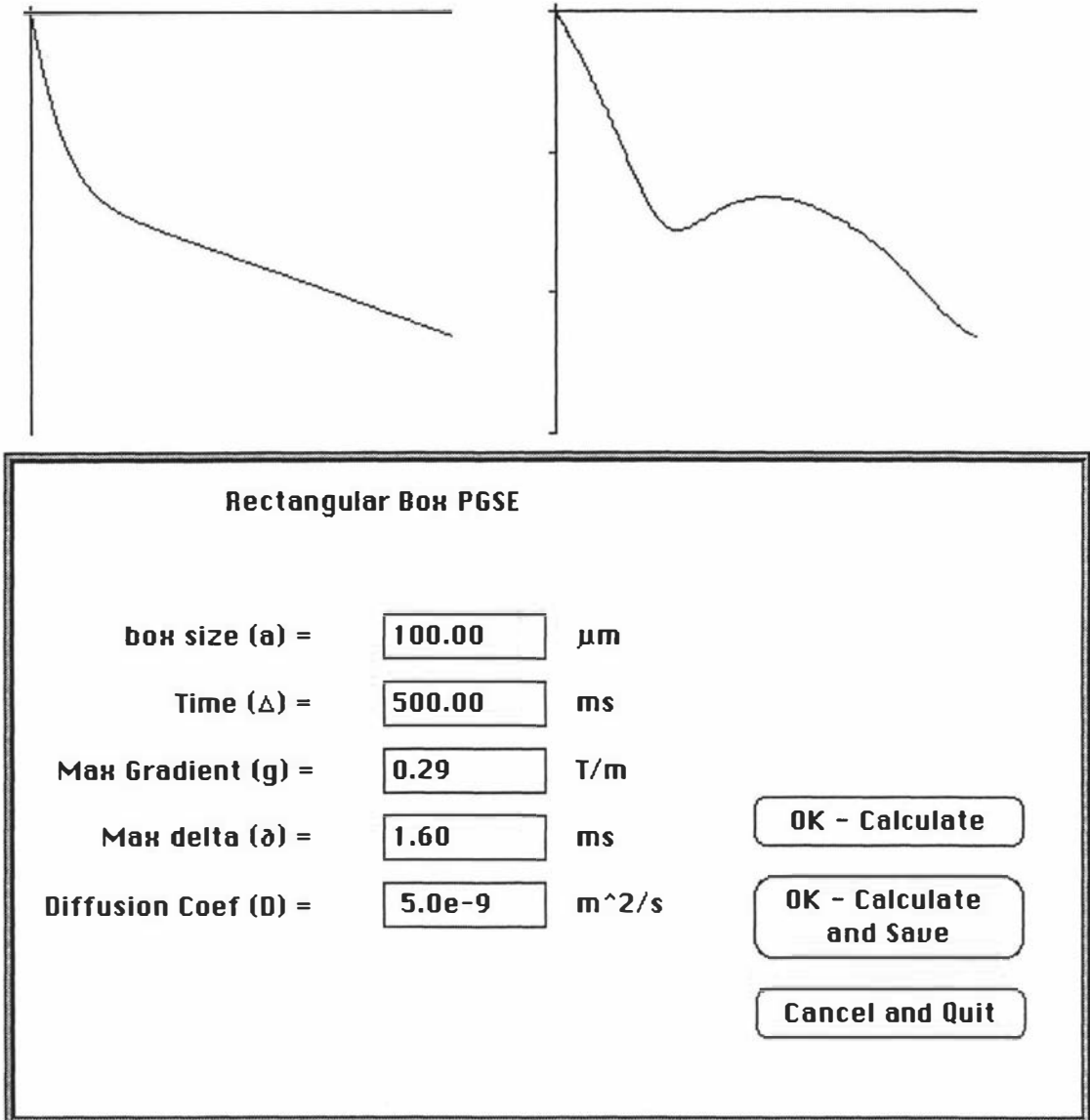
Rectangular Box PGSE

box size (a) =	100.00	µm
Time (Δ) =	500.00	ms
Max Gradient (g) =	0.29	T/m
Max delta (∂) =	1.60	ms
Diffusion Coef (D) =	5.0e-9	m^2/s

OK – Calculate

OK – Calculate and Save

Cancel and Quit

Figure B.3: Sample output from the RECTSIM program. This program formed the basis for many other programs which numerically eveluted different equations to generate echo attenuation curves. Parameters are entered in the dialog box and the echo attenuation curves displayed on the graphs above. The left graph shows the effect of varying Δ and holding the gradient at the value chosen in the dialog box. The right graph shows a q-space plot where Δ is fixed at the value given and the gradient is varied. The numerical curves could then be saved for use in analyising experimental data.